Journal of Materials Chemistry A

ROYAL SOCIETY OF CHEMISTRY

REVIEW

View Article Online
View Journal | View Issue

Cite this: *J. Mater. Chem. A*, 2022, **10**, 2196

Recent advances, practical challenges, and perspectives of intermediate temperature solid oxide fuel cell cathodes

Amanda Ndubuisi, Sara Abouali, Kalpana Singh and Venkataraman Thangadurai *

As a highly efficient clean power generation technology, intermediate temperature (600–800 °C) solid oxide fuel cells (IT-SOFCs) have gained much interest due to their rapid start-up and shut-down capability, longer life-time and lower cost compared to the conventional SOFCs. However, the sluggish oxygen reduction reaction (ORR) at the cathode at lower temperatures, chromium (Cr) poisoning of cathodes when exposed to Cr-based interconnects, material degradation under CO_2 and humid atmospheres, and compatibility of Co-containing cathodes with existing IT-SOFC electrolytes still affect their large-scale development. This work aims to present an overview on the latest achievements in developing IT-SOFC cathodes based on perovskite-type and other crystal structures, and composites. The utilisation of distribution of relaxation times for analysing the impedance spectra of SOFC cathodes has been discussed. Furthermore, this article presents summary towards the rational design of the cathode materials and structures, to realize cost-effective and high-performance IT-SOFCs.

Received 30th September 2021
Accepted 19th December 2021

DOI: 10.1039/d1ta08475e

rsc.li/materials-a

Introduction

Solid oxide fuel cells are electrochemical energy conversion devices attractive for clean generation of electricity from a variety of fuels with high efficiency. The chemical energy of reactants in SOFCs is directly converted into electrical energy through the oxidation of the fuel without any intermediate step of combustion. Thus, unlike combustion engines, this technology is not limited by the Carnot cycle efficiency. Due to their high efficiency and energy densities, SOFCs have the potential for large-scale stationary power generation. Current SOFCs are operating at high temperatures (800–1000 °C) which eliminates the need for expensive noble metal catalysts by increasing the electrochemical kinetics of reactions. Waste heat generated from high temperature SOFCs (HT-SOFCs) can be fed into combined heat and power (CHP) systems to increase the total efficiency of the system. Integrating SOFC units in central heating systems of households will not only provide electricity but heat and hot water with natural gas as fuel. Furthermore,

Department of Chemistry, University of Calgary, Calgary, Alberta, T2N 1N4, Canada. E-mail: vthangad@ucalgary.ca

Amanda Ndubuisi received her M.Sc. degree in Physics from Covenant University, Nigeria, specializing in Renewable Energy and Materials Science. She is a PhD student at the Department of Chemistry, University of Calgary, Canada, supervised by Professor Venkataraman Thangadurai. Her research focuses on developing mixed ionic and electronic catalysts for oxygen reduction in intermediate temperature solid oxide fuel cells and CO_2 reduction in solid oxide electrolysis cells.

Dr Sara Abouali is a materials scientist in the field of electrochemical energy storage/conversion devices. She obtained her PhD in Mechanical Engineering (Energy Concentration) from the Hong Kong University of Science and Technology (HKUST) in 2016. Since then, she has been working as a researcher/postdoctoral associate in international institutes in Hong Kong, Italy and Canada. She has published several scientific papers and patents on designing advanced electrodes and electrolytes for batteries, supercapacitors and fuel cells.

employing the SOFC technology will lower carbon footprint as it generates high quality CO_2 which can be sequestered and used as fuel in reverse mode SOFCs (electrolyser cells) to yield syngas, suitable for zero carbon economy.

Despite the advantages of HT-SOFCs, operating at high temperature presents significant drawbacks which hinder their full implementation in energy systems. These challenges include high cost of interconnects and sealants, accelerated degradation of the components, and subsequent degeneration in the performance of the cell as a result of elevated working temperatures. The state-of-the-art materials for SOFCs consist of Ni-yttria-stabilized zirconia (YSZ) composite anodes, oxide ion conducting YSZ electrolyte, and $La_{1-x}Sr_xMnO_{3-\delta}$ (LSM) cathode. Ni–YSZ composite anode is susceptible to redox cycling instability, and H_2S and coke poisoning.[1,2] LSM is typically mixed with YSZ electrolyte in a composite to extend the triple phase boundary which is an active site for oxygen reduction and increases the ionic conductivity.

Lowering the operating temperature of SOFCs to the intermediate temperature (IT) range (600–800 °C) has been reported to mitigate the challenges associated with HT-SOFCs thus offering technical and economic advantages.[3,4] On the other hand, decreasing the operating temperature to intermediate levels, will generate some other challenges towards the oxygen reduction reaction (ORR) activity of the cathode. The reduction of oxygen at the cathode is a thermally activated process and the kinetics of the reaction is decelerated, leading to significant electrical losses and a drop in the electrochemical performance of the cell at lower temperatures. Therefore, designing an advanced cathode with a high catalytic activity is essential to enhance the electrochemical performance of the cell at intermediate temperatures. Several cathode designs with novel compositions and engineered micro/nanostructures have been proposed. Also, advanced techniques have been used to further shed light on the electrochemical properties of the cathode and anode. One of these relatively new approaches is using the distribution of relaxation times (DRT) to analyse the impedance spectra to measure the polarization resistance of the anode and cathode.[5] Herein, we present an overview on advances in the development of IT-SOFC cathodes, mainly focusing on the development of novel cathode compositions and structures based on single perovskites, double perovskites, Ruddlesden–Popper layered perovskite-type oxides, swedenborgite-type, garnet-type and composite cathodes. The challenges associated with each group have been discussed and some of the proposed solutions have been reviewed. Afterwards, a brief discussion on the ORR mechanism has been presented and the application of DRT for analysing the degradation mechanisms of IT-SOFC cathodes is discussed.

Perovskite-type structure SOFC cathodes

As an important family of oxides, perovskite-type structures have shown great potential to be used as electrocatalysts for the ORR in an SOFC cathode. A variety of perovskite compositions have been developed with unique characteristics while specific concerns have been identified for each group. Overview on the structure, synthesis, compositions and electrocatalytic behaviour of perovskites along with the latest progress and strategies

Dr Singh received her PhD in 2016 from the University of Calgary (UofC), Canada, with specialisation in Physical Chemistry. She was a graduate student in the laboratory of Venkataraman Thangadurai at Calgary. Dr Singh's research interests include fundamentals of solid state electrolytes and electrodes for solid oxide fuel cells. During her PhD research at Calgary, she extended her research direction towards mixed conducting metal oxides for solid oxide electrolyser cells. Dr Singh has authored 18 peer-reviewed publications, 3 conference proceedings, and 1 patent application as a result of goal driven PhD and post-doctoral research, independent research projects, and collaborations with research institutes in USA, China, Australia, and Israel.

Dr Venkataraman Thangadurai is a full professor of chemistry, University of Calgary. He received his PhD in 1999 from Indian Institute of Science, Bangalore, India. He conducted his postdoctoral research at the University of Kiel, Germany, with a prestigious fellowship from the Alexander von Humboldt Foundation, Bonn. In 2004, he received the Habilitation degree from the University of Kiel. He is a Fellow of the Royal Society of Chemistry, United Kingdom, Fellow of the International Association of Advanced Materials, Sweden, and Fellow of The Electrochemical Society. He received the prestigious Keith Laidler Award and Research Excellence in Materials Chemistry Award from the Canadian Society of Chemistry. His research focuses on the design, synthesis and characterization of novel solid-state electrolytes and elemental and mixed conducting electrodes for next generation solid-state batteries, solid oxide fuel cells, electrolysis cells, catalysis, and gas sensors. He has 220+ publications (h-index 58), which have been cited over 15 500 times.

on mitigating the practical challenges of this class of complex oxides when used as IT-SOFC cathodes is presented.

Crystal structure

The first perovskite oxide was discovered by Gustav Rose in 1839 with a chemical composition of $CaTiO_3$ and was named after Lev Aleksevich von Perovski, a Russian mineralogist.[6,7] The general formula of a perovskite can be written as ABO_3, where A and B are cations with a coordination number of 12 and 6, respectively.[8] Alkaline, alkaline-earth and rare-earth metals can occupy larger A-sites while transition metals with smaller size can occupy B-sites.[8,9] Fig. 1a schematically shows an ideal cubic perovskite structure, however, due to the variation of ionic radius after cation substitutions, structural distortion changes the cubic lattice to tetragonal, orthorhombic, and rhombohedral, as demonstrated in Fig. 1b–d.[10–17] The deviation of the lattice from an ideal cubic structure can be calculated using the tolerance factor (t) as:

$$t = \frac{r_A + r_O}{\sqrt{2}(r_B + r_O)} \quad (1)$$

where r_A and r_B are the ionic radii of A and B cations, respectively, and r_O is the ionic radii of oxygen. The perfect cubic symmetry is obtained when $t = 1$, while $t < 1$ and $t > 1$ lead to the formation of less symmetric crystals with rhombohedral/orthorhombic (Fig. 1b and c) and hexagonal structures (Fig. 1d), respectively. It should be noted that the physicochemical properties of perovskites are highly governed by their structure which in turn can be tuned by partial or complete substitution of A and/or B cations.[9]

Synthesis methods of perovskite structures

Table 1 summarizes the most common techniques to synthesize perovskite-type SOFC cathodes and compares their advantages and disadvantages.[14–17] The solid-state synthesis method is a simple and mature technique, however, less homogeneity of the composition, grain growth due to sintering at high temperatures and lower surface area limiting their catalytic behaviour are some of the disadvantages of this method.[14–17] In contrast, the sol–gel technique benefits from a good homogeneity of the chemical composition, better control over grain size and processing at lower temperatures.[15–17] Another common technique is the co-precipitation method which produces

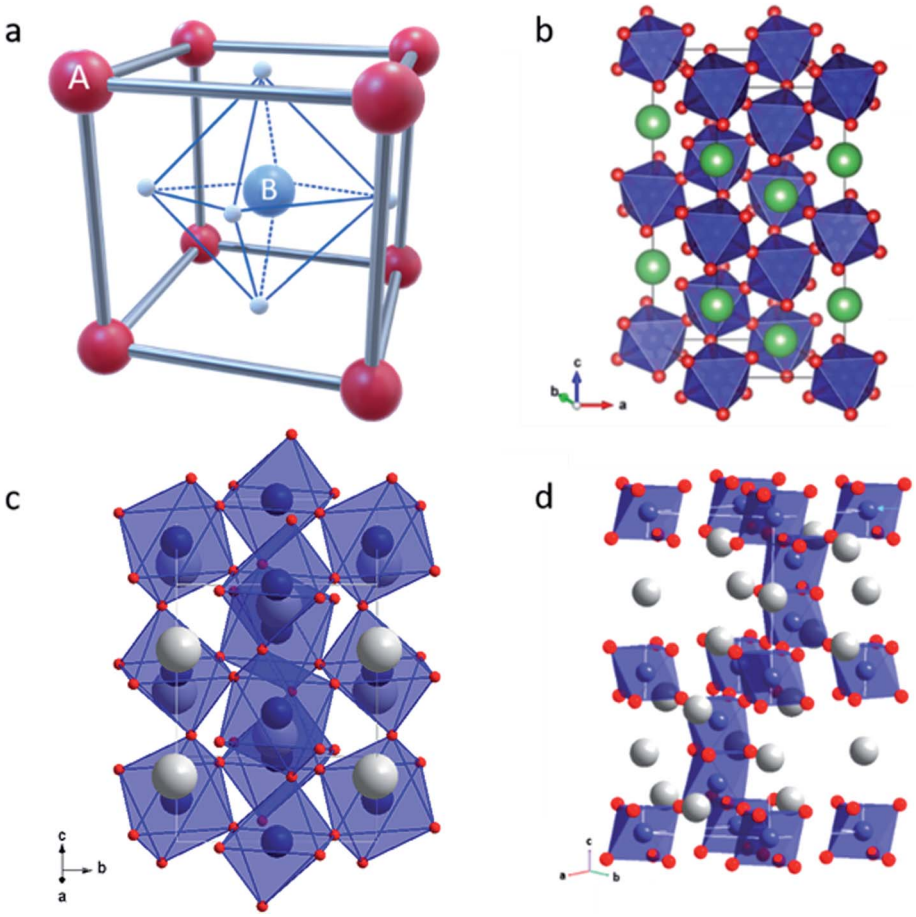

Fig. 1 Schematic illustration of a perovskite-type (ABO_3) crystal with (a) cubic, (b) rhombohedral. Reprinted with permission from ref. 11. Copyright 2017 American Chemical Society. (c) Orthorhombic[12] and (d) hexagonal structures. Reprinted from ref. 13. Copyright 2015, with permission from Elsevier.

Table 1 Comparison of common synthesizing techniques for perovskite-type structure cathodes[14–17]

Technique	Advantages	Disadvantages
Solid-state method	Simple and scalable, mature technology	High sintering temperatures and long processing times, inhomogeneity of the composition, grain growth, lower surface area
Sol–gel	Lower annealing temperatures and uniform morphologies	Works in a liquid phase, less-scalability, needs a soluble salt (precursor)
Co-precipitation	Uniform chemical composition with less impurity	Slow rate of precipitation
Solution combustion	Low-temperature process, good control over composition and particle size, allows for higher dopant concentration, fast rate of production	Low surface area

single-phase perovskite oxides, but the synthesis time is longer due to a slow precipitation rate.[17] Combustion method is a cost-effective, low-temperature technique to make perovskites with controlled particle size and morphology and enables a higher concentration of dopants.[17–19] The selection of the synthesis route should be based on the cost/scalability, compositional homogeneity and particle-size/morphology requirements which affect the catalytic behaviour of the final product.

Perovskites for IT-SOFC cathodes: composition–structure–property relationship

Efforts to design a high-performance IT-SOFC cathode have led to the development of a variety of perovskites with different chemical compositions and structures.[17] Mixed ionic-electronic conductors (MIECs) have gained an increasing interest due to their improved ORR kinetics at IT range benefitting from both ionic and electronic conduction.[18] Elemental doping has been a strong tool for tuning different properties of a perovskite material such as ORR activity, electronic/ionic conductivity, thermal expansion coefficient (TEC), and structural stability. Moreover, surface functionalization, designing novel electrode structures such as core–shell structures[19] and electrospun fibers,[20] nanostructuring of the electrode,[16,21–24] and composite cathodes[25] are other important techniques that have been used to enhance the electrochemical performance and stability of the electrode under operational conditions.

The A-site in a perovskite structure is occupied by larger size cations compared to B-site cations. Lanthanide elements such as La, Pr, Nd, Sm and Gd are common occupants of the A-site, while common B-site cations include transition metals such as Mn, Co, Fe, Cu and Ni.[17] Single doping or co-doping at A and/or B-sites creates a series of perovskites with different properties. Valence and ionic radii of the dopants are two critical parameters to determine the conduction behaviour of the material. With a similar valence of the dopant and lattice element, the change of electronic conductivity is attributed to the change of structural parameters due to the size effect.[9] In the case of aliovalent doping in the A-site, the electrical neutrality of the system can be compensated by changing the oxidation state of multivalent cations at B-sites or by formation of lattice oxygen vacancies.[9] A general formula of $A_{1-x}A'_xB_{1-y}B'_yO_{3-\delta}$ can be used to describe the chemical composition of the doped perovskite in which δ (0–1) indicates the lattice oxygen vacancies or oxygen non-stoichiometry.[18]

One of the most investigated high-temperature SOFC cathodes is lanthanum strontium manganite ($La_{1-x}Sr_xMnO_{3-\delta}$, LSM) where Sr^{2+} is doped at the La^{3+} site to introduce oxide ion vacancies due to the charge compensation mechanism in the parent structure of lanthanum manganite ($LaMnO_3$).[26,27] Sr and other alkaline-earth elements such as Ca^{2+} and Ba^{2+} have been commonly used for La substitution to enhance electrical conductivity.[9] However, these elements can chemically react with CO_2 and the electrolyte with increasing reactivity from Ca to Ba.[9] Several studies have investigated the effects of Sr concentration on different properties of LSM perovskites.[26–28] The $x \cong 0.5$ composition has shown a high conductivity and high catalytic activity towards the ORR, high thermal and microstructural stability, and good compatibility of TEC with common SOFC electrolytes such as YSZ (TEC_{YSZ}: 10.5×10^{-6} K^{-1} in air at 800 °C).[26,27,29] However, this composition is not an optimum cathode candidate in IT-SOFCs due to the inferior performance at lower operational temperature.[8,26]

It is known that replacing Mn with Fe ($La_{1-x}Sr_xFeO_{3-\delta}$, LSF) or Co ($La_{1-x}Sr_xCoO_{3-\delta}$, LSC) generates oxygen vacancies that promotes the ORR kinetics at lower temperatures.[27] LSC shows high electronic conductivity with a metallic behaviour attributed to the partially filled conduction band with delocalized conduction electrons.[30] LSF shows lower electronic conduction compared to LSC, with the hopping mechanism of localized electrons/holes responsible for the electronic conduction.[30] While LSC compounds show much improved ionic conduction (0.22 S cm^{-1})[15] compared to LSM, high contents of Co increase the TEC leading to a mismatch with conventional electrolytes.[27] Moreover, the high cost of Co is another limiting factor, motivating the partial or full substitution of Co with other elements.[31] One of the most investigated MIECs is the $La_{1-x}Sr_xCo_{1-y}Fe_yO_{3-\delta}$ (LSCF) family[30] possessing high electronic and ionic conductivity of $\sim 10^2$ and $\sim 10^{-2}$ S cm^{-2} at 800 °C, respectively, and a TEC value of 14.8–21.4 $\times 10^{-6}$ K^{-1} at 500–900 °C.[15,30,32–34] Different properties of the LSCF can be tuned by changing its chemical composition.

In general, the electronic conductivity of the LSCF is more controlled by the concentration of Fe and Co, while Sr content has a higher impact on controlling the ionic conductivity.[27] Also, it is reported that a high concentration of Sr and Co will increase the TEC value.[27] Investigations on the stability behaviour of the LSCF perovskites under the operational conditions have revealed some concerns including the chemical instability and TEC mismatch with YSZ electrolyte, surface segregation of Sr and Co, and reactivity of the cathode with contaminants including gas contaminants, *i.e.*, water vapor, CO_2 and SO_2 or volatile species coming from other cell components such as sealants or interconnects, *i.e.*, Cr, B and Si.[17,30]

The reactivity of LSCF towards YSZ leads to the formation of secondary phases such as $SrZrO_3$ at temperatures ≥800 °C.[30] To overcome the reactivity issue and to decrease the TEC mismatch, interlayers such as Gd-doped ceria (GDC) or Sm-

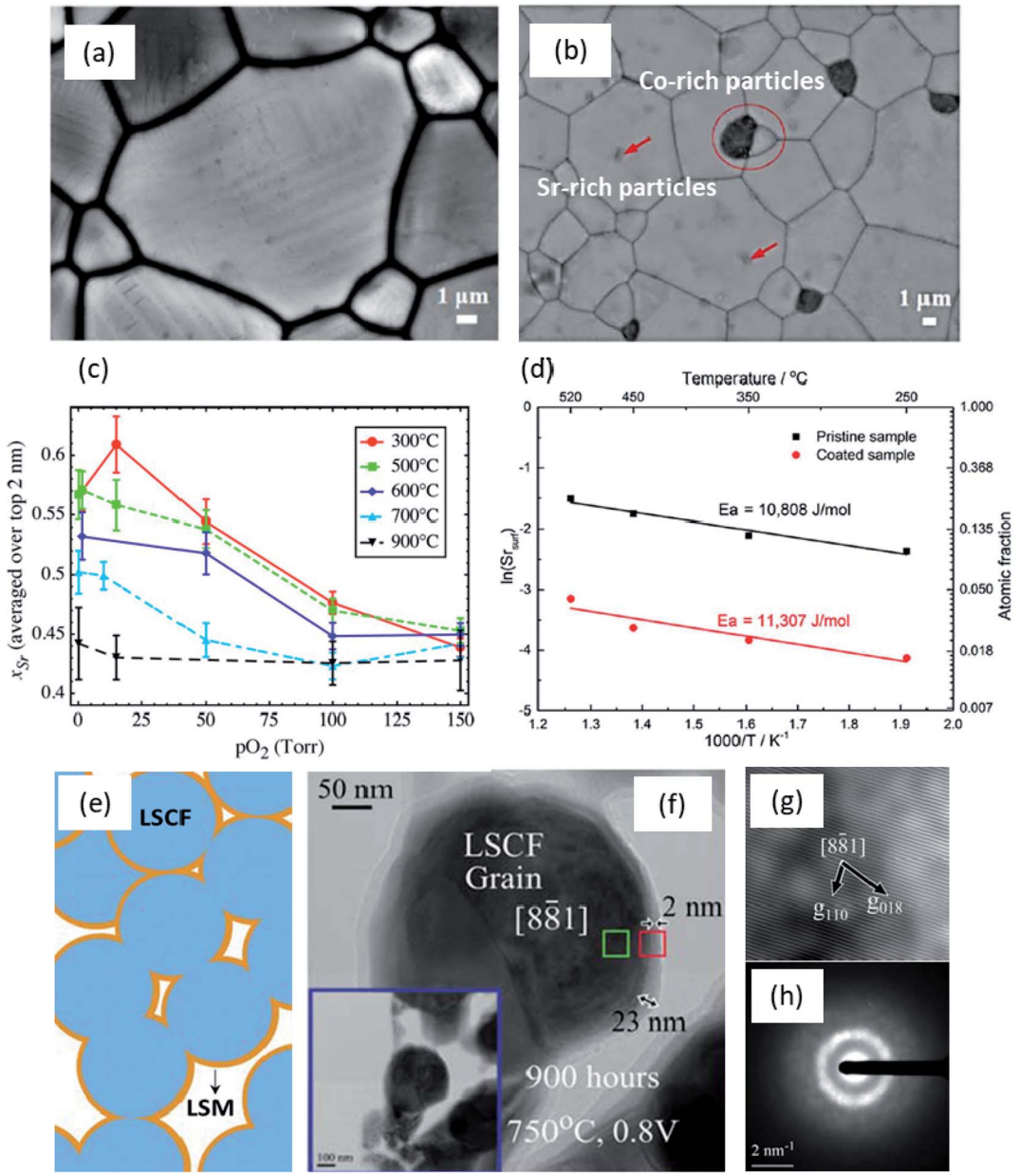

Fig. 2 (a) SEM image of a freshly prepared LSCF showing a dense, pinhole-free structure; (b) SEM image of LSCF heat treated at 800 °C, 96 h in the absence of Cr_2O_3 in air. Segregation of Co/Sr-rich particles can be observed. Reproduced from ref. 47 with permission from the Royal Society of Chemistry; (c) Sr surface region concentration *vs.* oxygen partial pressure. Reprinted from ref. 41, with the permission of AIP Publishing; (d) Arrhenius plots of atomic fractions of surface Sr in pristine and coated samples. Reproduced from ref. 40 with permission from the Royal Society of Chemistry; (e) schematic illustration of LSM-infiltrated LSCF cathode; (f) TEM image of an individual LSCF particle with LSM coating after long-term operation; (g) Fourier-filtered image of the LSCF grain after operation preserving the perovskite structure; (h) convergent beam electron diffraction (CBED) pattern of the shell in (f) showing the loss of crystallinity. Reproduced from ref. 52 with permission from the Royal Society of Chemistry.

doped ceria (SDC) with intermediate TEC values have been used.[14,30,35–37] Segregation of alkaline earth elements, mainly Sr in LSCF materials, is a well-known phenomenon that has been extensively studied[38,39] and an example is shown in Fig. 2a and b. The mechanism of this phenomenon has been under investigation and two major driving forces have been proposed:

(i) The electrostatic interaction between the negatively charged Sr'_{La} and the positively charged oxygen vacancy attracts the Sr dopant to the surface specifically when there is a high concentration of oxygen vacancies.[40–43] The effect of oxygen partial pressure on Sr segregation behaviour has been investigated by Fister *et al.*[41] in an epitaxial $La_{0.7}Sr_{0.3}MnO_3$ thin film confirming as shown in Fig. 2c where Sr concentration increases on the surface when oxygen partial pressure is lower; and

(ii) Another important driving force for Sr segregation originates from the difference in Sr and La ionic size introducing elastic forces to the structure. Hence, Sr segregation occurs to minimize this elastic strain energy.[40–42,44] Wen *et al.*[40] studied the effect of temperature on Sr surface concentration in a $La_{1-x}Sr_xCo_{3-\delta}$ epitaxial film revealing a weak thermally activated Sr diffusion process following an Arrhenius law with a small activation energy (Fig. 2d). They could effectively suppress the Sr segregation using a ZrO_2 coating (Fig. 2d) because of the reduced surface oxygen vacancies due to the cation exchange between Zr and Co.[40]

Surface segregation of Sr under SOFC operating temperatures leads to the formation of insulating $SrO/Sr(OH)_2/SrCO_3$ that decreases the kinetics of oxygen surface diffusion, increases the area specific resistance (ASR) and subsequently increases the degradation of the cathode.[30,45–49] Experimental and theoretical studies have shown that Sr-segregation can be remarkably suppressed *via* surface modifications, doping higher valence cations in the B-site,[50] and doping larger elements to generate compressive strains.[30,51] In addition, designing novel structures such as nano-architectures with the infiltration/wet impregnation technique, and core–shell structures have been proposed to enhance the performance and decrease the degradation of the LSCF cathodes.[52,53] For example, a nanosized surface layer of $La_xSr_{1-x}MnO_{3-\delta}$ ($x = 0.8$ and 0.85) has been fabricated *via* the infiltration technique on $La_{0.6}Sr_{0.4}Co_{0.2}Fe_{0.8}O_{3-\delta}$ (Fig. 2e–h) leading to inhibition of Sr segregation and enhancement of surface electrocatalytic activity.[52,53]

Undesirable reactions of the cathode with contaminants (contaminant poisoning) can cause serious degradation of SOFCs. Degradation mechanisms of cathodes have been reviewed in previous studies[54,55] and a surface functionalization strategy has been proposed to make contaminant-tolerant LSCF cathodes. For example, BaO infiltrated $La_{0.6}Sr_{0.4}Co_{0.2}Fe_{0.8}O_{3-\delta}$ cathode demonstrated Cr poisoning resistance due to the formation of $BaCrO_4$ instead of $SrCrO_4$.[56] Similarly, infiltration has been used to make the $BaCeO_3$–$La_{0.6}Sr_{0.4}Co_{0.2}Fe_{0.8}O_{3-\delta}$ architecture with enhanced tolerance towards S poisoning by the formation of $BaSO_4$ instead of $SrSO_4$.[57]

In addition to LSCF perovskites, several other La-containing compositions have been developed using A or B-site dopants such as Ba,[58,59] Cu,[60–67] Ni,[68,69] Mo,[70] and Ca[71,72] demonstrating a range of properties summarized in Table 2. A series of $La_{1-x}Ba_xCo_{0.2}Fe_{0.8}O_{3-\delta}$ (LBCF) compositions have been investigated for application in IT-SOFC cathodes showing lower electrical conductivities than their LSCF counterparts,[58,59] with a maximum value of 100 S cm^{-1} in the temperature range of RT-1000 °C for $La_{0.6}Ba_{0.4}Co_{0.2}Fe_{0.8}O_{3-\delta}$.[58] However, the main advantage of this family is their high resistance to Cr poisoning and good polarization performance stability compared to conventional LSM and LSCF cathodes.[73] Cu-doped compositions such as $La_{0.6}Sr_{0.4}Co_{1-y}Cu_yO_{3-\delta}$,[60] $La_{1-y}Sr_yMn_{1-x}Cu_xO_{3-\delta}$,[61,64] and $La_xSr_{1-x}Fe_{1-y}Cu_yO_{3-\delta}$[62,63,65,66,74] have been investigated. Specifically, Co-free compositions with Cu have attracted much attention due to the decreased cost and TEC and sufficient catalytic activity.[31,62,74,75] The Co-free composition of $La_{0.7}Sr_{0.3}Ti_{0.1}Fe_{0.6}Ni_{0.3}O_{3-\delta}$ was prepared using Ni and Ti as B-site dopants demonstrating high electrical conductivity (318 S cm^{-1} at 700 °C), low polarization resistance and good stability in both oxidizing and reducing environments, which are desirable for application in symmetrical SOFCs.[68] Using Ni and Fe in B-sites and La in A-sites, TEC value decreased to 11.4×10^{-6} K^{-1} in $LaNi_{0.6}Fe_{0.4}O_3$ in the temperature range of 30–1000 °C and an electrical conductivity of 580 S cm^{-1} at 800 °C was achieved.[69] The Mo-doped composition of $La_{0.5}Sr_{0.5}Fe_{0.9}Mo_{0.1}O_{3-\delta}$ also showed a lower TEC value of 13.2×10^{-6} K^{-1} at 300–600 °C with good structural stability in both oxidizing and reducing atmospheres.[70] The Ca-doped Sr/Co-free composition of $La_{0.65}Ca_{0.35}FeO_{3-\delta}$ has been prepared showing a high oxygen permeation flux and electrical conductivity reaching ~100 S cm^{-1} at 600–800 °C.[71,72]

By replacing La with other lanthanides including Pr,[70,74,76–79] Nd,[70,74,76,79–82] Sm[74,76,79,83–89] and Gd,[74,76,77,79] a variety of perovskite compositions can be generated in which the A site is occupied partly by a Ln element together with Sr or Ca, and the B site is occupied with transition metals such as Co, Fe, Mn, Cu and Mo. In the lanthanide family, the ionic size decreases moving from La to Pr, Nd, Sm and Gd leading to a lower ionicity of Ln–O bonds.[76] This change is beneficial to decrease the thermal mismatch of the cathode with common electrolytes by decreasing the TEC of the cathode. However, the electronic conductivity and electrochemical performance will be sacrificed (Fig. 3).[70,76,81,90,91]

Another important family of single perovskites for IT-SOFC cathodes are alkaline-earth based compositions including Sr- and/or Ba-based[92–95] compounds. Several compositions based on $SrCoO_{3-\delta}$ doped with Nb such as $SrNb_{0.1}Co_{0.9}O_{3-\delta}$,[96–100] $SrNb_{0.2}Co_{0.8}O_{3-\delta}$ [101] and A-site deficient $Sr_{0.95}Nb_{0.1}Co_{0.9}O_{3-\delta}$ [102]) have been investigated. These perovskites showed high electrical conductivity and good phase structure stability.[96,97] A nanoscale layer of $SrNb_{0.1}Co_{0.9}O_{3-\delta}$ was coated on a $(La_{0.6}Sr_{0.4})_{0.95}(Co_{0.2}Fe_{0.8})O_{3-\delta}$ cathode and demonstrated an improved ORR activity compared to the non-coated electrode.[100] Ta-doped compositions, $SrCo_{1-x}Ta_xO_{3-\delta}$, are another subgroup in this class of perovskites.[99,101,103,104] It was found that doping small amounts of Ta (20 mol%) stabilizes the crystal structure and enhances the ORR activity.[103] These changes were attributed to the increased oxygen surface exchange originating from the effects of Ta^{5+} on the oxidation states of Co ions.[103] Wang *et al.*[104] compared different properties of a $SrTa_{0.1}Co_{0.9}O_{3-\delta}$

Table 2 Summary of the most important properties of IT-SOFC perovskites[15,28,59,61–72,74,76–78,80–82,84,86,92–97,99–104,106–108,122,124,125,127,129–131,136–143a]

	Conductivity (S cm^{-1})			Cell performance		
Composition	σ_e	σ_i	TEC ($\times 10^{-6}$ K^{-1})	Electrolyte	R_p (Ω cm^2)	ASR (Ω cm^2)
$La_{0.8}Sr_{0.2}MnO_{3-\delta}$ (ref. 15, 28 and 136–138)	180 (700 °C) 300 (900 °C)	5.93×10^{-7} (900 °C)	11–13 (30–1000 °C)	—	—	—
$La_{1-x}Sr_xFeO_{3-\delta}$ (ref. 15 and 28)	129–369 (500–900 °C)	$0.205–5.6 \times 10^{-3}$ (500–900 °C)	12.2 (30–1000 °C)	—	—	—
$La_{1-x}Sr_xCoO_{3-\delta}$ (ref. 15, 28 and 139)	1200–1360 (500–900 °C)	0.22 (500–900 °C)	18–20 (300–750 °C)	SDC	1.0825 ($x = 0.3$, 0.4)	—
$La_{0.6}Sr_{0.4}CoO_{3-\delta}$ (ref. 76)	~1990–2820 (300–750 °C)	—	21.3 (50–800 °C)	LSGM	—	—
$La_{0.6}Sr_{0.4}Co_{0.2}Fe_{0.8}O_{3-\delta}$ (ref. 59, 140 and 141)	~252–330 (300–900 °C)	0.23 (900 °C)	15.3 (100–600 °C)	GDC	0.04 (800 °C)	—
$La_{0.4}Sr_{0.6}Co_{0.2}Fe_{0.8}O_{3-\delta}$ (ref. 59 and 140)	219 (900 °C)	0.4 (900 °C)	16.8 (100–400 C)	—	—	—
$La_{0.2}Sr_{0.8}Co_{0.2}Fe_{0.8}O_{3-\delta}$ (ref. 59)	120 (900 °C)	0.62 (900 °C)	—	—	—	—
$La_{0.2}Sr_{0.8}Co_{0.8}Fe_{0.2}O_{3-\delta}$ (ref. 59)	310 (900 °C)	0.87 (900 °C)	—	—	—	—
$La_{0.8}Sr_{0.2}Co_{0.8}Fe_{0.2}O_{3-\delta}$ (ref. 142)	~825–1000 (300–800 °C)	—	20.7 (100–900 °C)	—	—	—
$La_{0.8}Sr_{0.2}Co_{0.2}Fe_{0.8}O_{3-\delta}$ (ref. 142)	~100–150 (300–800 °C)	—	15.4 (100–800 °C)	—	—	—
$La_{0.9}Sr_{0.1}Co_{0.2}Fe_{0.8}O_{3-\delta}$ (ref. 140)	~15–60 (300–800 °C)	—	16 (300–900 °C)	—	—	—
$La_{0.6}Ba_{0.4}Co_{0.2}Fe_{0.8}O_{3-\delta}$ (ref. 58, 59 and 143)	100 (750 °C) 123 (900 °C)	0.01 (900 °C)	—	—	—	—
$La_{0.6}Ba_{0.4}Co_{0.2}Fe_{0.8}O_{3-\delta}$ (ref. 59)	123 (900 °C)	0.01 (900 °C)	—	—	—	—
$La_{0.4}Ba_{0.6}Co_{0.2}Fe_{0.8}O_{3-\delta}$ (ref. 59)	57 (900 °C)	0.33 (900 °C)	—	—	—	—
$La_{0.2}Ba_{0.8}Co_{0.2}Fe_{0.8}O_{3-\delta}$ (ref. 59)	19 (900 °C)	0.37 (900 °C)	—	—	—	—
$La_{0.54}Sr_{0.46}Fe_{0.8}Cu_{0.2}O_{3-\delta}$ (ref. 62)	9.029 (600 °C)	—	—	SDC	—	—
$La_{0.5}Sr_{0.5}Fe_{0.8}Cu_{0.2}O_{3-\delta}$ (ref. 66)	300 (500 °C)	—	15.8(9) (30–850 °C)	GDC	—	1.15 (600 °C)
$La_{0.5}Sr_{0.5}Fe_{0.8}Cu_{0.2}O_{3-\delta}$ (ref. 65)	—	—	17.7 (25–900 °C)	SDC	0.4 (700 °C)	—
$La_{0.6}Sr_{0.4}Fe_{0.8}Cu_{0.2}O_{3-\delta}$ (ref. 63)	190–238 (600–800 °C)	—	14.6 (RT-850 °C)	SDC	0.138 (750 °C)	
$La_{0.54}Sr_{0.46}Fe_{0.8}Cu_{0.2}O_{3-\delta}$ (ref. 62)	9.029 (600 °C)	—	—	SDC	—	—
$La_{0.7}Sr_{0.3}Mn_{0.8}Cu_{0.2}O_{3-\delta}$ (ref. 61)	208.4 (750 °C)	—	—	—	—	—
$La_{0.8}Sr_{0.2}Mn_{0.8}Cu_{0.2}O_{3-\delta}$ (ref. 64)	190 (750 °C)	—	—	YSZ	—	4.3 (750 °C)
$La_{0.8}Sr_{0.2}Fe_{0.8}Cu_{0.2}O_{3-\delta}$ (ref. 67)	184–150 (550–750 °C)	—	—	LSGM	—	0.25 (750 °C)
$La_{0.7}Sr_{0.3}Ti_{0.1}Fe_{0.6}Ni_{0.3}O_{3-\delta}$ (ref. 68)	318 (700 °C)	—	—	LSGM	0.185 (700 °C)	—
$LaNi_{0.6}Fe_{0.4}O_3$ (ref. 69)	580 (800 °C)	—	11.4 (30–1000 °C)	—	—	—
$La_{0.5}Sr_{0.5}Fe_{0.9}Mo_{0.1}O_{3-\delta}$ (ref. 70)	73–70 (600–800 °C)		14 (300–900 °C)	SDC	0.25 (700 °C)	—
$La_{0.65}Ca_{0.35}FeO_{3-\delta}$ (ref. 72)	~100 (600–800 °C)	—	—	—	—	—
$La_{0.65}Ca_{0.35}FeO_{3-\delta}$ (ref. 71 and 72)	100–200 (600 °C)	—	—	YSZ/GDC	0.255 (700 °C)	—
$La_{0.4}Ca_{0.6}Co_{0.2}Fe_{0.8}O_{3-\delta}$ (ref. 59)	52 (900 °C)	0.03 (900 °C)	—	—	—	—
$La_{0.4}Ca_{0.6}Co_{0.8}Fe_{0.2}O_{3-\delta}$ (ref. 59)	296 (900 °C)	0.01 (900 °C)	—	—	—	—
$Pr_{0.5}Sr_{0.5}Fe_{0.9}Mo_{0.1}O_{3-\delta}$ (ref. 70)	59–53 (600–800 °C)	—	13.6 (300–900 °C)	SDC	0.5 (700 °C)	—
$Pr_{0.5}Sr_{0.5}Fe_{0.8}Cu_{0.2}O_{3-\delta}$ (ref. 74)	~60–140 (300–750 °C)	—	17.3 (RT-800 °C)	SDC	0.036 (800 °C)	—
$Pr_{0.6}Sr_{0.4}CoO_{3-\delta}$ (ref. 76)	~2400–1780 (300–750 °C)	—	19.5 (50–800 °C)	LSGM	—	—
$Pr_{0.8}Sr_{0.2}Fe_{0.8}Co_{0.2}O_{3-\delta}$ (ref. 78)	75.8 (800 °C)	1.54×10^{-3} (800 °C)	12.8 (30–1000 °C)	—	—	—
$Pr_{0.8}Sr_{0.2}Mn_{0.8}Co_{0.2}O_{3-\delta}$ (ref. 78)	83.17 (800 °C)	3×10^{-5} (800 °C)	10.9 (30–1000 °C)	—	—	—
$Pr_{0.65}Sr_{0.3}MnO_{3-\delta}$ (ref. 78)	208.92 (800 °C)	3.4×10^{-4} (800 °C)	11.6 (30–1000 °C)	—	—	—
$Nd_{0.9}Sr_{0.1}Fe_{0.1}Co_{0.9}O_{3-\delta}$ (ref. 80)	0.137 (600 °C)	—	—	—	—	—
$Nd_{0.5}Sr_{0.5}Fe_{0.9}Mo_{0.1}O_{3-\delta}$ (ref. 70)	63–65 (600–800 °C)	—	13.3 (300–900 °C)	SDC	0.44 (700 °C)	—
$Nd_{0.5}Sr_{0.5}Fe_{0.8}Cu_{0.2}O_{3-\delta}$ (ref. 74)	~40–100 (300–750 °C)	—	17.19 (RT-800 °C)	SDC	0.089 (800 °C)	—
$Nd_{0.75}Sr_{0.25}Fe_{0.2}Co_{0.8}O_{3-\delta}$ (ref. 81)	30 (700 °C)	—	—	LSGM	—	0.1 (800 °C)
$Nd_{0.6}Sr_{0.4}CoO_{3-\delta}$ (ref. 76)	~2240–1400 (300–750 °C)	—	18.7 (50–800 °C)	LSGM	—	—

Table 2 (*Contd.*)

Composition	Conductivity (S cm^{-1})		TEC ($\times 10^{-6}$ K^{-1})	Cell performance		
	σ_e	σ_i		Electrolyte	R_p (Ω cm^2)	ASR (Ω cm^2)
$Nd_{0.5}Sr_{0.5}Fe_{0.8}Cu_{0.2}O_{3-\delta}$ (ref. 82)	124 (700 °C)	—	14.7 (25–800 °C)	SDC	0.071 (700 °C)	—
$Sm_{0.5}Sr_{0.5}Fe_{0.8}Cu_{0.2}O_{3-\delta}$ (ref. 74)	~40–80 (300–750 °C)	—	16.72 (RT-800 °C)	SDC	0.097 (800 °C)	—
$Sm_{0.6}Sr_{0.4}CoO_{3-\delta}$ (ref. 76)	~1950–1320 (300–750 °C)	—	18 (50–800 °C)	LSGM	—	—
$Sm_{0.3}Sr_{0.7}Nb_{0.08}Co_{0.92}O_{3-\delta}$ (ref. 84)	315 (350 °C)	—	—	SDC	—	0.062 (600 °C)
$Sm_{0.5}Sr_{0.5}Fe_{0.8}Cr_{0.2}O_{3-\delta}$ (ref. 86)	7.32 (766 °C)	—	4.7 (100–800 °C)	—	—	—
$Gd_{0.5}Sr_{0.5}Fe_{0.8}Cu_{0.2}O_{3-\delta}$ (ref. 74)	~25–35 (300–750 °C)	—	12.89 (RT-800 °C)	SDC	0.16 (800 °C)	—
$Gd_{0.6}Sr_{0.4}CoO_{3-\delta}$ (ref. 76)	~1260–890 (300–750 °C)	—	17.1 (50–800 °C)	LSGM	—	—
$Gd_{0.5}Sr_{0.5}CoO_3$ (ref. 77)	—	—	—	CGO	—	0.1–0.2 (650 °C)
$Ba_{0.9}Co_{0.7}Fe_{0.2}Ni_{0.1}O_{3-\delta}$ (ref. 92)	—	—	—	GDC	0.046 (600 °C)	
$Ba_{0.9}Co_{0.7}Fe_{0.2}Nb_{0.1}O_{3-\delta}$ (ref. 93)	13.9 (700 °C)	—	13.2 (600 °C)	LSGM	0.07 (700 °C)	—
$Ba_{0.5}Sr_{0.5}Zn_{0.2}Fe_{0.8}O_{3-\delta}$ (ref. 94)	9.4 (590 °C)	—	—	SDC	0.48 (650 °C)	—
$Ba_{0.9}Sr_{0.1}Co_{0.9}In_{0.1}O_{3-\delta}$ (ref. 95)	8.7–13.6 (600–800 °C)	—	17.04 (30–1000 °C)	SDC	—	0.079 (700 °C)
$SrNb_{0.1}Co_{0.9}O_{3-\delta}$ (ref. 96)	~135–75 (350–700 °C)	—	—	SDC	—	0.040 (650 °C) 0.094 (600 °C)
$SrNb_{0.1}Co_{0.9}O_{3-\delta}$ (ref. 97)	461–145 (300–800 °C)	—	24.2 (30–1000 °C)	LSGM	—	0.21 (650 °C)
$Sr_{0.95}Nb_{0.1}Co_{0.9}O_{3-\delta}$ (ref. 102)	276–129 (450–750 °C)	—	95.8 (25–800 °C)	SDC	—	0.052 (500 °C)
$SrNb_{0.1}Co_{0.9}O_{3-\delta}$ (ref. 99)	—	0.34 (650 °C)	—	—	—	—
$SrNb_{0.2}Co_{0.8}O_{3-\delta}$ (ref. 101)	~155–105 (400–700 °C)	0.28 (700 °C)	—	SDC	—	0.21–0.24 (550 °C)
$SrTa_{0.2}Co_{0.8}O_{3-\delta}$ (ref. 101)	~150–100 (400–700 °C)	0.31 (700 °C)	—	SDC	—	0.092–0.097 (550 °C)
$SrTa_{0.05}Co_{0.95}O_{3-\delta}$ (ref. 103)	590–210 (400–700 °C)	—	—	SDC	—	0.11–0.089 (550 °C)
$SrTa_{0.1}Co_{0.9}O_{3-\delta}$ (ref. 99)	—	0.17 (650 °C)	—	—	—	—
$SrTa_{0.1}Co_{0.9}O_{3-\delta}$ (ref. 104)	~325–175 (550–700 °C)	—	23.6 (500–900 °C)	—	—	—
$SrCo_{0.95}Ti_{0.05}O_{3-\delta}$ (ref. 107)	268–160 (600–800 °C)	—	21.2 (30–1000 °C)	LSGM	—	0.17 (700 °C)
$SrCo_{0.95}Ti_{0.05}O_{3-\delta}$ (ref. 106)	>150 (600 °C)	—	25.28 (400–850 °C)	LSGM	—	0.016 (850 °C)
$SrCo_{0.97}V_{0.03}O_{3-\delta}$ (ref. 106)	>4 (600 °C)	—	13.40 (400–850 °C)	LSGM	—	0.025 (850 °C)
$Sr_{0.7}Y_{0.3}CoO_{2.65-\delta}$ (ref. 108)	735 (650 °C)	—	19.6 (25–800 °C)	LSGM	—	0.11 (800 °C)
$Bi_{0.5}Sr_{0.5}Fe_{0.8}Co_{0.2}O_{3-\delta}$ (ref. 124)	19.5–25.1 (600–800 °C)	—	12.2–14.7 (300–800 °C)	SDC	—	0.086 (700 °C)
$Bi_{0.5}Sr_{0.5}Fe_{0.85}Ti_{0.15}O_{3-\delta}$ (ref. 125)	0.6–2.4 (300–800 °C)	—	13.4 (50–800 °C)	CGO	0.085 (700 °C)	—
$Bi_{0.5}Sr_{0.5}Fe_{0.9}Sn_{0.1}O_{3-\delta}$ (ref. 127)	—	—	12.9 (50–800 °C)	CGO	0.09 (700 °C)	—
$Bi_{0.5}Sr_{0.5}Fe_{0.95}P_{0.05}O_{3-\delta}$ (ref. 122)	—	—	13.5 (50–800 °C)	GDC	0.18 (700 °C)	—
$SrFe_{0.9}Si_{0.1}O_{3-\delta}$ + 50 wt% $Gd_{0.1}Ce_{0.9}O_{1.95}$ (ref. 129)	~25–50 (300–800 °C)	—	—	—	—	0.08 (800 °C)
$La_{0.6}Sr_{0.4}Co_{0.76}Fe_{0.19}B_{0.05}O_{3-\delta}$ + 50 wt% $Gd_{0.1}Ce_{0.9}O_{1.95}$ (ref. 130)	1253–1096 (600–800 °C)	—	—	—	—	0.08 (800 °C)
$La_{0.6}Sr_{0.4}Co_{0.78}Fe_{0.195}Si_{0.025}O_{3-\delta}$ + 50 wt% $Gd_{0.1}Ce_{0.9}O_{1.95}$ (ref. 130)	853–682 (600–800 °C)	—	—	GDC	—	0.11 (800 °C)
$Ba_{0.95}La_{0.05}Fe_{0.95}P_{0.05}O_{3-\delta}$ (ref. 131)	~14–7 (500–750 °C)	—	25.48 (100–800 °C)	SDC	—	0.023 (700 C)

[a] SDC: samarium-doped ceria, LSGM: lanthanum strontium gallium magnesium oxide, GDC/CGO: gadolinium-doped ceria.

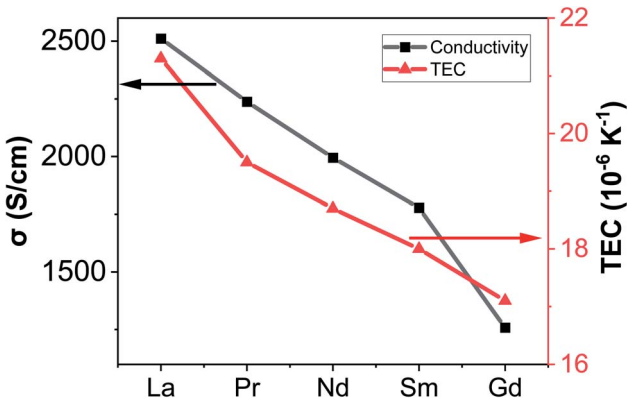

Fig. 3 Variation of DC electrical conductivity (σ) and thermal expansion coefficient (TEC) in $Ln_{0.6}Sr_{0.4}CoO_{3-\delta}$ (Ln = La, Pr, Nd, Sm and Gd) in air. Values are extracted from ref. 70, 76, 81, 90 and 91.

cathode with a $SrNb_{0.1}Co_{0.9}O_{3-\delta}$ material and proved that the Ta-doped counterpart shows better thermal and electrochemical stability due to the stronger Ta–O bonds.[104] In another interesting study, a nanoscale $SrTa_{0.1}Co_{0.9}O_{3-\delta}$ layer was used as the capping layer on a commercial $(La_{0.6}Sr_{0.4})_{0.95}(Co_{0.2}Fe_{0.8})O_{3-\delta}$-GDC composite.[105] This cathode showed excellent Cr-resistant properties with a good ORR activity. SrO-free surface of this cathode showed a much lower polarization resistance and degradation rate compared to the uncoated cathode.[105] $SrCoO_{3-\delta}$ doped with other elements such as Ti/V[106,107] and Y[108] has also been studied. Ti doping stabilized the crystal structure, improved the electrical conductivity, and decreased the polarization resistance[106,107] while V-doped compositions showed much lower TEC values.[108]

Co-free Sr-based compounds have also been investigated, mainly based on a strontium ferrite ($SrFeO_{3-\delta}$) composition with dopants such as Nb,[109–112] Ti,[113] Zr[114] and Cu[115] on B-sites.[15] Other Sr-based compositions such as $Sr_{1-x}Ce_xMnO_3$ [15,116] and $SrZr_{1-x}Ni_xO_3$ have also been investigated.[15,78,117] Ba-based compositions are another group of single perovskite cathodes. $Ba_{1-x}Sr_xCo_{1-y}Fe_yO_{3-\delta}$ (BSCF) compositions have shown good electrochemical performance at low temperatures,[118] however, they suffer from poor stability towards CO_2 originating from the susceptibility of alkaline-earth elements in reaction with CO_2.[119] The B-site doping strategy has been used to enhance either the electrochemical performance or structural stability of the perovskite using Nb,[92,93] Ln,[120] Ni,[92] and In.[95] Co-free compositions have also been prepared such as $Ba_{1-x}Sr_xFe_{1-y}Mo_yO_{3-\delta}$ [31,121] and $Ba_{1-x}Sr_xFe_{1-y}Zn_yO_{3-\delta}$ [94]) demonstrating promising performance as an IT-SOFC cathode.

Bismuth-based perovskites are novel compositions that have been recently investigated by several researchers showing promising performance as IT-SOFC cathodes.[122–127] Replacing Ba^{2+} with Bi^{3+} increases the structural stability at the operating temperatures.[124,126,128] Moreover, owing to its 6s lone electron pair, Bi^{3+} demonstrates high polarizability, enhancing the mobility of oxygen vacancies.[124] Bismuth strontium ferrites have been designed as a new family of Co-free perovskites with low area-specific resistance, high oxygen flux density and improved kinetics of surface exchange reactions.[127] However, the reported conductivity values are still not sufficient for an IT-SOFC cathode. Another novel concept that has been introduced recently is using non-metal dopants such as Si,[129,130] P[122,130,131] and B.[130] Slater *et al.*[132] reported the successful incorporation of Si into the structures of $SrCoO_{3-\delta}$ and $SrMnO_{3-\delta}$. They reported a higher conductivity for the Si-doped perovskites due to the transformation from a hexagonal structure into a cubic perovskite.[132] A similar observation was reported for a phosphate/sulfate-doped $SrCoO_{3-\delta}$ and the improvement in the conductivity was attributed to the change from a 2H- to 3C-perovskite.[133] The latter phase was found to be metastable when annealing at intermediate temperatures, however, co-doping with Fe was found to improve the stability.[133] The same group reported the synthesis of a Si-doped $SrFeO_{3-\delta}$ with an enhanced conductivity compared to the undoped structure attributed to the change of the crystal structure from a tetragonal symmetry to a cubic perovskite with disordered oxygen vacancies.[129] They also showed that increasing the Si level to higher than 10% decreases the conductivity due to the blocking effect of Si on electronic conduction pathways.[129] Doping silicate, borate, and phosphate into $La_{0.6}Sr_{0.4}Co_{0.8}Fe_{0.2}O_{3-\delta}$ and $Sr_{0.9}Y_{0.1}CoO_{3-\delta}$ compositions have been reported.[130] Introduction of oxide ion vacancies by oxyanion doping was found to be responsible for the improvement of the electronic conductivity in doped $La_{0.6}Sr_{0.4}Co_{0.8}Fe_{0.2}O_{3-\delta}$ material. However, in the case of $Sr_{0.9}Y_{0.1}CoO_{3-\delta}$, oxyanion doping decreased the electronic conductivity due to the disruption of conduction pathways.[130] Interestingly, oxyanion doping of both compositions improved the stability towards CO_2 and the observation was attributed to the decrease in the basicity of the system by introduction of acidic dopants.[130]

Stabilization of the cubic perovskite structure has also been observed when phosphate and borate were incorporated into the $Ba_{1-x}Sr_xCo_{0.8}Fe_{0.2}O_{3-\delta}$ material with a small improvement of the electronic conductivity for low levels of dopants.[134] However, borate-doped $La_{1-x}Sr_xMnO_{3-\delta}$ resulted in a lower electronic conductivity in comparison with the undoped material because of the lower concentration of Mn^{4+} in the doped-sample.[135] P-doped $Ba_{0.95}La_{0.05}Fe_{0.95}P_{0.05}O_{3-\delta}$ resulted in an enhancement in the electrical conductivity as well as a better electrocatalytic activity.[131] DFT studies predicted a lower formation energy of oxygen vacancies and migration barrier by introduction of P into the structure. Experimental results further confirmed the DFT findings and showed that P-doing into the Fe sites increases the surface exchange rate and the diffusion coefficient in a symmetrical cell leading to an improved ORR performance.[131] Similar observations have been reported for a P-doped (Bi, Sr)$FeO_{3-\delta}$ cathode.[122] Table 2 summarizes the properties of different LSCF compositions along with other perovskite-type SOFC cathodes.[15,28,59,61–72,74,76–78,80–82,84,86,92–97,99–104,106–108,122,124,125,127,129–131,136–143]

Double perovskite-type structure SOFC cathodes

Oxygen deficient double perovskite oxides are gaining prominent attention as oxygen electrodes in intermediate

temperature SOFCs due to their enhanced catalytic properties, oxygen transport, and stability over single perovskite oxides.[144,145] Their compositional formula is generally represented by $AA'BB'O_{5+\delta}$, where the A-site ion is a rare-earth element, A′ is an alkali or alkaline earth metal, B and B′ are transition metals and O is oxygen. They consist of alternating layers of $[AO_\delta]$–[BO]–[A′O]–[BO], where oxygen vacancies, δ, are majorly localised in the $[AO_\delta]$ planes. The concentration of oxygen vacancies within their sublattices facilitates the rapid diffusion of oxygen ions, giving rise to superior electrochemical performances.

Double perovskite crystal structure

Double perovskite oxides possess the same crystal structure as single perovskites. Their unit cell size depends on the ordering of the A, A′, B and/or B′ cations in the sublattices. On investigating the relationship between A- and B-site cation ordering, Knapp and Woodward observed that while A-site cation ordering was inclined to occur in a layered manner, B-site cation ordering usually assumes a rock salt structure.[146] In the layered structure, A and A′ cations alternately occupy the same crystallographic site. This alternate arrangement is favoured by a substantial difference between the ionic radii and/or charge of

Table 3 Summary of the crystallographic parameters and room temperature oxygen stoichiometry of selected IT-SOFC double perovskite cathodes[152,155–180,186]

Composition	Space group	Cell constants				Oxygen contents $(5+\delta)$
		a (Å)	b (Å)	c (Å)	V (Å^3)	
$LaBaCo_2O_{5+\delta}$ (ref. 152)	$Pm\bar{3}m$	3.881	—	—	58.456	6.00
$LaBaCoCuO_{5+\delta}$ (ref. 160)	$Pmmm$	3.922	3.9360	11.7073	180.74	—
$LaBaCuFeO_{5+\delta}$ (ref. 161)	$Immm$	5.5586	5.5550	7.8155	241.33	—
$LaSrMnCoO_{5+\delta}$ (ref. 162)	$Fm3m$	7.6891	—	—	454.597	
$PrBaCo_2O_{5+\delta}$ (ref. 163)	$P4/mmm$	3.909	—	7.638	116.8	5.64
$PrBaCoFeO_{5+\delta}$ (ref. 164)	$P4/mmm$	3.9184	—	7.6568	117.56	5.79
$PrBaCo_{2/3}Fe_{2/3}Cu_{2/3}O_{5+\delta}$ (ref. 165)	$P4/mmm$	3.904	—	7.651	116.63	—
$PrBaFe_2O_{5+\delta}$ (ref. 166)	$Pmmm$	3.928	3.934	7.794	120.46	5.884
$PrBa_{0.5}Sr_{0.5}Co_2O_{5+\delta}$ (ref. 167)	$P4/mmm$	7.758	—	7.704	463.70	5.498
$PrBa_{0.5}Sr_{0.5}Co_{1.5}Fe_{0.5}O_{5+\delta}$ (ref. 168)	$P4/mmm$	3.871	—	7.757	116.212	6.00
$PrBa_{0.5}Sr_{0.5}CoFeO_{5+\delta}$ (ref. 168)	$P4/mmm$	3.875	—	7.767	116.652	6.00
$PrBa_{0.8}Ca_{0.2}Co_{1.5}Fe_{0.5}O_{5+\delta}$ (ref. 169)	$P4/mmm$	3.871	—	7.703	115.421	5.81
$NdBaCo_2O_{5+\delta}$ (ref. 170)	$P4/mmm$	3.896	—	7.619	115.65	5.85
$NdBaCoCuO_{5+\delta}$ (ref. 171)	$P4/mmm$	3.920	—	7.683	118.049	5.782
$NdBaCoFeO_{5+\delta}$ (ref. 164)	$P4/mmm$	3.9090	—	7.6252	116.526	5.67
$NdBaCo_{2/3}Fe_{2/3}Cu_{2/3}O_{5+\delta}$ (ref. 172)	$P4/mmm$	3.923	—	7.696	118.5	5.44
$NdBaCo_{1.6}Ni_{0.4}O_{5+\delta}$ (ref. 173)	$P4/mmm$	3.9022	—	7.6200	116.03	—
$NdBaFe_2O_{5+\delta}$ (ref. 170)	$Pm\bar{3}m$	3.930	—	—	60.70	—
$NdBa_{0.5}Sr_{0.5}CoCuO_{5+\delta}$ (ref. 171)	$P4/mmm$	3.871	—	7.664	114.851	5.789
$NdBa_{0.5}Sr_{0.5}CoFeO_{5+\delta}$ (ref. 168)	$P4/mmm$	3.864	—	7.718	115.226	6.00
$NdBa_{0.5}Sr_{0.5}Co_2O_{5+\delta}$ (ref. 167)	$P4/mmm$	7.669	—	7.685	452.0	5.235
$NdSrCo_2O_{5+\delta}$ (ref. 174)	$Pbnm$	5.3740	5.4201	7.6020	221.443	6.00
$SmBaCo_2O_{5+\delta}$ (ref. 175)	$Pmmm$	3.889	7.839	7.563	230.22	5.62
$SmBaCo_{1.6}Fe_{0.4}O_{5+\delta}$ (ref. 175)	$Pmmm$	3.888	7.826	7.599	231.29	—
$SmBaCo_{0.5}Mn_{1.5}O_{5+\delta}$ (ref. 176)	$Cmmm$	7.736	7.799	7.692	464.07	5.98
$SmBaCo_{1.6}Ni_{0.4}O_{5+\delta}$ (ref. 173)	$Pmmm$	0.392	0.389	0.758	0.116	—
$SmSrCo_2O_{5+\delta}$ (ref. 177)	$Pbnm$	5.403	5.3830	7.6264	221.788	6.00
$YBaCo_2O_{5+\delta}$ (ref. 152)	$P4/mmm$	3.874	—	7.483	112.304	5.41
$YBaCo_{1.4}Cu_{0.6}O_{5+\delta}$ (ref. 178)	$P4/mmm$	11.658	—	7.546	1025.539	—
$YBaCo_{1.8}Fe_{0.2}O_{5+\delta}$ (ref. 179)	$P4/mmm$	3.8807	—	7.519	113.23	—
$EuBaCo_2O_{5+\delta}$ (ref. 180)	$P4/mmm$	3.882	—	7.541	229.36	5.40
$GdBaCo_2O_{5+\delta}$ (ref. 181)	$Pmmm$	3.876	3.912	7.541	114.367	5.61
$GdBaCoCuO_{5+\delta}$ (ref. 171)	$P4/mmm$	3.894	—	3.510	115.288	5.643
$GdBaCoFeO_{5+\delta}$ (ref. 170)	$P4/mmm$	3.903	—	7.643	116.43	6.00
$GdBaFeNiO_{5+\delta}$ (ref. 182)	$P4/mmm$	3.915	—	7.598	116.5	5.26
$GdBa_{0.5}Sr_{0.5}Co_2O_{5+\delta}$ (ref. 183)	$P4/mmm$	3.8624	—	7.5578	112.74	—
$GdBa_{0.5}Sr_{0.5}CoCuO_{5+\delta}$ (ref. 171)	$P4/mmm$	3.866	—	7.576	113.231′	5.66
$GdBa_{0.5}Sr_{0.5}CoFeO_{5+\delta}$ (ref. 183)	$P4/mmm$	3.8710	—	7.6368	114.43	—
$GdBa_{0.5}Sr_{0.5}Co_{1.5}Fe_{0.5}O_{5+\delta}$ (ref. 183 and 184)	$P4/mmm$	3.8596	—	7.5802	112.90	5.75
$GdSrCo_2O_{5+\delta}$ (ref. 181)	$Pnma$	5.373	7.572	5.402	219.763	6.00
$TbBaCo_2O_{5+\delta}$ (ref. 180)	$P4/mmm$	3.867	—	7.516	112.39	5.40
$DyBaCo_2O_{5+\delta}$ (ref. 180 and 185)	$P4/mmm$	3.879	—	7.505	112.95	5.30
$HoBaCo_2O_{5+\delta}$ (ref. 186)	$P4/mmm$	3.873	—	7.496	112.44	5.30

the elements which occupy the A and A′ sites.[147] To attain the layered structure, large atoms such as Ba are typically doped on the A′ site such as in the $REBaCo_2O_{5+\delta}$ (RE = Rare Earth) perovskites. The layered ordering of A-site cations in the $AA'B_2O_{5+\delta}$ perovskite leads to a tetragonal *P*4/*mmm* space group symmetry ($a_p \times a_p \times 2a$) where the unit cell is doubled along the *c*-axis.[148–150] In the case of an insignificant difference in the ionic radii, the perovskite oxide will lose the long-range ordering between the A and A′ cations resulting in randomly distributed A cations with a cubic structure ($Pm\bar{3}m$) as observed in $LaBaCo_2O_{5+\delta}$.[151,152] At a given temperature, the unit cell volume of $REBaCo_2O_{5+\delta}$ decreases with decreasing Ln^{3+} ionic radius.

The double perovskite can accommodate a large concentration of vacancies in the oxygen sublattice without structural collapse.[153] This occurs as a result of the distortion of the [BO] framework induced by the large size or charge difference between the A and A′ cations. To attain stability and/or electroneutrality, vacancies are created in the oxygen sublattice which cause the double perovskite stoichiometry to depart from $AA'BB'O_6$ to an oxygen-deficient double perovskite oxide, $AA'BB'O_{5+\delta}$ where $0 < \delta \leq 1$. These vacancies when ordered create a pathway for fast oxygen diffusion. Thus, this family of perovskite oxides provides mixed ionic and electronic conduction required for IT-SOFC cathodes. Taskin *et al.* discovered that transforming $Gd_{0.5}Ba_{0.5}MnO_{3-\delta}$ with randomly distributed Gd and Ba cations into a layered A site $GdBaMn_2O_{5+\delta}$ substantially enhanced the oxygen diffusivity.[154] In addition to cation ordering, oxygen vacancies directly influence the crystal system and lattice parameters of double perovskite oxides. Anderson *et al.* reported structural transition phases in $REBaCo_2O_{6-\delta}$ (RE = Pr^{3+} (1.13 Å), Nd^{3+} (1.11 Å), Sm^{3+} (1.08 Å), Eu^{3+} (1.07 Å), Gd^{3+} (1.05 Å), Tb^{3+} (1.04 Å), Dy^{3+} (1.027 Å), Ho^{3+} (1.02 Å)) perovskite oxide which corresponded with the ionic radius- and temperature-dependent oxygen non stoichiometry summarised in Table 3.[152,155–180,186] Several studies have reported a similar occurrence,[155–159] inferring that oxygen content fundamentally controls the structural symmetry of the $LnBaCo_2O_{5+\delta}$ series. Streule *et al.* suggested that structural transitions observed in double perovskites are related to the order/disorder of the oxygen vacancies.[149] When the ordering of oxygen vacancies occurs, the unit cell along the *b*-axis doubles, leading to the formation of an orthorhombic $a_p \times 2a_p \times 2a_p$ (*Pmmm*) structure. Thus, at certain perovskite oxide composition stoichiometries, vacancy ordering is observed within the sublattice. Since oxygen content varies with temperature, heating double perovskite oxide compositions to certain temperature ranges will drive a disorder in the arrangement of oxygen vacancies.

Double perovskite IT-SOFC cathodes: composition–structure–property relationship

Substantial efforts have been dedicated towards tuning the physical properties of double perovskite oxide catalysts through a systematic partial or complete substitution of the A and/or B sites. Whereas the A-site cation substitution primarily controls the electrochemical performance of the perovskite, B-site cation substitutions influence the electronic structure and catalytic activities of the perovskite oxides as the redox reactions occur on the B site. Studies that employ A-site cation substitution typically dope a trivalent lanthanide element with a larger divalent alkaline earth metal.[187–189] The most common A site doping is substituting lanthanide elements with Ba and/or Sr. The A-site layered $LnBaCo_2O_{5+\delta}$ (Ln = Pr, Nd, Sm, Eu, Gd, Tb, Dy, Ho, Y) series has been widely investigated.[151,152,155,185,190–193] This compositional family shows promising ionic transport properties, surface exchange kinetics and high electrical conductivities. Kim *et al.* reported a surface exchange rate coefficient, $k = 6.5 \times 10^{-5}$ cm s^{-1} and diffusion coefficient of oxygen ions, $D = 3.6 \times 10^{-7}$ cm^2 s^{-1} at 500 °C for $PrBaCo_2O_{5+\delta}$ (PBCO)[194] as compared to the widely known $La_{0.6}Sr_{0.4}Co_{0.2}Fe_{0.8}O_{3-\delta}$ (LSCF) cathode with $k = 3.3 \times 10^{-9}$ cm s^{-1} and $D = 1.2 \times 10^{-10}$ cm^2 s^{-1} at 500 °C.[195] They also reported ionic conductivity values of 0.056, 0.04 and 0.11 S cm^{-1} and total electrical conductivities of 700, 464 and 425 S cm^{-1} for $LnBaCo_2O_{5+\delta}$ (Ln = La, Nd, Sm) respectively at 900 °C.[155] Their results reveal that the ionic and electronic conductivities of $LnBaCo_2O_{5+\delta}$ decrease with decreasing Ln^{3+} size (Fig. 4a) due to the increase in the concentration of oxygen vacancies (Fig. 4b)

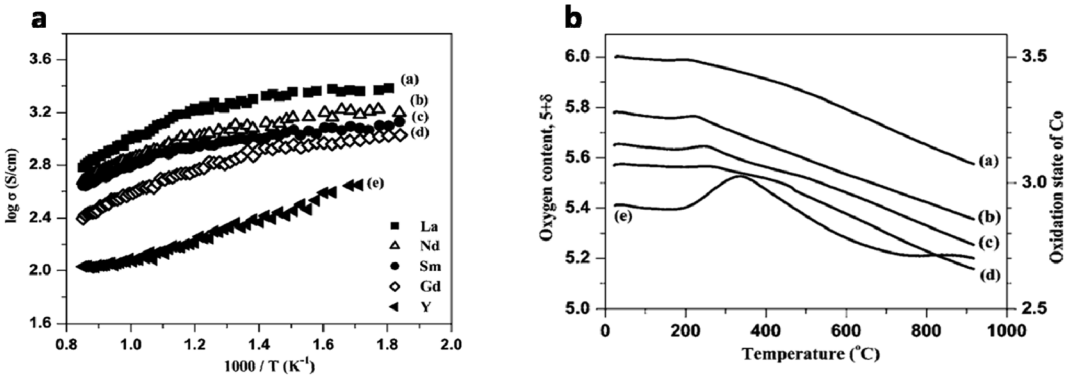

Fig. 4 (a) Temperature-dependent DC conductivity of $LnBaCo_2O_{5+\delta}$ (Ln = La, Nd, Sm, Gd, Y) samples in air. (b) Variation of oxygen content and cobalt oxidation state with temperature in air: (a) Ln = La, (b) Ln = Nd, (c) Ln = Sm, (d) Ln = Gd, (e) Ln = Y. Reproduced with permission.[152]

Table 4 Summary of the most important properties of selected IT-SOFC double perovskite cathodes[152,156–165,167,169–171,175–180,186,197,220,224,229–241]

	Conductivity (S cm^{-1})			Cell performance			
Composition	σ_e	σ_i	TEC ($\times 10^{-6}$ K^{-1})	Electrolyte	R_p (Ω cm^2)	ASR (Ω cm^2)	Power density (W cm^{-2})
$LaBaCo_2O_{5+\delta}$ (ref. 152 and 229)	1443 (600 °C)	—	24.3	SDC	—	0.056 (700 °C)	—
$LaBaCuCoO_{5+\delta}$ (ref. 220)	392 (600 °C)	—	—	SDC	—	0.11 (700 °C)	0.60 (800 °C)
$LaBaCuFeO_{5+\delta}$ (ref. 220)	123 (600 °C)	—	—	SDC	—	0.21 (700 °C)	0.56 (800 °C)
$LaSrMnCoO_{5+\delta}$ (ref. 230)	111 (600 °C)	—	15.8	SDC	0.048 (800 °C)	—	0.565 (800 °C)
$PrBaCo_2O_{5+\delta}$ (ref. 163 and 224)	844 (600 °C)	—	20.4	LSGM	0.75 (700 °C)	0.061 (700 °C)	0.41 (800 °C)
$PrBaCoCuO_{5+\delta}$ (ref. 224)	144 (600 °C)	—	15.2	SDC	—	0.047 (700 °C)	0.79 (700 °C)
$PrBaCoFeO_{5+\delta}$ (ref. 164)	203 (600 °C)	—	21.0	LSGM	—	0.098 (750 °C)	0.75 (800 °C)
$PrBaFe_2O_{5+\delta}$ (ref. 166 and 231)	25.4 (600 °C)	—	17.2	SDC	0.48 (700 °C)	—	0.15 (650 °C)
$PrBaCo_{2/3}Fe_{2/3}Cu_{2/3}O_{5+\delta}$ (ref. 165)	144 (600 °C)	—	16.6	GDC	0.038 (800 °C)	—	0.659 (800 °C)
$PrSrCo_2O_{5+\delta}$ (ref. 197)	2084 (600 °C)	—	—	GDC	—		0.73 (600 °C)
$PrBa_{0.5}Sr_{0.5}Co_2O_{5+\delta}$ (ref. 167 and 197)	493 (600 °C)	—	—	GDC	—	0.44 (700 °C)	1.08 (600 °C)
$PrBa_{0.5}Sr_{0.5}Co_{1.5}Fe_{0.5}O_{5+\delta}$ (ref. 168)	—	—	—	GDC	—	0.056 (600 °C)	2.90 (650 °C)
$PrBa_{0.5}Sr_{0.5}CoFeO_{5+\delta}$ (ref. 232)	346 (600 °C)	—	20.9	GDC	0.077 (800 °C)		0.649 (850 °C)
$PrBa_{0.8}Ca_{0.2}Co_{1.5}Fe_{0.5}O_{5+\delta}$ (ref. 169)	—	—	20.28	GDC	0.080 (600 °C)	—	1.89 (600 °C)
$NdBaCo_2O_{5+\delta}$ (ref. 170)	776 (600 °C)	—	21.5	LSGM	—	0.70 (700 °C)	0.55 (800 °C)
$NdBaCoCuO_{5+\delta}$ (ref. 171)	99.2 (700 °C)	—	16.9	LSGM	—	0.28 (700 °C)	—
$NdBaCoFeO_{5+\delta}$ (ref. 164)	71 (600 °C)	—	19.5	LSGM	—	0.119 (750 °C)	0.67 (800 °C)
$NdBaCo_{2/3}Fe_{2/3}Cu_{2/3}O_{5+\delta}$ (ref. 172)	92 (625 °C)	—	15.7	LSGM	—	0.023 (800 °C)	0.719 (800 °C)
$NdBaCo_{1.6}Ni_{0.4}O_{5+\delta}$ (ref. 173)	654 (600 °C)	—	19.4	SDC	—	0.077 (700 °C)	0.714 (800 °C)
$NdBaFe_2O_{5+\delta}$ (ref. 170)	11.7 (600 °C)	—	18.3	LSGM	—	—	—
$NdBa_{0.5}Sr_{0.5}Co_2O_{5+\delta}$ (ref. 174)	2412 (600 °C)	—	—	GDC	—	0.112 (600 °C)	1.00 (600 °C)
$PrBa_{0.5}Sr_{0.5}CoCuO_{5+\delta}$ (ref. 233)	221 (850 °C)	—	17.58	GDC	0.06 (800 °C)	—	0.521 (800 °C)
$NdSrCo_2O_{5+\delta}$ (ref. 174)	2420 (600 °C)	—	—	GDC	—	0.05 (700 °C)	—
$SmBaCo_2O_{5+\delta}$ (ref. 175 and 234)	434 (800 °C)	—	21.1	LSGM	—	0.054 (750 °C)	0.777 (800 °C)
$SmBaCo_{1.6}Fe_{0.4}O_{5+\delta}$ (ref. 175)	342 (600 °C)	—	20.8	—	—	—	—
$SmBaCo_{0.5}Mn_{1.5}O_{5+\delta}$ (ref. 176)	28 (600 °C)	—	18.7	LSGM	0.081 (900 °C)	—	0.377 (850 °C)
$SmBaCo_{1.6}Ni_{0.4}O_{5+\delta}$ (ref. 173)	412 (600 °C)	—	16.6	SDC	—	0.11 (700 °C)	0.572 (800 °C)
$SmBa_{0.5}Sr_{0.5}Co_2O_{5+\delta}$ (ref. 235 and 236)	280 (900 °C)	—	21.9	GDC	0.092 (700 °C)	—	1.31 (800 °C)
$SmSrCo_2O_{5+\delta}$ (ref. 177 and 237)	2137 (600 °C)	—	22.7	GDC	—	0.28 (600 °C)	0.713 (600 °C)
$SmSrCoMnO_{5+\delta}$ (ref. 237)	45.9 (700 °C)	—	13.7	—	—	—	—
$YBaCo_2O_{5+\delta}$ (ref. 179)	189 (600 °C)	—	16.3	LSGMC	—	0.11 (700 °C)	0.873 (800 °C)
$YBaCo_{1.4}Cu_{0.6}O_{5+\delta}$ (ref. 178)	47.4 (700 °C)	—	14.7	LSGM	—	0.12 (700 °C)	0.642 (800 °C)
$YBaCo_{1.8}Fe_{0.2}O_{5+\delta}$ (ref. 179)	128 (600 °C)	—	17.3	LSGMC	—	0.13	0.768 (800 °C)
$YBa_{0.5}Sr_{0.5}Co_2O_{5+\delta}$ (ref. 238)	371 (600 °C)	—	—	GDC	—	0.36 (700 °C)	—
$GdBaCo_2O_{5+\delta}$ (ref. 239)	375 (600 °C)	—	18.1	LSGM	0.34 (700 °C)	—	0.117 (750 °C)
$GdBaCoCuO_{5+\delta}$ (ref. 171)	90.239 (800 °C)	—	16.3	LSGM	—	—	0.468 (800 °C)
$GdBaCoFeO_{5+\delta}$ (ref. 170)	73.6 (600 °C)	—	18.8	LSGM	—	1.09 (700 °C)	0.450 (800 °C)
$GdBaFeNiO_{5+\delta}$ (ref. 182)	—	—	14.7	SDC	—	0.922 (700 °C)	0.287 (800 °C)
$GdBa_{0.5}Sr_{0.5}Co_2O_{5+\delta}$ (ref. 183)	640 (600 °C)	—	—	GDC	—	0.13 (600 °C)	—
$GdBa_{0.25}Sr_{0.75}CoCuO_{5+\delta}$ (ref. 171)	46.7 (800 °C)	—	16	LSGM	—	0.80 (700 °C)	0.53 (800 °C)
$GdBa_{0.5}Sr_{0.5}CoFeO_{5+\delta}$ (ref. 183 and 184)	—	0.01 (600 °C)	—	GDC	—	0.067 (600 °C)	1.31 (600 °C)
$GdSrCo_2O_{5+\delta}$ (ref. 181)	1155 (600 °C)	—	18.8	LSGM	—	—	0.350 (800 °C)
$Sr_2FeTiO_{6-\delta}$ (ref. 240)	2.83 (600 °C)	—	16.8	SDC	—	0.204 (700 °C)	0.335 (800 °C)
$Ba_2CoMo_{0.5}Nb_{0.5}O_{5+\delta}$ (ref. 241)	1.2 (800 °C)	—	—	SDC	—	0.09 (750 °C)	—

and a consequent disturbance of the O^{2-}–Co^{3+}/Co^{4+}–O^{2-} electronic band overlap.[152] This trend is observed in other studies which report that while the concentration of oxygen vacancies increases with decreasing radius of the lanthanide ions, the total electrical conductivity and the TEC decrease down the series from Ln = La to Ho, and Y.[151,196] In addition to inducing ordering in the crystallographic arrangement of the A and A′ sites, Ba enhances the ionic conductivity of double perovskite oxides because of its large ionic radii. Several studies have reported enhanced electrical conductivity and electrochemical performance with the substitution of Ba^{2+} for Sr^{2+} in layered double perovskite oxides.[177,197] Sr doping on Ba sites increases the oxygen content and thus an increase in the concentration of electronic holes. Table 4 summarises of the most important properties of selected IT-SOFC double perovskite cathodes.[152,156–165,167,169–171,175–180,186,197,220,224,229–241]

A concern with A′-site alkaline earth cations, particularly Sr and Ba, is their preferential segregation towards the cathode surface[198–202] and their chemical instability in CO_2 as they have a high tendency to form carbonates on reaction with atmospheric CO_2.[41–43] The challenge this phenomenon presents is that surface enriched strontium and barium oxides are susceptible to reaction with other gaseous contaminants such as Cr and CO_2 to form secondary phases on the electrode surface which are electronically insulating and impede surface oxygen exchange, consequently hampering the conductivity and electrochemical performance of the cathodes. Segregation originates from the minimization of elastic energy or lattice strain caused by the size mismatch between the dopant and the host cations, driving the smaller or larger sized dopant to free surfaces or interfaces.[203] Composition, temperature, electrochemical polarisation, and oxygen partial pressure have been observed to influence the degree of segregation of Ba and Sr to the surface of the cathode.[201,204–206] To suppress surface segregation, Kwon *et al.*[207] suggest selecting an A-site cation dopant such as Ca which exhibits a small size difference with the host cation. Additionally, they proposed a B-site cation with a small ionic radius such as Co or Ni as they discovered that the B-site ionic size is a major contributor to the segregation energetics. Xia *et al.*[208] reported that co-doping Ca on the Ba and Pr sites in $Pr_{0.9}Ca_{0.1}Ba_{0.8}Ca_{0.2}Co_2O_{5+\delta}$ not only reduced the segregation of Ba to the electrode surface but reduced the material's TEC (18.5×10^{-6} K^{-1}) and improved its electrochemical performance (0.069 Ω cm^2) and maximum power density (712 mW cm^{-2} at 800 °C) as compared with $PrBaCo_2O_{5+\delta}$ with TEC, ASR and maximum power density values of 22.4×10^{-6} K^{-1}, 0.094 Ω cm^2, and 629 mW cm^{-2}, respectively. Chen *et al.*[209] investigated the long-term stability of $PrBa_{0.8}Ca_{0.2}Co_2O_{5+\delta}$ (PBCC) in a Ni–$BaZr_{0.1}Ce_{0.7}Y_{0.1}Yb_{0.1}O_3$ anode supported cell with SDC electrolyte. The cell was run at a cell voltage of 0.7 V at 700 °C with humidified H_2 (~3% H_2O) as fuel and air with ~1% CO_2 as the oxidant. After ~50 h of operation, the PBCC cathode showed stable power output with a degradation rate ~1/24 of that of state-of-the-art LSCF cathode under the same operating conditions, indicating good tolerance to CO_2. Anjum *et al.*[199] observed a substantial reduction in Ba surface segregation in nanostructured $GdBaCo_2O_{5+\delta}$ (GBCO) (~10 nm radius) as well as reduced impedance in comparison with the chemically synthesised bulk sized GBCO electrode. Thus, they proposed applying nano-structuring strategies to control surface cation segregation.

The most studied transition metals for B site substitutions include Co, Fe, Mn, Ni and Cu. Co exhibits a characteristic high catalytic activity making it a B site element choice for many compositions.[165] Furthermore, Co containing samples have demonstrated higher electrical conductivity values than other transition metal compositions. Zhang *et al.* describes the electronic conductivity of cobalt based double perovskite oxides to occur *via* the hopping of electrons along the Co^{4+}–O^2–Co^{3+} bonds within the perovskite structure.[190] The electronic conductivity of perovskite oxides with Co as the only B site ion generally depicts metallic behaviour within the temperature range of 300–900 °C. This phenomenon is explained by the decrease in the concentration of charge carrier accompanied by the loss of lattice oxygen, and the low to high spin transition of Co^{3+} ions with increasing temperature. Fe doping decreases the TEC, improves oxygen diffusivity and catalytic activity, and thermal stability.[169,183,210] However, electrical conductivity decreases with increasing Fe content. For such samples, several factors contribute to the observed reduction in electrical conductivity. Firstly, substituting the slightly larger Fe^{3+} for Co^{3+} alters the orbital configuration of the valence electrons in which the overlap between $(Co,Fe)^{3+/4+}$: 3d and O^{2-}: 2p orbitals decreases resulting in lower electron delocalization and a consequent impediment to electron hopping. Moreover, because a charge compensation of Fe^{3+}–Fe^{4+} preferentially occurs over Co^{3+}–Co^{4+} and a low mobility of Fe ions, the electrical conductivity substantially decreases when Fe doping exceeds its percolation limit. Fe ions have such a lower mobility than Co ions that the reported mobility of electrical holes of $LaFeO_3$ is lower than that of $LaCoO_3$ by approximately three orders of magnitude.[211] Choi *et al.*[168] investigated the synergetic effect of co-doping both A- and B-sites on the electrochemical properties of $PrBaCo_2O_{5+\delta}$. Partially substituting Ba with Sr and Co with Fe in $PrBaCo_2O_{5+\delta}$ created oxygen vacancy (pore) channels in the [PrO] and [CoO] planes that significantly enhanced the oxygen ion diffusion and surface oxygen exchange resulting in a peak power density of ~2.9 W cm^{-2} at 650 °C. Similarly, doping Fe in $PrBa_{0.8}Ca_{0.2}Co_2O_{5+\delta}$ improved the catalytic activity of the cathode with a maximum power density of 1.89 W cm^{-2} at 600 °C.[169] In both compositions, the stronger Fe–O bonding strength increased the mobile oxygen species in the Ln–O layer and thus, improved their catalytic activities. In terms of electrochemical performance, $PrBa_{0.5}Sr_{0.5}Co_{1.5}Fe_{0.5}O_{5+\delta}$ and $PrBa_{0.5}Ca_{0.5}Co_{1.5}Fe_{0.5}O_{5+\delta}$ are very promising materials for IT-SOFC cathodes as they exhibit the highest maximum power density values.

Co containing perovskite oxides undergo chemical expansion with temperature increase, thus their TECs do not match the current IT-SOFC electrolytes. $LnBaCo_2O_{5+\delta}$ perovskites have been reported to possess TEC values in the range of 15–29 $\times 10^{-6}$ K^{-1},[152] while $La_{0.8}Sr_{0.2}Ga_{0.83}Mg_{0.17}O_{3-\delta}$ (LSGM) and $Sm_{0.2}Ce_{0.8}O_{1.95}$ (SDC) have TEC values of 11.4×10^{-6} K^{-1} and 12.4×10^{-6} K^{-1} respectively.[212,213] This large thermal expansion

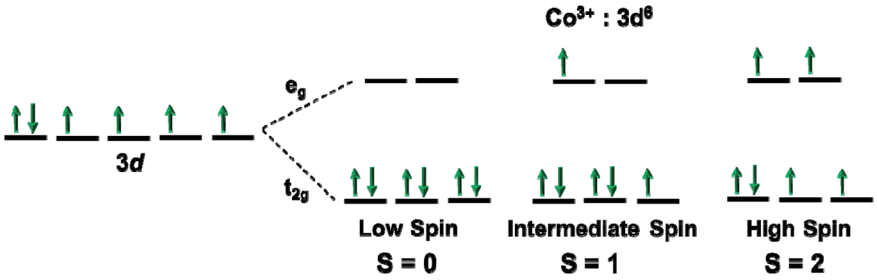

Fig. 5 Electron energy levels of the Low Spin (LS), Intermediate Spin (IS) and High Spin (HS) states of Co^{3+} with $3d^6$ electron configuration.[225]

stems from the reduction of Co^{4+} ions to the larger Co^{3+} ions through the loss of lattice oxygen. Additionally, the spin state transition of Co^{3+} ions from low-spin $Co^{3+}(t_{2g}^6e_g^0)$ (0.54 Å) to the intermediate spin $Co^{3+}(t_{2g}^5e_g^1)$ or high spin $Co^{3+}(t_{2g}^4e_g^2)$ (0.61 Å) state (Fig. 5) with increasing temperature strongly contributes to the TEC mismatch of Co containing cathodes. While several studies have attempted to develop compositions with compatible TECs, it has been observed that doping Sr on the Ba sites increases the TEC of the samples in the high temperature region.[181,214,215] Sr increases the concentration of Co^{3+} which undergoes spin-state transition within the 300–900 °C temperature range, hence an expansion of the lattice. Conversely, doping the A-site with Ca has been reported to improve the TEC of the composition.[208,216,217] Unlike Sr, doping with Ca facilitates the formation of Co^{4+} species which are known to exist in the low-spin state without transitioning to a higher spin state.[208] Also, introducing a small amount of Ln- and/or Ba-deficiency has also been reported to slightly reduce the TEC.[163,218,219] Substituting with other transition metals on the B-site is another strategy to reduce the TECs of cobalt based perovskites. The effect of doping Mn, Fe, Ni, and Cu on the TEC of double perovskites has been investigated in several studies.[170,172,173,176,183,220–222] Substitution of Fe for Co in $LnBaCo_{2-x}Fe_xO_{5+\delta}$ (Ln = Nd and Gd) decreased their TECs from 21.5×10^{-6} and 19.9×10^{-6} K^{-1} to 20.0×10^{-6} and 18.8×10^{-6} K^{-1}, respectively for $x = 1.0$ within the temperature range of 80–900 °C.[170] Thermal expansion in Fe doped perovskites is mitigated by the decrease in the concentration of oxygen vacancies as a result of a stronger Fe–O bond, and the formation of Fe^{3+} in place of the high spin Co^{3+} ions.[183] Cu doped $GdBaCo_2O_{5+\delta}$ and $PrBaCo_2O_{5+\delta}$ decreased from 18.3×10^{-6} and 24.1×10^{-6} K^{-1} to 15.1×10^{-6} and 15.2×10^{-6} K^{-1}, respectively.[223,224] Ni substitution for Co in $LnBaCo_{1.6}Ni_{0.4}O_{5+\delta}$ (Ln = Pr, Nd, and Sm) exhibited a lower TEC than undoped $LnBaCo_2O_{5+\delta}$ (Ln = Pr, Nd, and Sm) by ~4%, 8%, and 13%, respectively within 30–1000 °C.[173] TEC data reported in several studies (Table 4) show that doping Fe on Co sites reduces the TEC by a marginal quantity while Cu or Ni introduction considerably reduces the TEC. Co-doping Fe and Cu in $GdBaCo_{2/3}Fe_{2/3}Ni_{2/3}O_{5+\delta}$ yielded a TEC value of 14.6×10^{-6} K^{-1} in comparison with $GdBaCo_2O_{5+\delta}$ (19.9×10^{-6} K^{-1}).[222]

Another approach to minimize thermal expansion mismatch with electrolytes is incorporating electrolyte powders into the cathode compositions to form composite electrodes. Not only does this method decrease thermal expansion, it increases the triple phase boundary and consequently, active sites for the ORR. For example, SDC, which was introduced in $LnBaCo_2O_{5+\delta}$ in a 25–75 wt% composite, respectively reduced the TEC of the cathode from 21.5×10^{-6}, 21.0×10^{-6}, 19.1×10^{-6}, and 17.6×10^{-6} K^{-1} to 20.1×10^{-6}, 18.5×10^{-6}, 17.2×10^{-6}, and 16.7×10^{-6} K^{-1} for Ln = Pr, Nd, Sm, and Gd, between 30 and 1000 °C, respectively.[226] Some studies have proposed the complete substitution of Co as a strategy to decrease the TEC of cobalt based cathodes. Thus, cobalt-free double perovskite oxides such as $LaBaCuFeO_{5+\delta}$, $SmBaCu_2O_{5+\delta}$, $NdBaFe_{2-x}Mn_xO_{5+\delta}$ and $GdBaFeNiO_{5+\delta}$ have been investigated as potential IT-SOFC cathodes.[182,220,227,228] The TEC of $GdBaFeNiO_{5+\delta}$ was reduced to 14.7×10^{-6} K^{-1} as compared to $GdBaCo_2O_{5+\delta}$ (17.6×10^{-6} K^{-1}).[182] Table 4 shows summary of the most important properties of selected IT-SOFC double perovskite cathodes.[152,156–165,167,169–171,175–180,186,197,220,224,229–241]

Ruddlesden–Popper type oxides as IT-SOFC cathodes

Ruddlesden–Popper (RP) oxides are a family of perovskite related structures with a general formula of $A_{n+1}B_nO_{3n+1}$, alternatively written as $AO(ABO_3)_n$. Often described as a two-dimensional (2D) variation of three-dimensional (3D) perovskite oxides, their crystal structure consists of n perovskite ABO_3 layers stacked between AO rock-salt layers along the c-axis in an alternate arrangement (Fig. 6). The first member of the RP series A_2BO_4 ($n = 1$) exhibits a K_2NiF_4-type tetragonal structure, however, its ideal $I4/mmm$ space group may transform due to a distortion of the BO_6 octahedra around the c-axis.[242] 2D perovskite layers are formed through the corners shared by the BO_6 octahedra, while the AO layers are located between perovskite layers along the c-axis.

Layered K_2NiF_4-type $Ln_2NiO_{4+\delta}$ (Ln = La, Pr, Nd) nickelates and cuprates have garnered interest for exhibiting high oxygen ion diffusivity,[195,243] surface exchange kinetics, sufficient electrical conductivity[244] and moderate thermal expansion coefficients,[245–247] earning them a space amongst promising alternative IT-SOFC cathode materials. For example, Boehm *et al.* demonstrated higher oxygen bulk diffusion ($D^* \sim 4.15 \times 10^{-7}$ cm^2 S^{-1}) and surface exchange coefficient ($k^* \sim 7.57 \times 10^{-6}$ cm S^{-1}) in RP $Ln_2NiO_{4+\delta}$ nickelates than conventional

$La_{0.6}Sr_{0.4}Fe_{0.8}Co_{0.2}O_{3-\delta}$ ($D^* \sim 5.40 \times 10^{-9}$ cm S^{-1}, $k^* \sim 9.26 \times 10^{-8}$ cm S^{-1}) at 700 °C.[248] While ABO_3 oxides are generally oxygen-deficient perovskites, RP oxides can accommodate oxygen interstitial defects in the AO layers,[249] thus, their oxygen content can be hyper-stoichiometric as well as hypo-stoichiometric. These phenomena strongly influence the oxygen transport properties as oxygen ion migration can occur *via* mechanisms related to oxygen vacancies or interstitials.

Like single and double perovskites, cation substitutions influence the ionic and electronic conductivities, surface oxygen catalytic activity, and thermal expansion coefficients amongst other physical properties of RP phases. In addition to doping, the number of perovskite layers within the rock salt layers (AO) (Fig. 6)[250] regulates their physical properties.[251] Generally, the electrical conductivity of RP perovskite oxides ($n = 1$) in air ranges up to a few hundred S cm^{-1}, depending on the temperature.[252,253] Despite the poor electrical conductivity (<100 S cm^{-1}) reported in some ($n = 1$) RP perovskite compositions, good catalytic activities have been observed. $La_{1.5}Pr_{0.5}Ni_{0.95-x}Cu_xAl_{0.05}O_{4+\delta}$ ($x = 0.1$) exhibited a conductivity value of ~30 S cm^{-1} in air due to the reduction of charge carrier concentration, however its ASR and maximum power density were 0.04 Ω cm^2 and 530 mW cm^{-2} at 800 °C, respectively.[253] Its high catalytic activity was ascribed to Cu and Al doping which increased the oxygen vacancies, favouring the adsorption and transport of oxygen ions. Higher order RP ($n = 2$ and 3) MIEC oxides, however, are more electrically conducting and exhibit better electrochemical activities than the ($n = 1$) RP series due to the higher oxygen migration barrier of RP $n = 1$ than $n = 2$ and 3.[251,254,255] An extensive review on RP perovskite cathodes for SOFCs has been published by Ding *et al.*[256]

Other crystal structures for IT-SOFC cathodes

As stated in previous sections, perovskite or perovskite-related oxides containing Co have been widely investigated as candidate cathode materials owing to their high mixed ion–electronic conducting properties. However, their practical application has been hindered due to high TEC values when compared to conventional oxide-ion electrolytes. The resultant thermal expansion mismatch between the cathode and electrolyte becomes a major degradation issue during the thermal cycling of SOFCs as it can lead to delamination and cracks in the cathode layer. The increase in ionic radius due to the low-spin to high-spin transition of Co^{3+} ions (in the octahedral-site) is the cause of abnormally high TECs. Hence, Mn, Fe, Ni, and Cu have been partially substituted at the Co site in order to reduce the TEC values.[4,60,257–260] These substitutions result in compositions that exhibit lower TEC values but the electrochemical

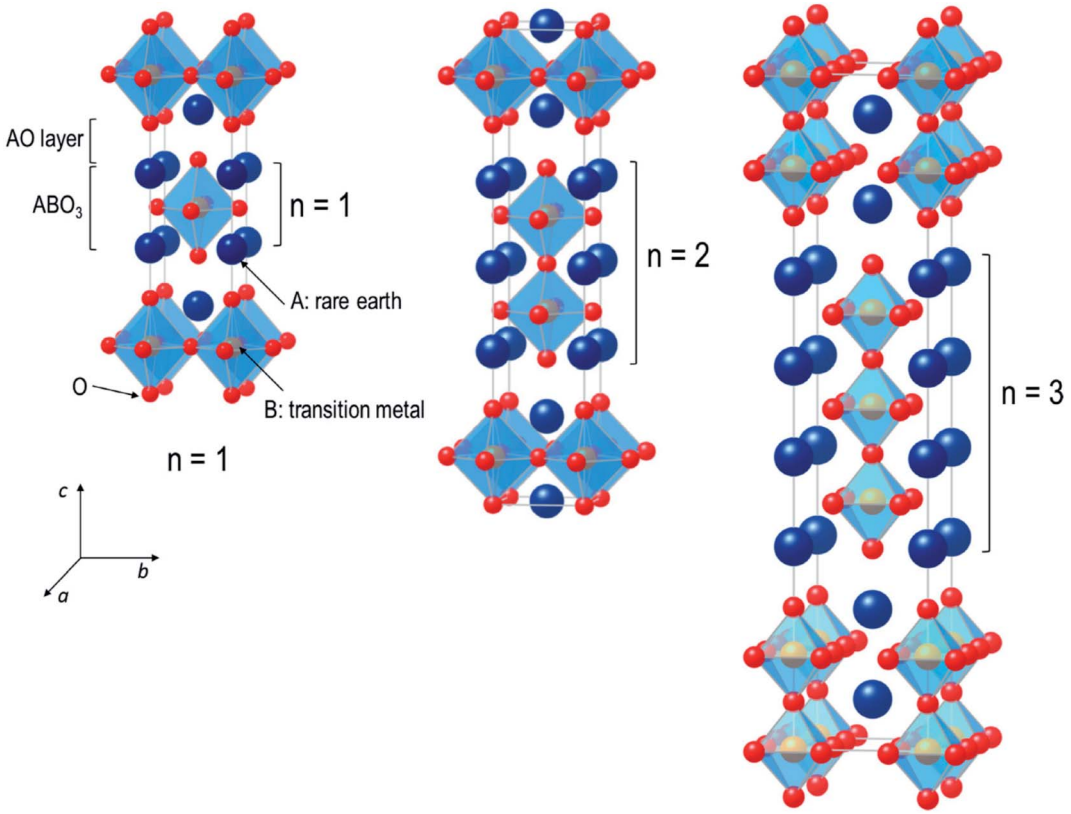

Fig. 6 Schematic crystal structures of $n = 1$, 2 and 3 members of layered structure Ruddlesden–Popper type $A_{n+1}B_nO_{3n+1}$ perovskite oxides. The denotation of n represents the number of stacked perovskite ABO_3 layers separated by a rock salt AO layer.[250]

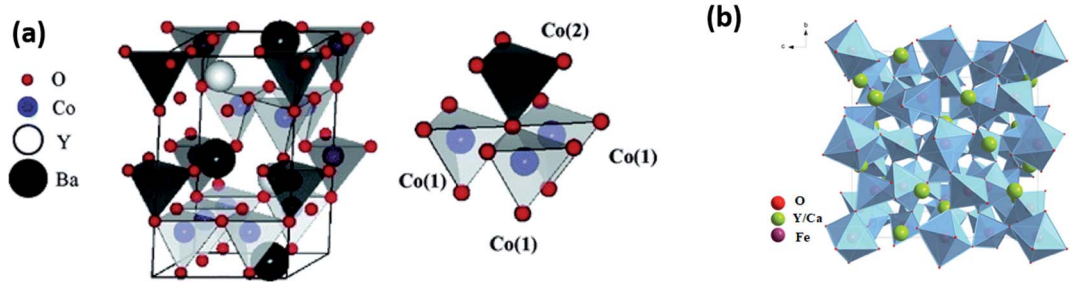

Fig. 7 Schematic illustration of the crystal structure of (a) $YBaCo_4O_7$. Reprinted with permission from ref. 275. Copyright 2006 American Chemical Society. (b) $Y_{3-x}Ca_xFe_5O_{12-\delta}$ ($Ia\bar{3}d$, cubic). Reprinted with permission from ref. 276. Copyright 2020 Elsevier.

performances also decrease when compared to parent Co-based compositions. Hence, researchers have investigated other crystal systems possessing matching TEC values with other cell components.

Swedenborgite-type $RBaCo_{4-x}M_xO_7$ (R = Y, Ca, In, Lu, Yb, Tm, Er, Ho, Dy; M = Co, Zn, Fe, Al, Ga) has shown potential as an oxygen storage material at low temperatures (200–400 °C). However, phase decomposition at elevated temperatures of 700–800 °C has prevented their application as SOFC cathodes.[261–267] Manthiram's group was the first research group that systematically studied the effect of various dopants on the phase stability and electrochemical performance of swedenborgite-type oxides as SOFC cathodes. In the $RBa(Co,M)_4O_7$ structure, Ba^{2+} and R ions adopt 12- and 6-fold oxygen coordination, respectively and the structure consists of corner-shared (Co, M)O_4 tetrahedra (Fig. 7a). Low TEC has been attributed to the presence of tetrahedral-site $Co^{2+/3+}$ ions which do not experience spin-state transitions at elevated temperatures as they are already in the high spin state.[264] The low anisotropic TEC along the *a*-axis is the main contributor to the low bulk TECs as revealed by neutron diffraction studies in $YBaCo_3ZnO_{7+\delta}$, $Y_{0.9}In_{0.1}BaCo_3ZnO_{7+\delta}$, and $Y_{0.9}In_{0.1}BaCo_3Zn_{0.6}Fe_{0.4}O_{7+\delta}$.[268] The change in Co–O bond length

Table 5 High temperature phase stability of selected metal oxides.[269–274a]

	Long-term stability test (120 h)		
Composition	800 °C	700 °C	600 °C
$YBaCo_4O_7$ (ref. 269)	✗ (50 h)	✗ (50 h)	—
$YBaCo_{4-x}Zn_xO_7$; $x = 0$, 0.5,	—	—	—
$1.0 \leq x \leq 2.0$ (ref. 269)	✓	✗	
	✓ (50 h)	✓ (50 h)	
$YBaCo_3ZnO_7$ (ref. 269)	✓ (50 h)	✓ (50 h)	
$YBaCo_3ZnO_7$ (ref. 270)	✓	✗	✗
$Y_{0.75}Ca_{0.25}BaCo_{2.5}Zn_{1.5}O_{7+\delta}$ (ref. 270)	✓	✓	✓
$Y_{0.5}Ca_{0.5}BaCo_{2.25}Zn_{1.75}O_{7+\delta}$ (ref. 270)	✓	✓	✓
$Y_{0.25}Ca_{0.75}BaCo_{2.5}Zn_{1.5}O_{7+\delta}$ (ref. 270)	✓	✓	✗
$CaBaCo_3ZnO_{7+\delta}$ (ref. 270)	✓	✗	✗
$Y_{0.5}In_{0.5}BaCo_3ZnO_{7\pm\delta}$ (ref. 271)	✓	✓	✓
$Y_{0.5}In_{0.5}BaCo_{2.5}ZnO_{7\pm\delta}$ (ref. 271)	✓	✓	✓
$Y_{0.5}In_{0.5}BaCo_2Zn_2O_{7\pm\delta}$ (ref. 271)	✓	✓	✓
$InBaCo_3ZnO_{7\pm\delta}$ (ref. 271)	✗	✗	✓
$YBaCo_{3.2}Ga_{0.8}O_{7+\delta}$ (ref. 272)	✓	✓	✓
$YBaCo_{3.3}Ga_{0.7}O_{7+\delta}$ (ref. 272)	✓	✗	✗
$InBaCo_{3.3}Ga_{0.7}O_{7+\delta}$ (ref. 272)	✗	✗	✗
$CaBaCo_{3.3}Ga_{0.7}O_{7+\delta}$ (ref. 272)	✗	✗	✗
$Y_{0.9}In_{0.1}BaCo_{3.3}Ga_{0.7}O_{7+\delta}$ (ref. 272)	✓	✓	✓
$Y_{0.5}In_{0.5}BaCo_{3.5}Ga_{0.5}O_{7+\delta}$ (ref. 272)	✓	✓	✓
$Y_{0.7}In_{0.3}BaCo_{3.3}Ga_{0.7}O_{7+\delta}$ (ref. 272)	✗	✗	✗
$In_{0.7}Ca_{0.3}BaCo_{3.3}Ga_{0.7}O_{7+\delta}$ (ref. 272)	✗	✗	✗
$YBaCo_{4-x}Al_xO_{7+\delta}$ (ref. 273)	✗	✗	✗
$Y_{0.75}Tb_{0.25}BaCo_{3.2}Ga_{0.8}O_{7+\delta}$ (ref. 274)	✓	✓	✓

[a] ✗ = not stable, ✓ = stable.

in CoO_4 polyhedra was suppressed by doping with In, Zn, and Fe which resulted in a reduction in the anisotropic and bulk TECs.[268]

The phase stabilities of $RBaCo_{4-x}M_xO_7$ series were assessed by long-term phase stability measurement by heating the samples at 600, 700, 800, and 900 °C for 50–120 h, and high-temperature X-ray diffraction (XRD) measurements. From Table 5, it can be seen that Zn substitution increased the phase stability at high temperatures for $RBa(Co,M)_4O_7$ (R = Y, Ca, In; M = Zn, Fe, Al).[269] By looking into the decomposition products ($BaCoO_{3-\delta}$ and Co_3O_4) of the $YBaCo_4O_7$ sample, it was suggested that at elevated temperatures cobalt prefers to adopt octahedral coordination instead of tetrahedral coordination. In both $BaCoO_{3-\delta}$ and Co_3O_4 decomposition products, Co is in the octahedral coordination. As Zn^{2+} prefers the tetrahedral-site, the partial substitution of Zn^{2+} for $Co^{2+/3+}$ stabilised the $YBaCo_{4-x}Zn_xO_7$ ($x \geq 1$) phase with corner-shared CoO_4 tetrahedra.[269] Similar to $RBaCo_{4-x}M_xO_7$, the high temperature phase stability of the $Y_{1-x}Ca_xBaCo_{4-y}Zn_yO_7$ system improved with increasing Zn content, while Ca contents ≥0.5 deteriorated the phase stability.[270] Similar tests were also performed on the $Y_{0.5}In_{0.5}BaCo_{4-x}Zn_xO_7$ ($x = 1$, 1.5, and 2) series.[271] Here, it was seen that employing a mixture of Y and In (50% each) promotes phase stability and overcomes the phase-decomposition problems due to the increased oxygen content and decreased lattice size.[271]

In the Ga doped-$YBaCo_{4-y}Ga_yO_{7+\delta}$ (y = 0.6–0.8) series, $YBaCo_{3.2}Ga_{0.8}O_{7+\delta}$ exhibited good stability in long-term studies suggesting the positive effect of Ga doping to reduce the temperature range of decomposition and improving the phase stability at 800 °C.[272] On the other hand, serious decomposition of $InBaCo_{3.3}Ga_{0.7}O_{7+\delta}$ into Co_3O_4, In_2O_3 and CaBa–$Co_{3.3}Ga_{0.7}O_{7+\delta}$ indicated again that the instability of Co^{3+} in the tetrahedral sites and its preference for octahedral coordination is the cause of phase instability.[272] The Y-doped $Y_{1-x}In_xBaCo_{3.3}Ga_{0.7}O_{7+\delta}$ (x = 0.1–0.9) series also remains stable at high temperatures indicating that the synergistic effect of In and Y could also maximize the stability at a certain Ga content.[272] However, $Y_{1-x}Ca_x$-$BaCo_{3.3}Ga_{0.7}O_{7+\delta}$ and $In_{1-x}Ca_xBaCo_{3.3}Ga_{0.7}O_{7+\delta}$ samples were not stable long-term, suggesting that there is no synergistic effect of In and Ca codopants.[272] In recent studies, doping and co-doping effects of trivalent cations (Al^{3+}, Ga^{3+}, and Fe^{3+}) on the phase stability and electrochemical performance for the ORR have been reported.[273] It was seen that Al based compositions, $YBaCo_{4-x}$-$Al_xO_{7+\delta}$ showed severe decomposition above 700 °C.[273] Among the trivalent dopants in the YBa(Co, Ga, Al, and Fe)$_4O_{7+\delta}$ series, the order of dopants towards the phase stabilization capability can be summarized as $Ga^{3+} > Al^{3+} > Fe^{3+}$.[273] Additional studies with the Tb doping showed that Tb has a relatively weaker stabilization capability compared to Y.[274]

However, owing to low oxygen permeation flux majority of the studies for the ORR were performed with GDC composites. For example, the non-composite $YBaCo_3ZnO_7$ cathode showed an ASR of 0.15 Ω cm^2 at 700 °C, whereas the $YBaCo_3ZnO_7$ + GDC composite cathode showed a lower ASR of 0.06 Ω cm^2 at 700 °C.[269] Studies on various $YBaCo_3ZnO_7$ + GDC composite cathodes with various GDC contents showed that 50 : 50 wt% showed the lowest ASR values indicating that incorporation of GDC offers an extended TPB and oxide-ion bulk diffusion and thereby enhances the catalytic activity for the ORR.[277] All the studies showed almost similar ASR values at 700 °C for composite cathodes (0.06–0.08 Ω cm^2).[269,274] Stability against CO_2 was also investigated for (Y,Tb)$Ba(Co,Ga)_4O_{7+\delta}$ swedenborgite oxides,[277] where it was seen that the ASRs of (Y,Tb)$Ba(Co,Ga)_4O_{7+\delta}$–Gd-doped CeO_2 (GDC) composite cathodes only increased by ∼120% at 600 °C when exposed to 5% CO_2 in air,[277] whereas literature studies have shown that the ASR of Co-containing perovskite oxides increases >500% when exposed to 5% CO_2 in air.[277] The better CO_2 tolerance was attributed to the presence of low number of oxygen vacancies in (Y,Tb)$Ba(Co,Ga)_4O_{7+\delta}$.[277]

Yttrium iron garnet, $Y_3Fe_5O_{12}$ (YIG) finds applications in ferrimagnetic oxide, microwave and magneto-optic devices.[278–280] Doping Y with Ca^{2+} increases specific oxygen permeability (10^{-11} mol s^{-1} cm^{-2}).[281] The other advantage associated with YIG is low TEC values (10.6×10^{-6} K^{-1}).[282] Given these advantages few studies have employed doped garnets as SOFC cathodes. Zhong *et al.* showed that the $Y_{2.5}$-$Ca_{0.5}Fe_5O_{12-\delta}$ (YCFO)–$Ce_{0.8}Sm_{0.2}O_{1.9}$ (SDC, 40 wt%) composite electrode cathode showed an ASR of 0.55 Ω cm^2 at 650 °C,[282] where oxygen ion diffusion, oxygen dissociative adsorption, and gas-phase diffusion were assigned as rate-limiting steps based on equivalent circuit modeling.[282] The maximum power density (MPD) of 438 mW cm^{-2} with SDC electrolyte (40 μm) was seen at 650 °C.[282]

A recent study by Zhang *et al.* reported the systematic effect of Ca-doping on the electrical and electrochemical properties of $Y_{3-x}Ca_xFe_5O_{12-\delta}$ (x = 0, 0.05, 0.1, 0.3, 0.5 and 0.7), where the x = 0.3 member exhibited the highest oxygen non-stoichiometry (δ = 0.19) and X-ray absorption spectroscopy (XAS) studies confirmed the formation of hole carriers ($Fe^{\bullet}_{Fe}$) as a result of Ca doping. With an increase in Ca amount until $x = 0.1$, the electrical conductivity (1.58 S cm^{-1} at 750 °C) increased and then decreased due to a decrease in the concentration of the charge carriers. The lowest ASR of 1 Ω cm^2 was seen for $x = 0.3$ garnet–LSGM composite electrode at 750 °C in air. pO_2 dependent ASR and impedance spectroscopy genetic programming (ISGP) analysis showed that oxygen dissociation and partial reduction of adsorbed oxygen molecule are the rate limiting steps for the ORR.[276]

Composite cathodes

Juhl *et al.* were one of the first researchers who correlated the performance and structure of composite SOFC cathodes.[283] At an overvoltage of −50 mV an ASR of 0.5 Ω cm^2 at 850 °C was obtained for the LSM–YSZ composite cathode.[283] With increase in the thickness of the composite cathode layer, the polarisation resistance decreased more prominently at 700 °C, indicating that the bulk of the LSM–YSZ (60 : 40) composite layer is active for the ORR.[283] A uniform mixture of the LSM, YSZ, and pores was recognized as the key for considerable improvement of the composite layer which can lead to easy percolation of electrons,

oxide ions and gas through the layer and hence extending the active TPB area.[283]

Leng *et al.* employed the LSCF–GDC (50–50 wt%) composite cathode with a power density of 625 mW cm^{-2} at 600 °C.[284] The effect of sintering temperature showed that the best performance at 600 °C was achieved for a sintering temperature of 975 °C.[285] A high sintering temperature of 1100 °C resulted in a large area of dense regions with less micropores which significantly reduced the reaction area and increased the resistance of oxygen species diffusion along the surface of grains.[285] On the other hand, the lower temperature sintered cathode was more porous, with a lot of macro- and micro-pores, which led to an increase in reaction area. However, reducing the temperature to 850 °C weakened the connection between agglomerated particles. This increased the resistance of bulk/surface diffusion of oxygen species including oxygen ion as well as electron transfer through the porous cathode.[285]

Chen *et al.* prepared a novel Pr_2NiO_4 (PNO)–$Pr_{0.2}Ce_{0.8}O_{1.9}$ (PCO) composite cathode through solid-state mixing and a modified sol–gel method,[286] where the PNO–PCO composite cathode obtained by the sol–gel method exhibited better electrochemical performance due to uniform particle size distribution and porosity with GDC electrolyte (ASR = 0.09 Ω cm^2 at 800 °C), and the NiO–GDC/GDC/PNO–PCO single cell yielded an MPD of 0.57 W cm^{-2} at 800 °C.[286] Co-doped double perovskite-type cobaltite $Pr_{0.9}Y_{0.1}BaCo_{1.8}Ni_{0.2}O_{6-\delta}$ (PYBCN)–SDC (PYBCN–SDC) composite exhibited an ASR value of 0.045 Ω cm^2 at 800 °C where the lower ASR was attributed predominantly to a large concentration of O^{2-} vacancies in the cobaltite component of the composite.[287] Jafari *et al.* showed an ASR at 0.008 Ω cm^2 (750 °C) for the $La_{0.6}Ca_{0.4}Fe_{0.8}Ni_{0.2}O_{3-\delta}$–YSZ (LCFN–YSZ) composite.[288]

Zhao *et al.* prepared composite-cathode LSCF–GDC using the nanoparticle of GDC impregnated to the LSCF and obtained the lowest resistance of 0.07 Ω cm^2 at 600 °C.[289] Liu *et al.* performed long term studies on the LSCF–GDC composite cathode and showed that ASR increased from 0.38 Ω cm^2 to 0.83 Ω cm^2 after testing at 750 °C for 500 h. It was also shown that the degradation rate of the LSCF conventional cathode was higher when compared with composite-cathode LSCF–SDC.[290] Xi *et al.* impregnated $Sm_{0.5}Sr_{0.5}CoO_{3-\delta}$ (SSC) into $PrBaCo_2O_{5+\delta}$ (PBC) and obtained an ASR of 0.16 Ω cm^2 and power density of 385 mW cm^{-2} at 700 °C.[291] The infiltrated LCFN–SDC (70 : 30) composite cathode showed an ASR of 0.15 Ω cm^2 at 800 °C where the improvement was attributed to enhanced activity for surface oxygen dissociation and diffusion processes achieved due to the specific electrode architecture by the nano SDC decorated on the LCFN backbone.[292] A single perovskite oxide $Sm_{0.5}Sr_{0.5}CoO_{3-\delta}$ (SSC) with high ORR activity was combined with MIEC $SmBaCo_2O_{5+\delta}$ (SBC) to exhibit an ASR of 0.021 Ω cm^2 at 750 °C.[293]

In the field of proton conducting SOFC cathodes, composite cathode materials are mainly divided into proton-blocking composite cathodes (PBCCs) and proton-conducting composite cathodes (PCCCs).[294] In PBCC, electrochemical reactions are mainly restricted at the cathode–electrolyte interface, as dissociated oxygen ions are transferred along the surface of the

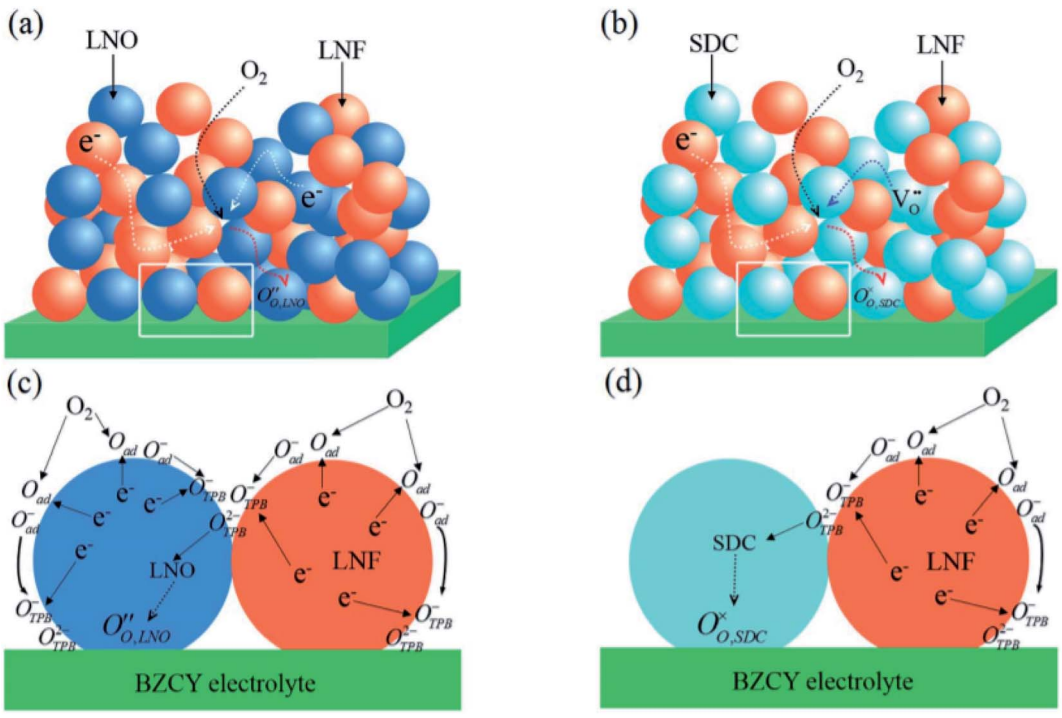

Fig. 8 Schematic diagrams of the overall ORR at (a) the LNO–LNF cathode (b) SDC–LNF cathode with BZCY electrolyte, and an ORR model at the cathode (c) LNO–LNF/electrolyte (BZCY) interface and (d) SDC–LNF/electrolyte (BZCY) interface. Reproduced from ref. 294 with permission from the Royal Society of Chemistry.

cathode or through the bulk of the cathode to TPBs. Whereas in PCCCs, transport of all three charge carriers (oxygen vacancies, electronic defects and protons) occurs simultaneously resulting in enhanced active area for electrochemical reactions.[294] Simply, it is expected that PCCCs should exhibit better electrochemical performance than the PBCCs owing to the presence of more TPBs. However, some experiments show the opposite trend. As water is generated at the cathode side, the PCCC will adsorb more water and hence there will be a reduction in active TPBs for the ORR; on the other hand, PBCC will show better performance even though it has less TPBs.

When comparing two types of PBCC with $BaZr_{0.1}Ce_{0.7}Y_{0.2}O_{3-\delta}$ (BZCY) electrolyte, $La_2NiO_{4+\delta}$–$LaNi_{0.6}Fe_{0.4}O_{3-\delta}$ (LNO–LNF) showed a lower ASR of 0.103 Ω cm^2 with an MPD of 490 mW cm^{-2} at 700 °C than $Sm_{0.2}Ce_{0.8}O_{2-\delta}$–$LaNi_{0.6}Fe_{0.4}O_{3-\delta}$ (SDC–LNF).[294] Additionally, introducing an anode functional layer (AFL) between the anode and electrolyte increased the power outputs to 708 mW cm^{-2}, at 700 °C for the LNO–LNF cathode. The LNO–LNF cathode exhibited better performance than SDC–LNF due to its oxygen transport mechanism which occurs through interstitial oxygen defects (Fig. 8).[294] Chen *et al.* generalised the percolation theory for typical H^+–SOFC composite cathodes with e^-, O^{2-} and H^+ mixed conducting properties based on the (LSCF–SDC–BZCY) composite cathode.[295] Duan *et al.* employed a proton-, oxygen-ion-, and electron–hole-conducting $BaCo_{0.4}Fe_{0.4}Zr_{0.1}Y_{0.1}O_{3-\delta}$ as a composite cathode and obtained a high power density of 455 W cm^{-2} for 40 wt% BCZYYb + 60 wt% NiO|BCZYYb +1.0 wt% NiO|BCZY63 + BCFZY0.1, and 405 W cm^{-2} for 40 wt% BCZYYb + 60 wt% NiO|BCZYYb +1.0 wt% NiO|BCZY63 + BCFZY0.1 cell at 500 °C.[296] Dai *et al.* employed a one step co-firing process to prepare SSC–BZY and SSC–$BaCe_{0.7}Zr_{0.1}Y_{0.2}O_{3-\delta}$ (BCZY) composite-cathode,[297] where SSC–BZY showed an ASR of 0.3 Ω cm^2 and SSC–BZCY showed an ASR of 0.58 Ω cm^2 at 650 °C.[297] The lower ASR of SSC–BZY was attributed to the highly porous microstructure, which increased the rate of gas diffusion at the cathode.

Mechanism of the oxygen reduction reaction (ORR)

The overall ORR can be generally expressed by an overall equation as shown in Table 6 [283,285,298–301] and Fig. 9. The ORR consists of multielementary reactions such as adsorption of oxygen molecule onto the surface, dissociation of the oxygen molecule and diffusion of the adsorbed species, subsequent reduction of adsorbed oxygen species and incorporation into the cathode/electrolyte lattice.[298] The rates of these reactions determine the cathode's ultimate electrochemical performance. To understand the reason behind the different electrochemical behaviours of various compositions, understanding the rate determining step (RDS) of the ORR is very important.

Based on the conducting mechanism and the pathways for the ORR, cathode materials can be categorized into two groups: (i) pure electronic conducting materials, and (ii) mixed ionic-electronic conductors (MIECs).[6,8,119,302,303] In the first group, after the oxygen molecule has been adsorbed and dissociates on the perovskite surface, it migrates to the TPBs through surface diffusion where oxide ions form and incorporate into the electrolyte by electron transfer. Fig. 10a schematically shows the oxygen pathway in a pure electronic conductive catalyst. The length of TPBs plays an important role in controlling the catalytic activity of the electrode. In this case, a porous electrode is required to provide more TPB sites for the ORR.[6,8,302–304] The second group consists of materials showing both electronic and ionic conductivity towards the ORR. As a result, the adsorbed oxygen can be transferred to the electrolyte *via* both surface and bulk diffusion not limited to the TPBs as illustrated in Fig. 10b. MIECs are particularly attractive for application in IT-SOFCs where catalytic activity is required in the lower temperature range.[305]

Each elementary step of the overall ORR occurring at the MIEC cathodes has a specific relationship with the pO_2 as shown in Table 6.[283,285,298–301] For example, the double perovskite type $Y_{1-x}Ca_xBaCo_2O_{5+\delta}$ (YCBC)/LSGM/YCBC symmetrical cell

Table 6 pO_2 dependency of ASR revealing the process associated with different reactions involved in the ORR[283,285,298–301]

Process	n	Equation
Overall	$ASR = ASR_o(pO_2)^{-n}$	$O_2(g) + 4e' + 2V_O^{\cdot\cdot} \rightleftharpoons 2O_O^{\times}$
Adsorption of oxygen molecules[298,299]	1	$O_{2(g)} \leftrightarrows O_{2,ads}$
Transfer of electrons[299]	0.39	
Ionization of atomic oxygen and CT reaction at TPB[300]	0.28–0.36	
Charge-transfer at TBP[301]	0.24 to 0.32	
Oxygen surface diffusion of dissociative adsorbed oxygen at the TPB $(La_{0.75}Sr_{0.25})_{0.9}MnO_3$–8YSZ (50 : 50)[283]	0.5	$O_{2,ads(g)} \leftrightarrows 2O_{ads}$
Oxygen surface diffusion of dissociative adsorbed oxygen at the TPB $(La_{0.75}Sr_{0.25})_{0.9}MnO_3$–8YSZ (50 : 50)[283]		
Charge transfer reaction[285]	0.25	$O_{ads} + 2e' + V_O^{\cdot\cdot} \leftrightarrows O_O^{\times}$
O^{2-} transfer from the TPB to the electrolyte[285]	0	$O_{TPB}^{2-} + V_O^{\cdot\cdot} \leftrightarrow O_O^{\times}$

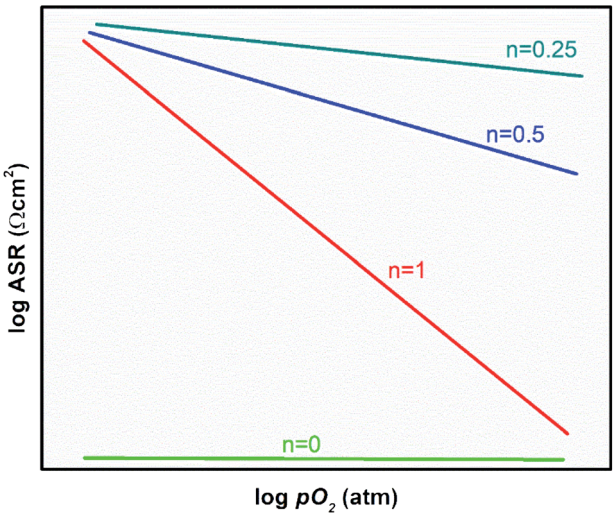

Fig. 9 Schematic representation of the variation of ASRs as a function of pO_2.

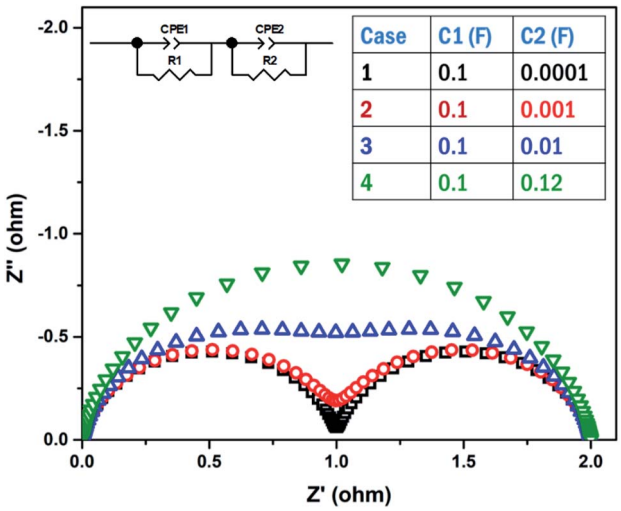

Fig. 11 Nyquist plot showing the semicircle deconvolution of simulated data with different relaxation times (RC).

showed a dependence value of 0.5 at temperatures 700 °C to 800 °C, indicating that dissociation of molecular oxygen into atomic oxygen is the RDS at these temperatures.[216] The pO_2 dependence of ASR for LSM-i-ESB (LSM-infiltrated ESB $(Bi_{0.8}Er_{0.2})_2O_3$) at 650 °C shows a dependence value of 0.1 for ASR_{HF}, and dependence of 0.7 for ASR_{LF}.[306] This indicates that ASR_{LF} is related to surface chemical reactions, whereas ASR_{HF} is related to oxygen ion transport between solid phases. In the case of $Nd_{0.75}Sr_{0.25}Co_{0.8}Fe_{0.2}O_{3-\delta}$ (NSCF) + LSGM symmetrical cells at low pO_2 range (<0.1 atm), ASR_{HF} showed dependence of 1, and ASR_{LF} showed dependence of 0.24 at 700 °C. At high pO_2 range (>0.1 atm), ASR_{HF} showed dependence of 0.58; ASR_{LF} showed dependence of 0 at 700 °C,[307] indicating that in the low pO_2 range, the charge-transfer reaction dominates the ORR, whereas surface diffusion (of dissociative adsorbed oxygen) dominates the ORR in the higher pO_2 region.

Distribution of relaxation times

From a mechanistic point of view, the ORR involves various subprocess where ASR values are affected by both fundamental material properties (ionic and electronic conductivity, oxygen surface exchange and bulk diffusion rates) and synthesis parameters (particle size, surface morphology of the grains, porosity, tortuosity, and the interface between the electrode and electrolyte). Conventionally, the impedance data are analysed through equivalent circuit modelling (ECM), where a viable equivalent circuit (EC) is fitted to the measurement dataset.[308–310] In ECM, known electrical analogues, such as resistance, capacitance and inductance are used to build the EC, along with more complex functions like semi-infinite and bounded diffusion (Warburg type) elements, and Gerischer element (GE).[308,311] However, deconvolution of AC impedance data becomes difficult when processes with similar relaxation times are present, especially in the case of the ORR which involves several elementary reactions (Fig. 11).

Alternatively, the impedance data can be transformed into a distribution function of relaxation times (DFRT).[312–323] DFRT shows data as peaks on a log(τ) axis and each peak corresponds to specific electrochemical process. DFRT does not involve preconceived notions and is hence model free. By looking into the trends of peak position and height as a function of temperature, partial pressure and/or polarization, information on the electrochemical processes can be easily deducted and visualised. The DFRT, $G(\tau)$, can be obtained by solving the following expression:

$$Z(\omega) = R_\infty + R_{pol}\int_{-\infty}^{\infty} \frac{\Gamma(\log(\tau))}{1+i\omega\tau} d(\log(\tau)) \quad (2)$$

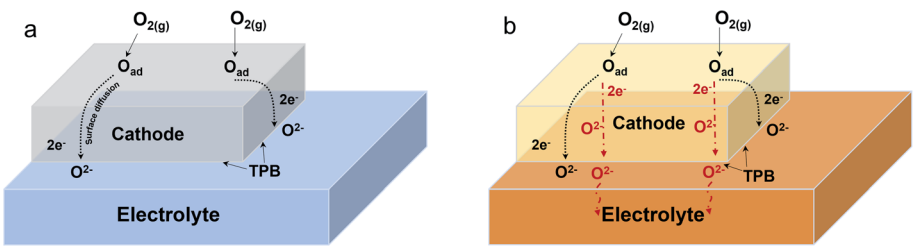

Fig. 10 Schematic of the possible pathways for the oxygen reduction reaction (ORR) in (a) pure electronic conductor and (b) mixed-ionic electronic conductor (MIEC).

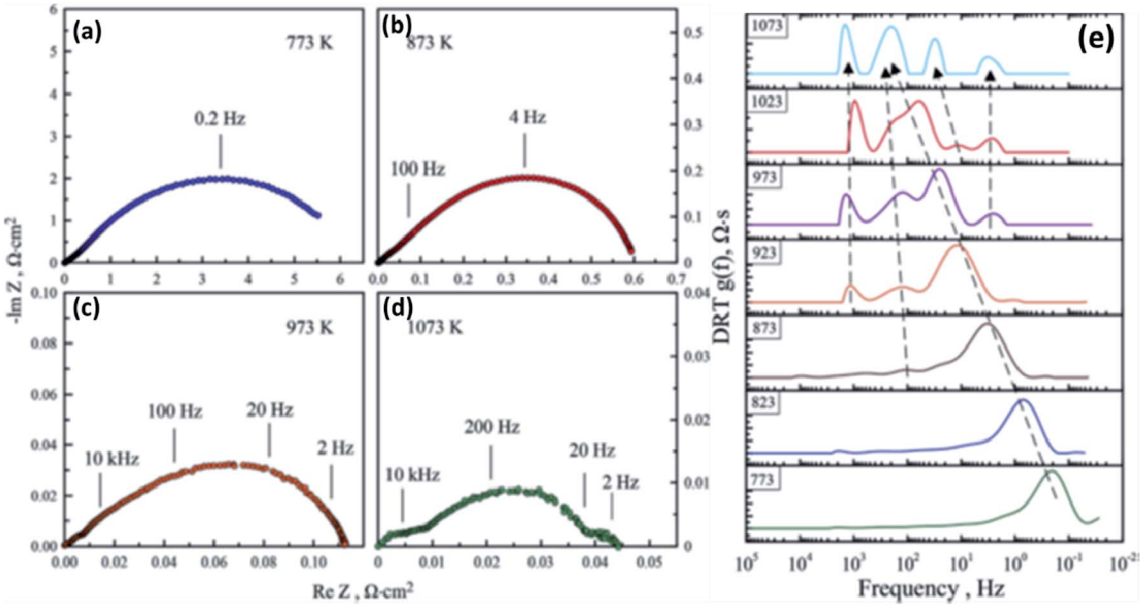

Fig. 12 (a–d) Electrochemical impedance spectra, (e) DRT plots at different temperatures for the symmetrical cell with PYBCN–SDC (70–30 wt%) composite electrodes at different temperatures in the air. Reprinted from ref. 287. Copyright 2019, with permission from Elsevier.

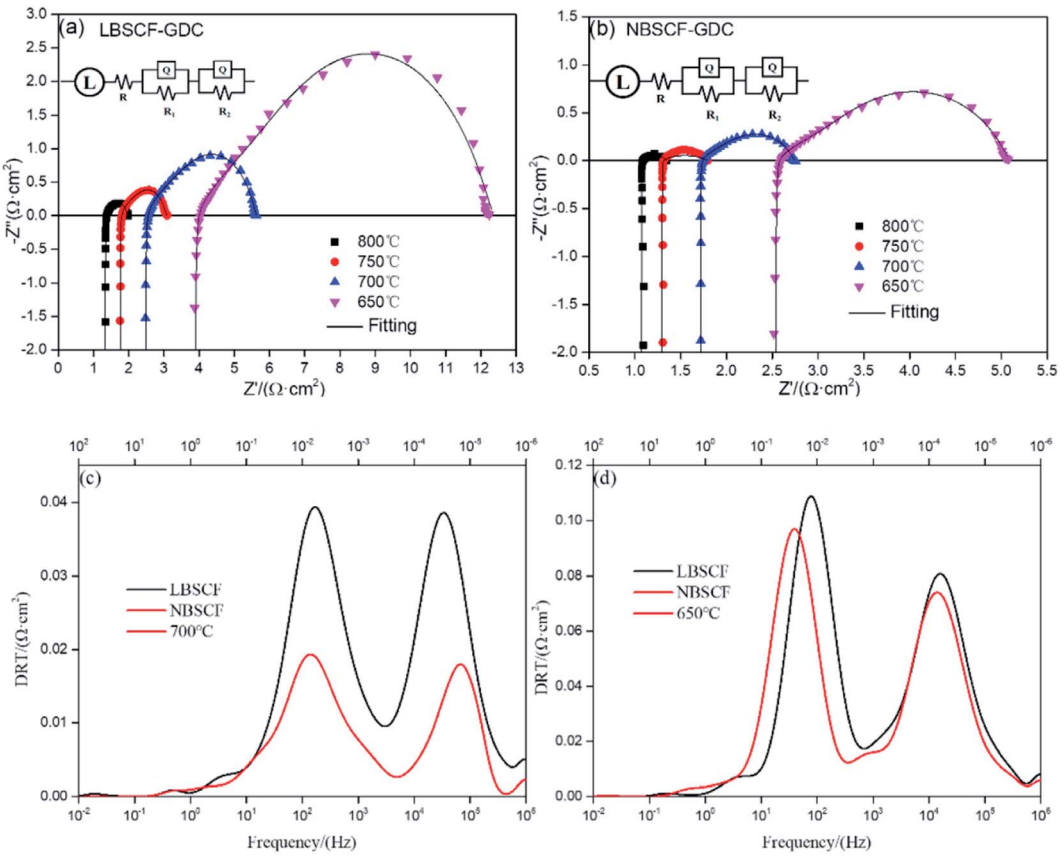

Fig. 13 Electrochemical impedance spectra of (a) LBSCF and (b) NBSCF symmetrical cells under OCV conditions at different temperatures in air. DRT analysis of ASRs for LBSCF and NBSCF cathodes at (c) 700 °C and (d) 650 °C. Reprinted from ref. 324. Copyright 2021, with permission from Elsevier.

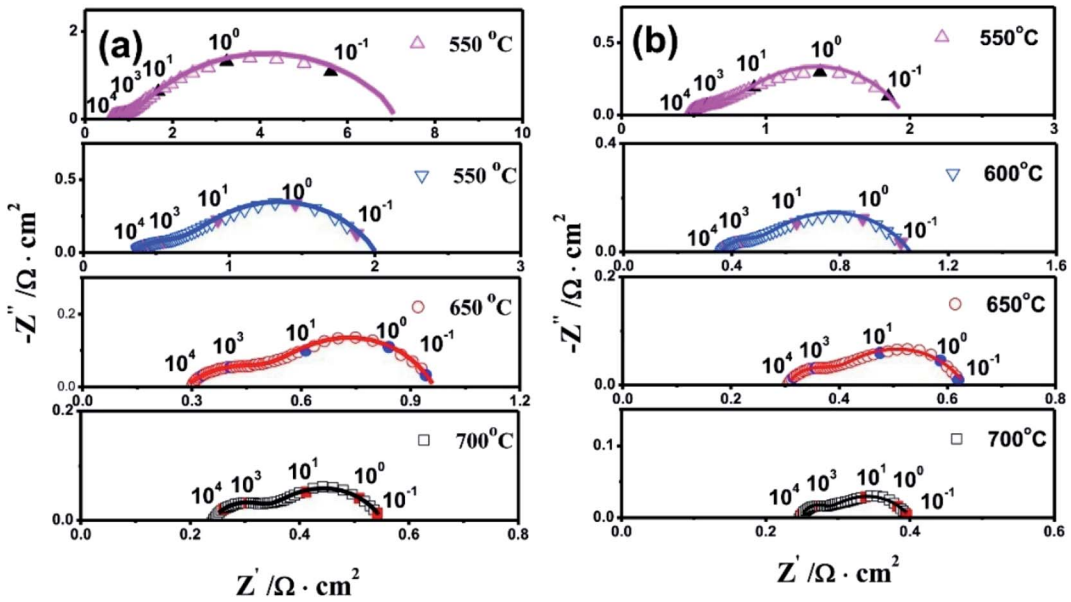

Fig. 14 The fitted impedance spectra of the cells under OCV conditions with (a) B9CFZY and (b) B9CFZY–BZCY cathodes. Reprinted with permission from ref. 325. Copyright 2019, with permission from Elsevier.

where $Z(\omega)$ is the dataset, R_∞ is the high frequency cut-off resistance, and R_{pol} is the polarization resistance or overall resistance of the dispersion. The time constant, τ, is the inverse of the frequency: $\tau = (2\pi f)^{-1} = \omega^{-1}$.

Marshenya *et al.* studied the impedance data under OCV conditions for $Pr_{0.9}Y_{0.1}BaCo_{1.8}Ni_{0.2}O_{6-\delta}$–$Ce_{0.8}Sm_{0.2}O_{1.9}$ (PYBCN–SDC) composite cathode through DRT (Fig. 12).[287] The DRT plot clearly showed that at lower temperature the ORR is dominated by a single electrochemical process and with increase in temperature, four different additional processes appear (Fig. 12e). The additional peaks at high temperatures were attributed to the presence of impurity phases seen in high temperature mixtures of PYBCN–SDC powders. Although electrochemical processes responsible for each peak were not

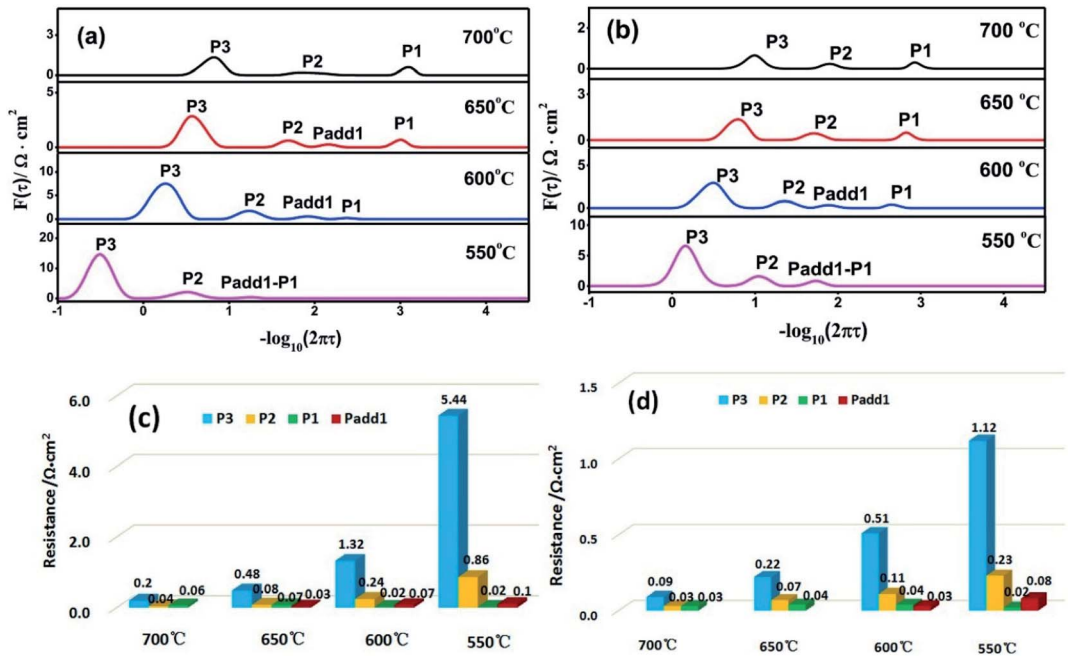

Fig. 15 DRT analysis of the impedance spectrum data under OCV conditions for the anode supported cells with (a) B9CFZY and (b) B9CFZY–BZCY cathodes, and the values of polarization resistance corresponding to the different peaks for the anode supported cells with (c) B9CFZY and (d) B9CFZY–BZCY cathodes. Reprinted with permission from ref. 325. Copyright 2019, with permission from Elsevier.

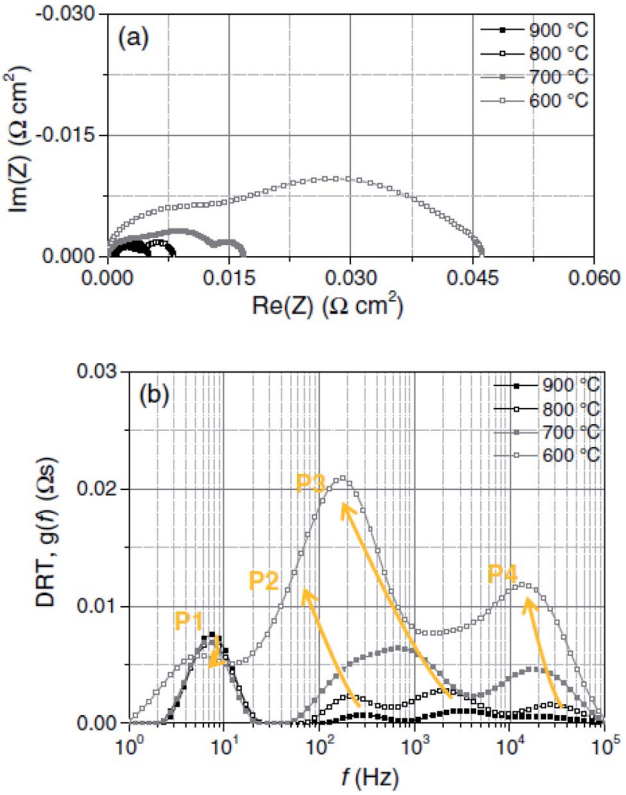

Fig. 16 Electrochemical impedance plots for the BSCF/GDC/BSCF symmetrical cell under OCV conditions with *in situ* sintered electrodes from 900 to 600 °C at a constant pO_2 of 0.21 atm: (a) impedance spectra (ohmic losses were subtracted for clarity reasons) and (b) corresponding DRTs. Reprinted with permission from ref. 328. Copyright 2017, with permission from The Electrochemical Society.

explained, it was suggested that the impurity peaks might have affected the electrochemical parameters of oxygen exchange between the cathode and ambient atmosphere.

Fig. 13a and b show the impedance plots under OCV conditions and Fig. 13c and d show the DRT plots for symmetrical cells of $LaBa_{0.5}Sr_{0.5}Co_{1.5}Fe_{0.5}O_{5-\delta}$ (LBSCF)–GDC and $NdBa_{0.5}Sr_{0.5}Co_{1.5}Fe_{0.5}O_{5-\delta}$ (NBSCF)–GDC composite cathodes at different temperatures in air.[324] The authors first fitted the impedance plot with ECM and then employed DRT to deconvolute data to further understand individual electrochemical processes. The authors assigned oxygen ion charge transfer from the electrolyte to the cathode at TPB to high frequency (>10^3 Hz) peaks, surface exchange or ion transfer at the cathode to IF (1–10^3 Hz) peaks, and the gas diffusion process was attributed to LF (10^2–1 Hz) peaks. By analysing the DRT plots, the authors argued that since the integral areas for HF and IF peaks of NBSCF were smaller than those of LBSCF (Fig. 13c and d), NBSCF possessed higher oxygen surface exchange and diffusion ability. Although not clearly seen, the authors mentioned that since LBSCF DRT peaks showed slightly larger temperature dependence, LF peaks attributed to the oxygen diffusion process were termed RDS. It is important to mention that individual peaks were assigned to different electrochemical processes by referencing literature studies.

Wei *et al.*[325] employed DRT to distinguish the contributions of different polarization processes of anode-supported button cells with $Ba_{0.9}Co_{0.4}Fe_{0.4}Zr_{0.1}Y_{0.1}O_{3-\delta}$ (B9CFZY) and B9CFZY–$BaZr_{0.1}Ce_{0.7}Y_{0.2}O_{3-\delta}$ (BZCY) cathodes. Fig. 14 shows the fitted impedance data of anode supported cells under OCV conditions with B9CFZY and B9CFZY–BZCY cathodes, although ECM used for fitting the experimental data was not specified. Fig. 15 shows the DRT plot at 700–550 °C, where at lower temperature four peaks were seen, and at 700 °C three peaks were seen. The peaks were labelled as P1, $P1_{add}$, P2, and P3. Comparing the DRT plots in Fig. 14a and b, it can be seen that P1 peaks were similar in both cases and were assigned to hydrogen charge transfer in the anode. P2 and P3 were assigned to oxide ion diffusion to TPBs or active sites in the cathode, and oxygen gas adsorption/dissociation, while referencing literature studies. In the B9CFZY–BZCY cell, P2 and P3 were smaller than the corresponding peaks for the cell with the B9CFZY cathode, indicating the positive effect of adding BZCY to the B9CFZY cathode which boosts oxygen gas adsorption, dissociation and transfer. As P3 was the major contributor to polarization resistance, the RDS was assigned to oxygen species involved in the reaction. P1 seen

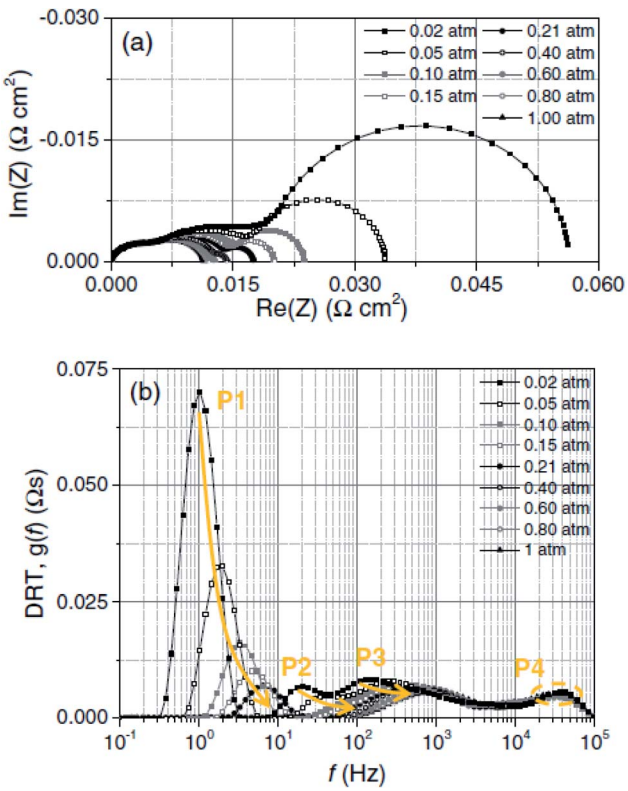

Fig. 17 Electrochemical impedance plots for the BSCF/GDC/BSCF symmetrical cell under OCV conditions with *in situ* sintered electrodes at 700 °C in the pO_2 range from 0.02 to 1 atm, (a) impedance spectra (ohmic losses were subtracted for clarity reasons) and (b) corresponding DRTs. Reprinted with permission from ref. 328. Copyright 2017, with permission from The Electrochemical Society.

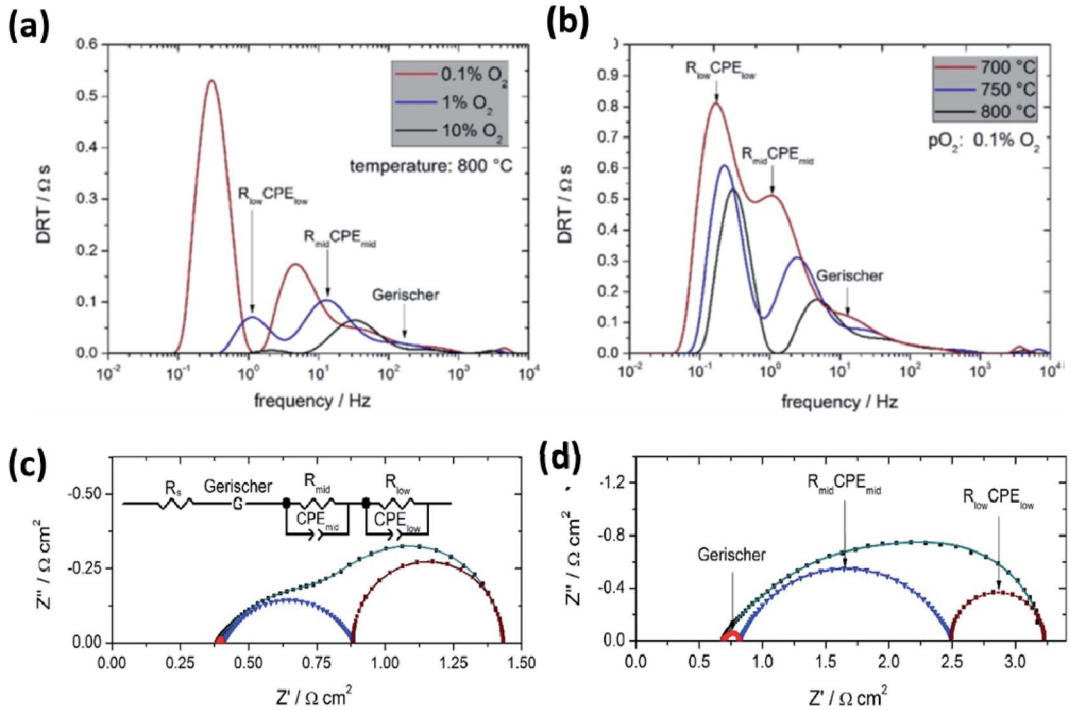

Fig. 18 DRT plots of a symmetrical STF35 electrode under OCV conditions as a function of (a) pO_2 at 800 °C, (b) temperature at 0.1% O_2. Impedance spectra fitted with an ECM at (c) 800 °C and (d) 700 °C in 0.1% O_2. Reprinted with permission from ref. 329. Copyright 2019, with permission from Elsevier.

at lower temperatures was assigned to the incorporation and transfer of O^{2-} in the lattice. The assignment of individual electrochemical processes to peaks in DRT plots was based on other studies, where impedance spectra of the cell were further characterized and analysed as a function of anodic and cathodic gas composition.[326]

Almar *et al.* investigated the ORR of the BSCF/GDC symmetrical cell cathode under OCV conditions, which exhibits fast oxygen-exchange kinetics leading to the impedance spectra showing a semicircle for the Gerischer process instead of the typical tear drop shape[327,328] by DRT (Fig. 16 and 17). P1 showed low thermal deactivation and pO_2 dependence of 0.98, and hence was associated with molecular oxygen diffusion within the cathode setup, the contacting gold meshes and the porous cathode. P2 showed thermal activation and pO_2 dependence of 0.66 and hence was associated with the surface-exchange reaction. P3 also showed thermal activation with pO_2 dependency of 0.09, with a capacitance of 0.05 to 0.08 F cm^{-2} from 600 to 900 °C associated with interfacial capacitances. Hence P3 was attributed to oxide transfer losses across the cathode/electrolyte interface. P4 also showed thermal activation but was pO_2 independent and hence was attributed to electronic current losses between the electrode and the current collector (gold mesh).

Mroziński *et al.* employed the DRT method to validate the ECM fit for $Sr_{0.86}Ti_{0.65}Fe_{0.35}O_3$ (STF35)/GDC symmetrical cells under OCV conditions.[329] Fig. 18a and b show DRT plots at different pO_2 (10%, 1%, and 0.1%), where three peaks were seen at HF, MF, and LFs depending on the pO_2. At low pO_2 (0.1%) additional contribution at LFs was seen, and the HF peak was ascribed to the Gerischer process.[329] The temperature dependent DRT plot at 0.1% oxygen content in Fig. 18b shows that LF contribution is present at all temperatures. From these observations, ECM with the Gerischer element was proposed and the chi-squared parameter was mostly $<10^{-5}$ (Fig. 18c and d). Fitting with different ECMs gave bad fittings along with higher chi-squared values, where adsorption of oxygen species was determined as RDS after analysing the dependence of each peak on pO_2 and temperature, and calculating the activation energy and capacitance values.[329]

DRT analysis of the pO_2 dependence study for $La_{0.85}Sr_{0.15}MnO_{3\pm\delta}$ (LSM) infiltrated $(Bi_{0.8}Er_{0.2})_2O_3$ (ESB)/GDC symmetrical cells under OCV conditions is shown in Fig. 19, where R1 (red) indicates the process of ion transport, R2 (blue) indicates surface chemical reactions, and R3 (dark yellow) indicates gas diffusion.[306] The intermediate peak R2 associated with surface chemical reactions shows strong dependency on pO_2 and its intensity in DRT plots also shows strong correlation with pO_2 and is considered the rate-limiting step. The above-mentioned examples show that DRT analysis has been successfully employed to deconvolute impedance plots for cases with similar relaxation times, resulting in better understanding of individual electrochemical processes occurring in SOFC cathodes. It was also seen in various studies that DRT plots served as a complementary tool for ECM fitting of the impedance data.

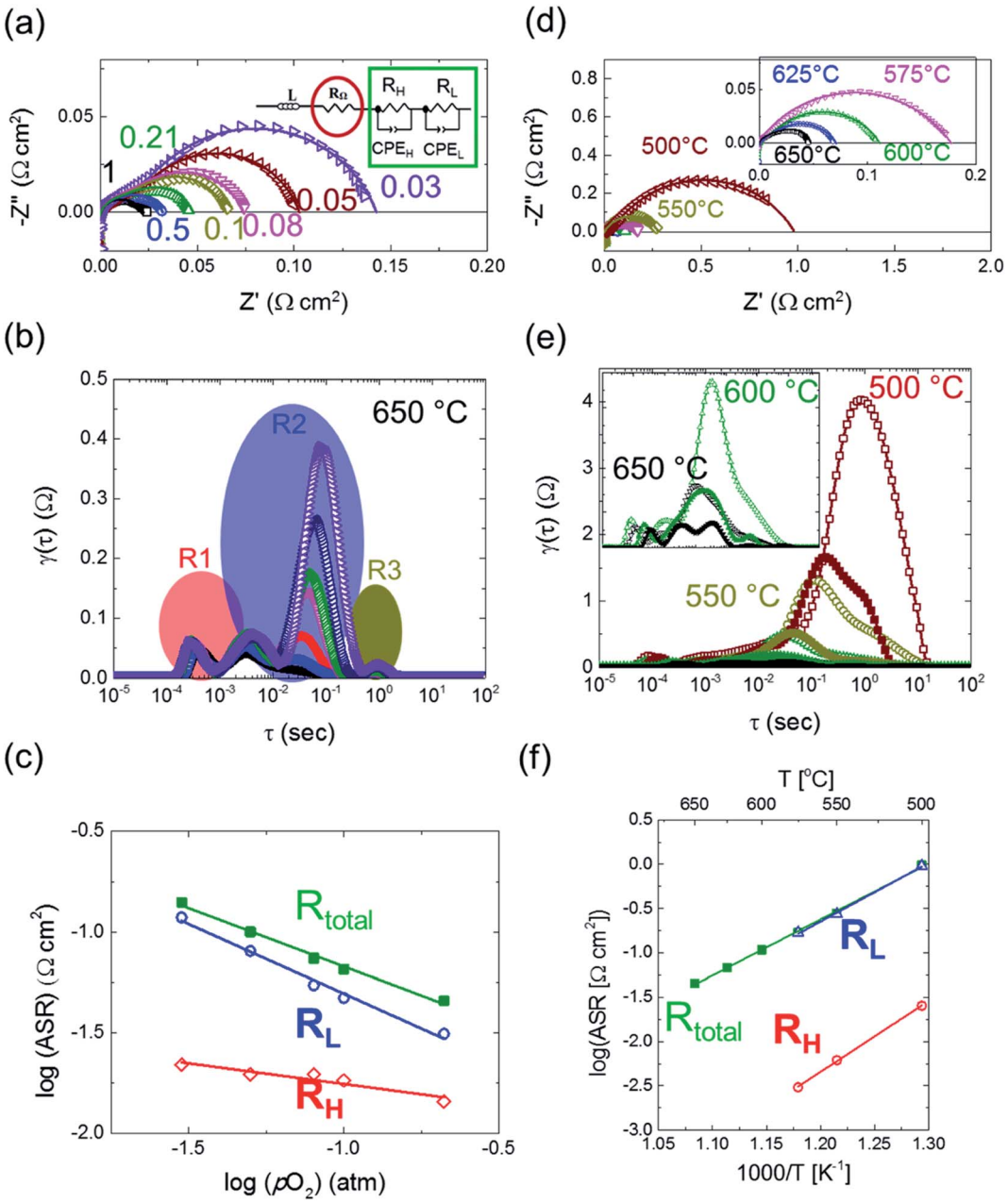

Fig. 19 Electrochemical performance of LSM-i-ESB/GDC symmetrical cells under OCV conditions. (a) pO_2 dependence of impedance spectra at 650 °C, (b) DRT analysis of impedance spectra under different pO_2 at 650 °C, (c) variation of ASR with pO_2 at 650 °C, (d) temperature dependence of impedance spectra in synthetic air, (e) DRT analysis of impedance spectra for symmetrical cells calcined at 650 °C (closed symbols) and 800 °C (open symbols), and (f) Arrhenius plot of cathode ASR. Reprinted with permission from ref. 306. Copyright 2018, with permission from American Chemical Society.

Summary

The evolution of IT-SOFC cathodes has undergone tremendous progress in recent years, particularly towards designing alternative cathode materials that are excellent electrocatalysts, chemically and thermally stable, compatible with IT-SOFC electrolytes, and demonstrate improved electrochemical properties. We have discussed recent advances in the development of IT-SOFC cathodes with respect to material developments and interfacial engineering. LSCF, one of the most investigated MIECs, has demonstrated good ionic and electronic conductivities suitable for IT-SOFC cathodes. However, under the operating conditions, its TEC is incompatible with IT-SOFC electrolytes, and it suffers from surface segregation of Sr and reactivity with other contaminants in the cell. To prevent contaminant-poisoning of LSCF, surface functionalization routes such as infiltration have been proposed. Additionally, double perovskite oxides, especially Co-containing perovskites, have been investigated as cathodes for IT-SOFCs and have demonstrated higher surface exchange kinetics and diffusion

coefficient of oxygen ions and higher electronic conductivities in comparison with ABO_3 disordered perovskite oxides. Additionally, mixing high performing cathode materials with electrolytes in a composite ratio further improves the electrochemical performance and long-term stability of the cathode and increases the power density of the cell. The reduction of oxygen occurs through several intermediate reactions whose kinetics are strongly influenced by the properties of the material, synthesis parameters and operating conditions. By distinguishing the electrode processes and the corresponding relaxation time, DFRT/DRT can be employed to comprehend the intricate ORR process in IT-SOFCs. For example, the DRT analysis on the dependence of LSM-i-ESB on pO_2 suggests that pO_2 is the rate-limiting step in this process.

Author contributions

V. T. planned the review paper. S. A. wrote the section on single perovskite oxides and ORR mechanisms, A. N. wrote the sections on double perovskites and layered Ruddlesden–Popper perovskites and K. S. contributed to the sections on other crystal structures, composite cathodes, and distribution of relaxation times. All authors commented on the paper.

Conflicts of interest

There are no conflicts to declare.

Acknowledgements

The authors would like to thank the Alberta Innovates for supporting this work. One of us (V. T.) would like to dedicate this paper to Professor John Kilner.

References

1 L. Yang, Z. Cheng, M. Liu and L. Wilson, *Energy Environ. Sci.*, 2010, **3**, 1804.
2 M. S. Khan, S.-B. Lee, R.-H. Song, J.-W. Lee, T.-H. Lim and S.-J. Park, *Ceram. Int.*, 2016, **42**, 35–48.
3 E. D. Wachsman and K. T. Lee, *Science*, 2011, **334**, 935–939.
4 D. J. L. Brett, A. Atkinson, N. P. Brandon and S. J. Skinner, *Chem. Soc. Rev.*, 2008, **37**, 1568–1578.
5 D. A. Osinkin, *Electrochim. Acta*, 2021, **372**, 137858.
6 P. M. Shafi, *Perovskite Oxides as Advanced Energy Materials for Solid Oxide Fuel Cell and Supercapacitor Applications*, Springer International Publishing, 2020, pp. 181–204.
7 J. P. Attfield, P. Lightfoot and R. E. Morris, *Dalton Trans.*, 2015, **44**, 10541–10542.
8 I. R. de Larramendi, N. Ortiz-Vitoriano, I. B. Dzul-Bautista and T. Rojo, *Perovskite Materials – Synthesis, Characterisation, Properties, and Applications*, InTech, 2016.
9 A. V. Nikonov, K. A. Kuterbekov, K. Z. Bekmyrza and N. B. Pavzderin, *Eurasian J. Phys. Funct. Mater.*, 2018, **2**, 274–292.
10 T. Jia, Z. Zeng, H. Q. Lin, Y. Duan and P. Ohodnicki, *RSC Adv.*, 2017, **7**, 38798–38804.
11 J. Kim, X. Chen, P. C. Shih and H. Yang, *ACS Sustainable Chem. Eng.*, 2017, **5**, 10910–10917.
12 M. A. Zeb and H. Y. Kee, *Phys. Rev. B: Condens. Matter Mater. Phys.*, 2012, **86**, 1–7.
13 C. F. Chen, G. King, R. M. Dickerson, P. A. Papin, S. Gupta, W. R. Kellogg and G. Wu, *Nano Energy*, 2015, **13**, 423–432.
14 D. P. Tarragó, B. Moreno, E. Chinarro and V. C. de Sousa, *Perovskite Materials – Synthesis, Characterisation, Properties, and Applications*, 2016.
15 P. Kaur and K. Singh, *Ceram. Int.*, 2020, **46**, 5521–5535.
16 X. Xu, W. Wang, W. Zhou and Z. Shao, *Small Methods*, 2018, **2**, 1–35.
17 Z. Li, M. Li and Z. Zhu, *Perovskite Cathode Materials for Low – Temperature Solid Oxide Fuel Cells: Fundamentals to Optimization*, Springer, Singapore, 2021.
18 S. K. Burnwal, S. Bharadwaj and P. Kistaiah, *J. Mol. Eng. Mater.*, 2016, **4**, 1630001.
19 P. Qiu, X. Yang, T. Zhu, S. Sun and L. Jia, *Int. J. Hydrogen Energy*, 2020, **45**, 23160–23173.
20 S. T. Aruna, L. S. Balaji, S. S. Kumar and B. S. Prakash, *Renewable Sustainable Energy Rev.*, 2017, **67**, 673–682.
21 S. Jo, B. Sharma, D. Hwan and P. Jea, *J. Korean Ceram. Soc.*, 2020, **57**, 135–151.
22 A. M. Abdalla, S. Hossain, A. T. Azad and P. M. I. Petra, *Renewable Sustainable Energy Rev.*, 2018, **82**, 353–368.
23 B. Madhavan and A. Ashok, *Ionics*, 2015, **21**, 601–610.
24 X. Huang, G. Zhao, G. Wang and J. T. S. Irvine, *Chem. Sci.*, 2018, **9**, 3623–3637.
25 A. Junaida, A. Aziz, N. Akidah, M. Rao and A. Muchtar, *Ceram. Int.*, 2020, **46**, 23314–23325.
26 S. P. Jiang, *J. Mater. Sci.*, 2008, **43**, 6799–6833.
27 C. Sun, R. Hui and J. Roller, *J. Solid State Electrochem.*, 2010, **14**, 1125–1144.
28 A. Jun, J. Kim, J. Shin and G. Kim, *ChemElectroChem*, 2016, **3**, 511–530.
29 A. J. Jacobson, *Chem. Mater.*, 2010, **22**, 660–674.
30 S. P. Jiang, *Int. J. Hydrogen Energy*, 2019, **44**, 7448–7493.
31 S. S. Hashim, F. Liang, W. Zhou and J. Sunarso, *ChemElectroChem*, 2019, **6**, 3549–3569.
32 G. C. Kostogloudis and C. Ftikos, *Solid State Ionics*, 1999, **126**, 143–151.
33 Y. Teraoka, H. M. Zhang, K. Okamoto and N. Yamazoe, *Mater. Res. Bull.*, 1988, **23**, 51–58.
34 X. Ding, X. Kong, X. Wang, J. Jiang and C. Cui, *J. Alloys Compd.*, 2010, **502**, 472–476.
35 H. Uchida, S. I. Arisaka and M. Watanabe, *Electrochem. Solid-State Lett.*, 1999, **2**, 428–430.
36 A. Mai, V. A. C. Haanappel, F. Tietz and D. Stöver, *Solid State Ionics*, 2006, **177**, 2103–2107.
37 F. Giannici, G. Canu, A. Chiara, M. Gambino, C. Aliotta, A. Longo, V. Buscaglia and A. Martorana, *ACS Appl. Mater. Interfaces*, 2017, **9**, 44466–44477.
38 W. Lee, J. W. Han, Y. Chen, Z. Cai and B. Yildiz, *J. Am. Chem. Soc.*, 2013, **135**, 7909–7925.
39 M. Niania, R. Podor, T. Ben Britton, C. Li, S. J. Cooper, N. Svetkov, S. Skinner and J. Kilner, *J. Mater. Chem. A*, 2018, **6**, 14120–14135.

40 Y. Wen, T. Yang, D. Lee, H. N. Lee, E. J. Crumlin and K. Huang, *J. Mater. Chem. A*, 2018, **6**, 24378–24388.
41 T. T. Fister, D. D. Fong, J. A. Eastman, P. M. Baldo, M. J. Highland, P. H. Fuoss, K. R. Balasubramaniam, J. C. Meador and P. A. Salvador, *Appl. Phys. Lett.*, 2008, **93**, 151904.
42 S. P. Jiang, *Int. J. Hydrogen Energy*, 2019, **44**, 7448–7493.
43 V. Sharma, M. K. Mahapatra, P. Singh and R. Ramprasad, *J. Mater. Sci.*, 2015, **50**, 3051–3056.
44 V. Sharma, M. K. Mahapatra, P. Singh and R. Ramprasad, *J. Mater. Sci.*, 2015, **50**, 3051–3056.
45 F. Qiang, K. N. Sun, N. Q. Zhang, X. D. Zhu, S. R. Le and D. R. Zhou, *J. Power Sources*, 2007, **168**, 338–345.
46 H. Wang, K. J. Yakal-Kremski, T. Yeh, G. M. Rupp, A. Limbeck, J. Fleig and S. A. Barnett, *J. Electrochem. Soc.*, 2016, **163**, F581–F585.
47 L. Zhao, J. Drennan, C. Kong, S. Amarasinghe and S. P. Jiang, *J. Mater. Chem. A*, 2014, **2**, 11114–11123.
48 M. Kubicek, A. Limbeck, T. Frömling, H. Hutter and J. Fleig, *J. Electrochem. Soc.*, 2011, **158**, B727.
49 B. Fan and X. Liu, *Solid State Ionics*, 2009, **180**, 973–977.
50 M. Li, M. Zhao, F. Li, W. Zhou, V. K. Peterson, X. Xu, Z. Shao, I. Gentle and Z. Zhu, *Nat. Commun.*, 2017, **8**, 1–9.
51 H. Ding, A. V. Virkar, M. Liu and F. Liu, *Phys. Chem. Chem. Phys.*, 2013, **15**, 489–496.
52 M. E. Lynch, L. Yang, W. Qin, J. J. Choi, M. Liu, K. Blinn and M. Liu, *Energy Environ. Sci.*, 2011, **4**, 2249–2258.
53 A. Giuliano, M. P. Carpanese, D. Clematis, M. Boaro, A. Pappacena, F. Deganello, L. F. Liotta and A. Barbucci, *J. Electrochem. Soc.*, 2017, **164**, F3114–F3122.
54 I. Sreedhar, B. Agarwal, P. Goyal and A. Agarwal, *J. Solid State Electrochem.*, 2020, **24**, 1239–1270.
55 Z. Yang, M. Guo, N. Wang, C. Ma, J. Wang and M. Han, *Int. J. Hydrogen Energy*, 2017, **42**, 24948–24959.
56 K. Chen, N. Ai, K. M. O'Donnell and S. P. Jiang, *Phys. Chem. Chem. Phys.*, 2015, **17**, 4870–4874.
57 C. C. Wang, D. Luo, S. P. Jiang and B. Lin, *J. Phys. D: Appl. Phys.*, 2018, **51**, 435502.
58 B. Gedziorowski, K. Świerczek and J. Molenda, *Solid State Ionics*, 2012, **225**, 437–442.
59 J. W. Stevenson, I. Armstrong, R. D. Carneim, L. I. Pederson and W. J. Weber, *J. Electrochem. Soc.*, 1996, **143**, 2722–2729.
60 K. Yasumoto, Y. Inagaki, M. Shiono and M. Dokiya, *Solid State Ionics*, 2002, **148**, 545–549.
61 J. Ryu, T. Noh, Y. N. Kim and H. Lee, *J. Ceram. Soc. Jpn.*, 2012, **120**, 594–598.
62 M. Hussain, M. Muneer, G. Abbas, I. Shakir, A. Iqbal, M. A. Javed, M. Iqbal, Z. Ur-Rehman and R. Raza, *Ceram. Int.*, 2020, **46**, 18208–18215.
63 Q. Zhou, L. Xu, Y. Guo, D. Jia, Y. Li and W. C. J. Wei, *Int. J. Hydrogen Energy*, 2012, **37**, 11963–11968.
64 T. Noh, J. Ryu, J. Kim, Y. Kim and H. Lee, *J. Alloys Compd.*, 2013, **557**, 196–201.
65 J. Lu, Y. Yin, J. Li, L. Xu and Z. Ma, *Electrochem. Commun.*, 2015, **61**, 18–22.
66 S. Pang, W. Wang, T. Chen, X. Shen, Y. Wang, K. Xu and X. Xi, *J. Power Sources*, 2016, **326**, 176–181.
67 F. Zurlo, E. Di Bartolomeo, A. D'Epifanio, V. Felice, I. Natali Sora, L. Tortora and S. Licoccia, *J. Power Sources*, 2014, **271**, 187–194.
68 M. Bilal, J. Gao, K. Shaheen, Y. Wang, M. Yasir, S. Zhang, C. Li and C. Li, *J. Power Sources*, 2020, **472**, 228498.
69 J. C. Lin, F. P. Ting, T. Y. Lee, S. Der Chyou and C. M. Lai, *Int. J. Hydrogen Energy*, 2013, **38**, 1714–1724.
70 M. Wu, H. Cai, F. Jin, N. Sun, J. Xu, L. Zhang, X. Han, S. Wang, X. Su, W. Long, L. Wang and L. Zhang, *J. Eur. Ceram. Soc.*, 2021, **41**, 2682–2690.
71 Y. Yamaguchi, I. Kagomiya, S. Minami and H. Shimada, *J. Power Sources*, 2020, **448**, 227426.
72 C. Feo, I. Kagomiya, T. Murayama, K. Tsunekawa, K. Kakimoto and Y. Ogura, *J. Eur. Ceram. Soc.*, 2019, **39**, 1082–1092.
73 Y. Zhen, A. I. Y. Tok, F. Y. C. Boey and S. P. Jiang, *Electrochem. Solid-State Lett.*, 2008, **11**, 42–46.
74 X. Fu, M. Liu, X. Meng, S. Lü, D. Wang, Y. Zhang, H. Liu, M. Song, Z. Li and L. Wang, *Ionics*, 2020, **26**, 1285–1295.
75 V. Ramaswamy, P. Awati and A. K. Tyagi, *J. Alloys Compd.*, 2004, **364**, 180–185.
76 K. T. Lee and A. Manthiram, *J. Electrochem. Soc.*, 2006, **153**, A794.
77 C. Rossignol, J. M. Ralph, J. M. Bae and J. T. Vaughey, *Solid State Ionics*, 2004, **175**, 59–61.
78 H. Ullmann, N. Trofimenko, F. Tietz, D. Stöver and A. Ahmad-Khanlou, *Solid State Ionics*, 2000, **138**, 79–90.
79 J. M. Serra, V. B. Vert, M. Betz, V. A. C. Haanappel, W. A. Meulenberg and F. Tietz, *J. Electrochem. Soc.*, 2008, **155**, B207.
80 S. D. Priya, A. S. Nesaraj and A. I. Selvakumar, *Bull. Mater. Sci.*, 2021, 2–8.
81 S. Mulmi and V. Thangadurai, *Chem. Commun.*, 2019, **55**, 3713–3716.
82 J. Yin, Y. Yin, J. Lu, C. Zhang, N. Q. Minh and Z. Ma, *J. Phys. Chem. C*, 2014, **118**, 13357–13368.
83 E. Olsson, J. Cottom, X. Aparicio-Anglès and N. H. De Leeuw, *Phys. Chem. Chem. Phys.*, 2020, **22**, 692–699.
84 H. Zhang, G. Chen and L. Tang, *Chem. Commun.*, 2020, **56**, 1361–1364.
85 E. Olsson, X. Aparicio-Anglès and N. H. De Leeuw, *Phys. Chem. Chem. Phys.*, 2017, **19**, 13960–13969.
86 I. Susanto, D. M. Kamal, S. Ruswanto, R. Subarkah, F. Zainuri, S. Permana, J. W. Soedarsono, A. Subardi and Y. P. Fu, *East.-Eur. J. Enterp. Technol.*, 2020, **6**, 15–20.
87 C. Xia, W. Rauch, F. Chen and M. Liu, *Solid State Ionics*, 2002, **149**, 11–19.
88 L. M. Acuña, J. Peña-Martínez, D. Marrero-López, R. O. Fuentes, P. Nuñez and D. G. Lamas, *J. Power Sources*, 2011, **196**, 9276–9283.
89 H. Lv, B. Y. Zhao, Y. J. Wu, G. Sun, G. Chen and K. A. Hu, *Mater. Res. Bull.*, 2007, **42**, 1999–2012.
90 W. Chen, T. Wen, H. Nie and R. Zheng, *Mater. Res. Bull.*, 2003, **38**, 1319–1328.
91 H. Y. Tu, Y. Takeda, N. Imanishi and O. Yamamoto, *Solid State Ionics*, 1999, **117**, 277–281.

92 Z. Liu, L. Z. Cheng and M. F. Han, *J. Power Sources*, 2011, **196**, 868–871.
93 Z. Bin Yang, M. F. Han, P. Zhu, F. Zhao and F. Chen, *Int. J. Hydrogen Energy*, 2011, **36**, 9162–9168.
94 B. Wei, Z. Lü, X. Huang, M. Liu, N. Li and W. Su, *J. Power Sources*, 2008, **176**, 1–8.
95 Y. Cheng, Q. Zhou, W. Li, T. Wei, Z. Li, D. An, X. Tong, Z. Ji and X. Han, *J. Alloys Compd.*, 2015, **641**, 234–237.
96 W. Zhou, Z. Shao, R. Ran, W. Jin and N. Xu, *Chem. Commun.*, 2008, 5791–5793.
97 F. Wang, Q. Zhou, T. He, G. Li and H. Ding, *J. Power Sources*, 2010, **195**, 3772–3778.
98 D. Chen, C. Chen, Y. Gao, Z. Zhang, Z. Shao and F. Ciucci, *J. Power Sources*, 2015, **295**, 117–124.
99 T. Yang, X. Jin and K. Huang, *J. Membr. Sci.*, 2018, **568**, 47–54.
100 J. Wang, T. Yang, Y. Wen, Y. Zhang, C. Sun and K. Huang, *J. Power Sources*, 2019, **414**, 24–30.
101 M. Li, W. Zhou, V. K. Peterson, M. Zhao and Z. Zhu, *J. Mater. Chem. A*, 2015, **3**, 24064–24070.
102 Y. Zhu, Z.-G. Chen, W. Zhou, S. Jiang, J. Zou and Z. Shao, *ChemSusChem*, 2013, **6**, 2249–2254.
103 M. Li, W. Zhou and Z. Zhu, *ChemElectroChem*, 2015, **2**, 1331–1338.
104 J. Wang, T. Yang, L. Lei and K. Huang, *J. Mater. Chem. A*, 2017, **5**, 8989–9002.
105 T. Yang, Y. Wen, T. Wu, N. Xu and K. Huang, *J. Mater. Chem. A*, 2020, **8**, 82–86.
106 V. Cascos, L. Troncoso and J. A. Alonso, *Int. J. Hydrogen Energy*, 2015, **40**, 11333–11341.
107 Y. Shen, F. Wang, X. Ma and T. He, *J. Power Sources*, 2011, **196**, 7420–7425.
108 Y. Li, Y. N. Kim, J. Cheng, J. A. Alonso, Z. Hu, Y.-Y. Chin, T. Takami, M. T. Fernández-Díaz, H.-J. Lin, C.-T. Chen, L. H. Tjeng, A. Manthiram and J. B. Goodenough, *Chem. Mater.*, 2011, **23**, 5037–5044.
109 M. J. Akhtar and R. T. A. Khan, *Mater. Charact.*, 2011, **62**, 1016–1020.
110 S. Jiang, W. Zhou, Y. Niu, Z. Zhu and Z. Shao, *ChemSusChem*, 2012, **5**, 2023–2031.
111 Q. Zhou, L. Zhang and T. He, *Electrochem. Commun.*, 2010, **12**, 285–287.
112 L. Yan, H. Ding, Z. Zhu and X. Xue, *J. Power Sources*, 2011, **196**, 9352–9355.
113 X. Yu, W. Long, F. Jin and T. He, *Electrochim. Acta*, 2014, **123**, 426–434.
114 S. Misra, *Mater. Chem. Phys.*, 2017, **190**, 1–7.
115 Q. Li, T. Xia, L. Sun, H. Zhao and L. Huo, *Electrochim. Acta*, 2014, **150**, 151–156.
116 N. T. M. Nhung and H. J. Kim, *New Phys.: Sae Mulli*, 2021, **71**, 446–449.
117 P. Kaur and K. Singh, *ECS Trans.*, 2019, **91**, 1543–1550.
118 Z. Shao and S. M. Haile, *Materials for Sustainable Energy*, co-published with Macmillan Publishers Ltd, UK, 2010, pp. 255–258.
119 A. Yan, M. Cheng, Y. Dong, W. Yang, V. Maragou, S. Song and P. Tsiakaras, *Appl. Catal., B*, 2006, **66**, 64–71.
120 D. Liu, Y. Dou, T. Xia, Q. Li, L. Sun, L. Huo and H. Zhao, *J. Power Sources*, 2021, **494**, 229778.
121 Y. Ling, X. Zhang, Z. Wang, S. Wang, L. Zhao, X. Liu and B. Lin, *Int. J. Hydrogen Energy*, 2013, **38**, 14323–14328.
122 J. Gao, Q. Li, Z. Zhang, Z. Lü and B. Wei, *Electrochem. Commun.*, 2021, **125**, 106978.
123 M. Li, Y. Wang, Y. Wang, F. Chen and C. Xia, *ACS Appl. Mater. Interfaces*, 2014, **6**, 11286–11294.
124 S. Huang, F. Gao, Z. Meng, S. Feng, X. Sun, Y. Li and C. Wang, *ChemElectroChem*, 2014, **1**, 554–558.
125 J. Gao, Q. Li, W. Xia, L. Sun, L.-H. Huo and H. Zhao, *ACS Sustainable Chem. Eng.*, 2019, **7**, 18647–18656.
126 Y. Niu, J. Sunarso, F. Liang, W. Zhou, Z. Zhu and Z. Shao, *J. Electrochem. Soc.*, 2011, **158**, B132.
127 W. Xia, Q. Li, L. Sun, L. Huo and H. Zhao, *J. Alloys Compd.*, 2020, **835**, 155406.
128 A. Wedig, R. Merkle, B. Stuhlhofer, H. U. Habermeier, J. Maier and E. Heifets, *Phys. Chem. Chem. Phys.*, 2011, **13**, 16530–16533.
129 J. M. Porras-Vazquez, T. Pike, C. A. Hancock, J. F. Marco, F. J. Berry and P. R. Slater, *J. Mater. Chem. A*, 2013, **1**, 11834–11841.
130 J. M. Porras-Vazquez and P. R. Slater, *Fuel Cells*, 2012, **12**, 1056–1063.
131 J. Liu, J. Wang, A. Belotti and F. Ciucci, *ACS Appl. Energy Mater.*, 2019, **2**, 5472–5480.
132 C. A. Hancock and P. R. Slater, *Dalton Trans.*, 2011, **40**, 5599.
133 C. A. Hancock, R. C. T. Slade, J. R. Varcoe and P. R. Slater, *J. Solid State Chem.*, 2011, **184**, 2972–2977.
134 J. M. Porras-Vazquez and P. R. Slater, *J. Power Sources*, 2012, **209**, 180–183.
135 J. M. Porras-Vazquez, T. F. Kemp, J. V. Hanna and P. R. Slater, *J. Mater. Chem.*, 2012, **22**, 8287.
136 O. V. Belyaeva, T. A. Krasnova, S. A. Semenova and O. S. Gladkova, *Solid Fuel Chem.*, 2011, **45**, 418–421.
137 I. Yasuda, K. Ogasawara, M. Hishinuma, T. Kawada and M. Dokiya, *Solid State Ionics*, 1996, **86–88**, 1197–1201.
138 F. Tietz, I. Arul Raj, M. Zahid and D. Stöver, *Solid State Ionics*, 2006, **177**, 1753–1756.
139 Y. C. Wu, P. Y. Huang and G. Xu, *Ceram. Int.*, 2017, **43**, 2460–2470.
140 L. Tai, *Solid State Ionics*, 1995, **76**, 259–271.
141 A. Esquirol, N. P. Brandon, J. A. Kilner and M. Mogensen, *J. Electrochem. Soc.*, 2004, **151**, A1847.
142 L. W. Tai, M. M. Nasrallah, H. U. Anderson, D. M. Sparlin and S. R. Sehlin, *Solid State Ionics*, 1995, **76**, 259–271.
143 E. V. Tsipis, M. V. Patrakeev, V. V. Kharton, A. A. Yaremchenko, G. C. Mather, A. L. Shaula, I. A. Leonidov, V. L. Kozhevnikov and J. R. Frade, *Solid State Sci.*, 2005, **7**, 355–365.
144 G. Kim, S. Wang, A. J. Jacobson, L. Reimus, P. Brodersen and C. A. Mims, *J. Mater. Chem.*, 2007, **17**, 2500.
145 Y. Tian, Y. Liu, W. Wang, L. Jia, J. Pu, B. Chi and J. Li, *J. Energy Chem.*, 2020, **43**, 108–115.
146 M. C. Knapp and P. M. Woodward, *J. Solid State Chem.*, 2006, **179**, 1076–1085.

147 P. K. Davies, *Curr. Opin. Solid State Mater. Sci.*, 1999, **4**, 467–471.
148 L. Lo Presti, M. Allieta, M. Scavini, P. Ghigna, L. Loconte, V. Scagnoli and M. Brunelli, *Phys. Rev. B: Condens. Matter Mater. Phys.*, 2011, **84**, 104107.
149 S. Streule, A. Podlesnyak, E. Pomjakushina, K. Conder, D. Sheptyakov, M. Medarde and J. Mesot, *Phys. B*, 2006, **378–380**, 539–540.
150 C. Bernuy-Lopez, K. Høydalsvik, M.-A. Einarsrud and T. Grande, *Materials*, 2016, **9**, 154.
151 S. Wang, J. Zan, W. Qiu, D. Zheng, F. Li, W. Chen, Q. Pei and L. Jiang, *J. Electroanal. Chem.*, 2021, **886**, 115144.
152 J.-H. Kim and A. Manthiram, *J. Electrochem. Soc.*, 2008, **155**, B385.
153 A. Talapatra, B. P. Uberuaga, C. R. Stanek and G. Pilania, *Chem. Mater.*, 2021, **33**, 845–858.
154 A. A. Taskin, A. N. Lavrov and Y. Ando, *Appl. Phys. Lett.*, 2005, **86**, 091910.
155 J.-H. Kim, L. Mogni, F. Prado, A. Caneiro, J. A. Alonso and A. Manthiram, *J. Electrochem. Soc.*, 2009, **156**, B1376.
156 D. S. Tsvetkov, I. L. Ivanov and A. Y. Zuev, *J. Solid State Chem.*, 2013, **199**, 154–159.
157 Z. Zhang, D. Xie, J. Ni and C. Ni, *Ceram. Int.*, 2021, **47**, 14673–14679.
158 M. C. L. Cheah, B. J. Kennedy, R. L. Withers, M. Yonemura and T. Kamiyama, *J. Solid State Chem.*, 2006, **179**, 2487–2494.
159 B. Manoun, A. Ezzahi, S. Benmokhtar, A. Ider, P. Lazor, L. Bih and J. M. Igartua, *J. Alloys Compd.*, 2012, **533**, 43–52.
160 L. Suescun, C. Y. Jones, C. A. Cardoso, J. W. Lynn, B. H. Toby, F. M. Araújo-Moreira, O. F. de Lima, H. Pardo and A. W. Mombrú, *Phys. Rev. B: Condens. Matter Mater. Phys.*, 2005, **71**, 144405.
161 H. Pardo, W. A. Ortiz, F. M. Araújo-Moreira, L. Suescun, B. Toby, E. Quagliata, C. A. Negreira, K. Prassides and A. W. Mombrú, *Phys. C*, 1999, **313**, 105–114.
162 J. Androulakis, N. Katsarakis, J. Giapintzakis, N. Vouroutzis, E. Pavlidou, K. Chrissafis, E. K. Polychroniadis and V. Perdikatsis, *J. Solid State Chem.*, 2003, **173**, 350–354.
163 L. Jiang, F. Li, T. Wei, R. Zeng and Y. Huang, *Electrochim. Acta*, 2014, **133**, 364–372.
164 F. Jin, H. Xu, W. Long, Y. Shen and T. He, *J. Power Sources*, 2013, **243**, 10–18.
165 F. Jin, Y. Shen, R. Wang and T. He, *J. Power Sources*, 2013, **234**, 244–251.
166 L. Zhao, J. Shen, B. He, F. Chen and C. Xia, *Int. J. Hydrogen Energy*, 2011, **36**, 3658–3665.
167 A. K. Azad, J. H. Kim and J. T. S. Irvine, *J. Power Sources*, 2011, **196**, 7333–7337.
168 S. Choi, S. Yoo, J. Kim, S. Park, A. Jun, S. Sengodan, J. Kim, J. Shin, H. Y. Jeong, Y. Choi, G. Kim and M. Liu, *Sci. Rep.*, 2013, **3**, 2426.
169 C. Lim, S. Sengodan, D. Jeong, J. Shin and G. Kim, *Int. J. Hydrogen Energy*, 2019, **44**, 1088–1095.
170 Y. N. Kim, J.-H. Kim and A. Manthiram, *J. Power Sources*, 2010, **195**, 6411–6419.
171 M. West and A. Manthiram, *Int. J. Hydrogen Energy*, 2013, **38**, 3364–3372.
172 F. Jin, L. Li and T. He, *J. Power Sources*, 2015, **273**, 591–599.
173 X. Che, Y. Shen, H. Li and T. He, *J. Power Sources*, 2013, **222**, 288–293.
174 S. Yoo, S. Choi, J. Kim, J. Shin and G. Kim, *Electrochim. Acta*, 2013, **100**, 44–50.
175 N. E. Volkova, L. Y. Gavrilova, V. A. Cherepanov, T. V. Aksenova, V. A. Kolotygin and V. V. Kharton, *J. Solid State Chem.*, 2013, **204**, 219–223.
176 A. Olszewska, Y. Zhang, Z. Du, M. Marzec, K. Świerczek, H. Zhao and B. Dabrowski, *Int. J. Hydrogen Energy*, 2019, **44**, 27587–27599.
177 A. Jun, J. Kim, J. Shin and G. Kim, *Int. J. Hydrogen Energy*, 2012, **37**, 18381–18388.
178 Y. Zhang, B. Yu, S. Lü, X. Meng, X. Zhao, Y. Ji, Y. Wang, C. Fu, X. Liu, X. Li, Y. Sui, J. Lang and J. Yang, *Electrochim. Acta*, 2014, **134**, 107–115.
179 J. Xue, Y. Shen and T. He, *J. Power Sources*, 2011, **196**, 3729–3735.
180 A. Maignan, C. Martin, D. Pelloquin, N. Nguyen and B. Raveau, *J. Solid State Chem.*, 1999, **142**, 247–260.
181 J.-H. Kim, F. Prado and A. Manthiram, *J. Electrochem. Soc.*, 2008, **155**, B1023.
182 L. Li, F. Jin, Y. Shen and T. He, *Electrochim. Acta*, 2015, **182**, 682–692.
183 J. Kim, A. Jun, J. Shin and G. Kim, *J. Am. Ceram. Soc.*, 2014, **97**, 651–656.
184 C. Kuroda, K. Zheng and K. Świerczek, *Int. J. Hydrogen Energy*, 2013, **38**, 1027–1038.
185 T. V. Aksenova, L. Y. Gavrilova, D. S. Tsvetkov, V. I. Voronin and V. A. Cherepanov, *Russ. J. Phys. Chem. A*, 2011, **85**, 427–432.
186 J.-H. Kim, Y. N. Kim, Z. Bi, A. Manthiram, M. P. Paranthaman and A. Huq, *Solid State Ionics*, 2013, **253**, 81–87.
187 C. Frontera, A. Caneiro, A. E. Carrillo, J. Oró-Solé and J. L. García-Muñoz, *Chem. Mater.*, 2005, **17**, 5439–5445.
188 Y. Zhang, B. Niu, X. Hao, Y. Wang, J. Liu, P. Jiang and T. He, *Electrochim. Acta*, 2021, **370**, 137807.
189 V. S. Kudyakova, B. V. Politov, A. Y. Suntsov and V. L. Kozhevnikov, *J. Solid State Chem.*, 2020, **287**, 121382.
190 K. Zhang, L. Ge, R. Ran, Z. Shao and S. Liu, *Acta Mater.*, 2008, **56**, 4876–4889.
191 H. Téllez, J. Druce, J. A. Kilner and T. Ishihara, *Faraday Discuss.*, 2015, **182**, 145–157.
192 Y.-H. Joung, H. Il Kang, W. S. Choi and J. H. Kim, *Electron. Mater. Lett.*, 2013, **9**, 463–465.
193 D. Fu, F. Jin and T. He, *J. Power Sources*, 2016, **313**, 134–141.
194 G. Kim, S. Wang, A. J. Jacobson, Z. Yuan, W. Donner, C. L. Chen, L. Reimus, P. Brodersen and C. A. Mims, *Appl. Phys. Lett.*, 2006, **88**, 024103.
195 A. Tarancón, M. Burriel, J. Santiso, S. J. Skinner and J. A. Kilner, *J. Mater. Chem.*, 2010, **20**, 3799.
196 J.-H. Kim and A. Manthiram, *J. Mater. Chem. A*, 2015, **3**, 24195–24210.

197 S. Park, S. Choi, J. Kim, J. Shin and G. Kim, *ECS Electrochem. Lett.*, 2012, **1**, F29–F32.
198 B. Wei, M. Schroeder and M. Martin, *ACS Appl. Mater. Interfaces*, 2018, **10**, 8621–8629.
199 U. Anjum, M. Agarwal, T. S. Khan, P. Prateek, R. K. Gupta and M. A. Haider, *Nanoscale*, 2019, **11**, 21404–21418.
200 M. Arnold, H. Wang and A. Feldhoff, *J. Membr. Sci.*, 2007, **293**, 44–52.
201 L. Zhu, B. Wei, Z. Lü, J. Feng, L. Xu, H. Gao, Y. Zhang and X. Huang, *Appl. Surf. Sci.*, 2017, **416**, 649–655.
202 J. Yi, S. Feng, Y. Zuo, W. Liu and C. Chen, *Chem. Mater.*, 2005, **17**, 5856–5861.
203 W. Lee, J. W. Han, Y. Chen, Z. Cai and B. Yildiz, *J. Am. Chem. Soc.*, 2013, **135**, 7909–7925.
204 L. Zhu, B. Wei, Z. Wang, K. Chen, H. Zhang, Y. Zhang, X. Huang and Z. Lü, *ChemSusChem*, 2016, **9**, 2443–2450.
205 L. Zhao, J. Drennan, C. Kong, S. Amarasinghe and S. P. Jiang, *J. Mater. Chem. A*, 2014, **2**, 11114–11123.
206 Y. Li, W. Zhang, Y. Zheng, J. Chen, B. Yu, Y. Chen and M. Liu, *Chem. Soc. Rev.*, 2017, **46**, 6345–6378.
207 H. Kwon, W. Lee and J. W. Han, *RSC Adv.*, 2016, **6**, 69782–69789.
208 W. Xia, X. Liu, F. Jin, X. Jia, Y. Shen and J. Li, *Electrochim. Acta*, 2020, **364**, 137274.
209 Y. Chen, S. Yoo, Y. Choi, J. H. Kim, Y. Ding, K. Pei, R. Murphy, Y. Zhang, B. Zhao, W. Zhang, H. Chen, Y. Chen, W. Yuan, C. Yang and M. Liu, *Energy Environ. Sci.*, 2018, **11**, 2458–2466.
210 S. Joo, J. Kim, J. Shin, T.-H. Lim and G. Kim, *J. Electrochem. Soc.*, 2016, **163**, F1489–F1495.
211 K. Gaur, S. C. Verma and H. B. Lal, *J. Mater. Sci.*, 1988, **23**, 1725–1728.
212 J. Liu, F. Jin, X. Yang, B. Niu, Y. Li and T. He, *Electrochim. Acta*, 2019, **297**, 344–354.
213 P. Datta, P. Majewski and F. Aldinger, *J. Eur. Ceram. Soc.*, 2009, **29**, 1463–1468.
214 J. H. Kim and J. T. S. Irvine, *Int. J. Hydrogen Energy*, 2012, **37**, 5920–5929.
215 J. Xue, Y. Shen and T. He, *Int. J. Hydrogen Energy*, 2011, **36**, 6894–6898.
216 Z. Du, C. Yan, H. Zhao, Y. Zhang, C. Yang, S. Yi, Y. Lu and K. Świerczek, *J. Mater. Chem. A*, 2017, **5**, 25641–25651.
217 D. Fu, F. Jin and T. He, *J. Power Sources*, 2016, **313**, 134–141.
218 F. Meng, T. Xia, J. Wang, Z. Shi and H. Zhao, *J. Power Sources*, 2015, **293**, 741–750.
219 S. Pang, X. Jiang, X. Li, Q. Wang and Z. Su, *J. Power Sources*, 2012, **204**, 53–59.
220 Q. Zhou, T. He, Q. He and Y. Ji, *Electrochem. Commun.*, 2009, **11**, 80–83.
221 T. Broux, M. Bahout, J. M. Hanlon, O. Hernandez, S. Paofai, A. Berenov and S. J. Skinner, *J. Mater. Chem. A*, 2014, **2**, 17015–17023.
222 S. H. Jo, P. Muralidharan and D. K. Kim, *Electrochem. Commun.*, 2009, **11**, 2085–2088.
223 Q. Zhou, Y. Zhang, Y. Shen and T. He, *J. Electrochem. Soc.*, 2010, **157**, B628.
224 L. Zhao, Q. Nian, B. He, B. Lin, H. Ding, S. Wang, R. Peng, G. Meng and X. Liu, *J. Power Sources*, 2010, **195**, 453–456.
225 R. Schmidt, J. Wu, C. Leighton and I. Terry, *Phys. Rev. B: Condens. Matter Mater. Phys.*, 2009, **79**, 125105.
226 Q. Zhou, F. Wang, Y. Shen and T. He, *J. Power Sources*, 2010, **195**, 2174–2181.
227 X. Kong and X. Ding, *Int. J. Hydrogen Energy*, 2011, **36**, 15715–15721.
228 X. Mao, T. Yu and G. Ma, *J. Alloys Compd.*, 2015, **637**, 286–290.
229 W. Wang, T. S. Peh, S. H. Chan and T. S. Zhang, *ECS Trans.*, 2019, **25**, 2277–2281.
230 Q. Zhou, W. C. J. Wei, Y. Guo and D. Jia, *Electrochem. Commun.*, 2012, **19**, 36–38.
231 J. Zou, J. Park, B. Kwak, H. Yoon and J. Chung, *Solid State Ionics*, 2012, **206**, 112–119.
232 L. Jiang, T. Wei, R. Zeng, W.-X. Zhang and Y.-H. Huang, *J. Power Sources*, 2013, **232**, 279–285.
233 B. Wang, G. Long, Y. Ji, M. Pang and X. Meng, *J. Alloys Compd.*, 2014, **606**, 92–96.
234 Q. Zhou, T. He and Y. Ji, *J. Power Sources*, 2008, **185**, 754–758.
235 J. H. Kim, M. Cassidy, J. T. S. Irvine and J. Bae, *J. Electrochem. Soc.*, 2009, **156**, B682.
236 J. H. Kim, M. Cassidy, J. T. S. Irvine and J. Bae, *Chem. Mater.*, 2010, **22**, 883–892.
237 Y. Wang, X. Zhao, S. Lü, X. Meng, Y. Zhang, B. Yu, X. Li, Y. Sui, J. Yang, C. Fu and Y. Ji, *Ceram. Int.*, 2014, **40**, 11343–11350.
238 F. Meng, T. Xia, J. Wang, Z. Shi, J. Lian, H. Zhao, J.-M. Bassat and J.-C. Grenier, *Int. J. Hydrogen Energy*, 2014, **39**, 4531–4543.
239 H. Zhao, Y. Zheng, C. Yang, Y. Shen, Z. Du and K. Świerczek, *Int. J. Hydrogen Energy*, 2013, **38**, 16365–16372.
240 W. Li, Y. Cheng, Q. Zhou, T. Wei, Z. Li, H. Yan, Z. Wang and X. Han, *Ceram. Int.*, 2015, **41**, 12393–12400.
241 Z. Q. Deng, J. P. Smit, H. J. Niu, G. Evans, M. R. Li, Z. L. Xu, J. B. Claridge and M. J. Rosseinsky, *Chem. Mater.*, 2009, **21**, 5154–5162.
242 M. T. Tlili, N. Chihaoui, M. Bejar, E. Dhahri, M. A. Valente and E. K. Hlil, *J. Alloys Compd.*, 2011, **509**, 6447–6451.
243 J. Bassat, *Solid State Ionics*, 2004, **167**, 341–347.
244 K. Zheng and K. Świerczek, *Mater. Res. Bull.*, 2016, **84**, 259–266.
245 A. Aguadero, J. Alonso, M. Escudero and L. Daza, *Solid State Ionics*, 2008, **179**, 393–400.
246 L. M. Kolchina, N. V. Lyskov, P. P. Pestrikov, S. Y. Istomin, G. N. Mazo and E. V. Antipov, *Mater. Chem. Phys.*, 2015, **165**, 91–96.
247 W. Wang, Y. Li, Y. Liu, Y. Tian, B. Ma, J. Li, J. Pu and B. Chi, *ACS Sustainable Chem. Eng.*, 2021, **9**, 10913–10919.
248 E. Boehm, J. Bassat, P. Dordor, F. Mauvyy, J. Grenier and P. Stevens, *Solid State Ionics*, 2005, **176**, 2717–2725.
249 J. D. Jorgensen, B. Dabrowski, S. Pei, D. R. Richards and D. G. Hinks, *Phys. Rev. B: Condens. Matter Mater. Phys.*, 1989, **40**, 2187–2199.

250 D. Lee and H. Lee, *Materials*, 2017, **10**, 368.
251 L. Zhang, F. Yao, J. Meng, W. Zhang, H. Wang, X. Liu, J. Meng and H. Zhang, *J. Mater. Chem. A*, 2019, **7**, 18558–18567.
252 L. Miao, J. Hou, Z. Gong, Z. Jin and W. Liu, *Int. J. Hydrogen Energy*, 2019, **44**, 7531–7537.
253 Q. Zhou, T. Zhang, C. Zhao, L. Qu, Y. He, T. Wei and X. Tong, *Mater. Res. Bull.*, 2020, **131**, 110986.
254 S. Yoo, S. Choi, J. Shin, M. Liu and G. Kim, *RSC Adv.*, 2012, **2**, 4648.
255 G. Amow, I. Davidson and S. Skinner, *Solid State Ionics*, 2006, **177**, 1205–1210.
256 P. Ding, W. Li, H. Zhao, C. Wu, L. Zhao, B. Dong and S. Wang, *JPhys Mater.*, 2021, **4**, 022002.
257 E. Perry Murray, *Solid State Ionics*, 2002, **148**, 27–34.
258 M. M. Natile, G. Eger, P. Batocchi, F. Mauvy and A. Glisenti, *Int. J. Hydrogen Energy*, 2017, **42**, 1724–1735.
259 M. Hrovat, *Solid State Ionics*, 1996, **83**, 99–105.
260 E. Olsson, J. Cottom, X. Aparicio-Anglès and N. H. de Leeuw, *Phys. Chem. Chem. Phys.*, 2019, **21**, 9407–9418.
261 M. Valldor, *Solid State Sci.*, 2004, **6**, 251–266.
262 M. Karppinen, H. Yamauchi, S. Otani, T. Fujita, T. Motohashi, Y.-H. Huang, M. Valkeapää and H. Fjellvåg, *Chem. Mater.*, 2006, **18**, 490–494.
263 E. Tsipis, V. Kharton and J. Frade, *Solid State Ionics*, 2006, **177**, 1823–1826.
264 A. Maignan, V. Caignaert, D. Pelloquin, S. Hébert, V. Pralong, J. Hejtmanek and D. Khomskii, *Phys. Rev. B: Condens. Matter Mater. Phys.*, 2006, **74**, 165110.
265 S. Kadota, M. Karppinen, T. Motohashi and H. Yamauchi, *Chem. Mater.*, 2008, **20**, 6378–6381.
266 H. Hao, J. Cui, C. Chen, L. Pan, J. Hu and X. Hu, *Solid State Ionics*, 2006, **177**, 631–637.
267 Y. Jia, H. Jiang, M. Valkeapää, H. Yamauchi, M. Karppinen and E. I. Kauppinen, *J. Am. Chem. Soc.*, 2009, **131**, 4880–4883.
268 W. H. Kan, K.-Y. Lai, A. Huq and A. Manthiram, *J. Power Sources*, 2016, **307**, 454–461.
269 J.-H. Kim and A. Manthiram, *Chem. Mater.*, 2010, **22**, 822–831.
270 Y. N. Kim, J.-H. Kim and A. Manthiram, *Int. J. Hydrogen Energy*, 2011, **36**, 15295–15303.
271 Y. N. Kim, J. H. Kim, A. Huq, M. P. Paranthaman and A. Manthiram, *J. Power Sources*, 2012, **214**, 7–14.
272 K.-Y. Lai and A. Manthiram, *Chem. Mater.*, 2016, **28**, 9077–9087.
273 K.-Y. Lai and A. Manthiram, *J. Mater. Chem. A*, 2018, **6**, 16412–16420.
274 K.-Y. Lai and A. Manthiram, *J. Mater. Chem. A*, 2019, **7**, 8540–8549.
275 M. Karppinen, H. Yamauchi, S. Otani, T. Fujita, T. Motohashi, Y.-H. Huang, M. Valkeapää and H. Fjellvåg, *Chem. Mater.*, 2006, **18**, 490–494.
276 Z. Zhang, K. Singh, Y. Tsur, J. Zhou, J. J. Dynes and V. Thangadurai, *J. Solid State Chem.*, 2020, **290**, 121530.
277 J.-H. Kim, Y. N. Kim, S. M. Cho, H. Wang and A. Manthiram, *Electrochim. Acta*, 2010, **55**, 5312–5317.
278 S. Geller and M. A. Gilleo, *J. Phys. Chem. Solids*, 1957, **3**, 30–36.
279 H. Zhao, J. Zhou, Y. Bai, Z. Gui and L. Li, *J. Magn. Magn. Mater.*, 2004, **280**, 208–213.
280 Y. J. Wu, C. Yu, X. M. Chen and J. Li, *J. Am. Ceram. Soc.*, 2012, **95**, 1671–1675.
281 V. V. Kharton, A. L. Shaula, E. N. Naumovich, N. P. Vyshatko, I. P. Marozau, A. P. Viskup and F. M. B. Marques, *J. Electrochem. Soc.*, 2003, **150**, J33.
282 W. Zhong, Y. Ling, Y. Rao, R. Peng and Y. Lu, *J. Power Sources*, 2012, **213**, 140–144.
283 M. Juhl, S. Primdahl, C. Manon and M. Mogensen, *J. Power Sources*, 1996, **61**, 173–181.
284 Y. Leng, S. Chan, S. Jiang and K. Khor, *Solid State Ionics*, 2004, **170**, 9–15.
285 B. Philippeau, F. Mauvy, C. Nicollet, S. Fourcade and J. C. Grenier, *J. Solid State Electrochem.*, 2015, **19**, 871–882.
286 X. Chen, J. Wang, Q. Liang, X. Sun, X. Zhu, D. Zhou and J. Meng, *Solid State Sci.*, 2020, **100**, 106108.
287 S. N. Marshenya, B. V. Politov, D. A. Osinkin, A. Y. Suntsov, I. A. Leonidov and V. L. Kozhevnikov, *J. Alloys Compd.*, 2019, **779**, 712–719.
288 M. Jafari, H. Salamati, M. Zhiani and E. Shahsavari, *Int. J. Hydrogen Energy*, 2019, **44**, 1953–1966.
289 E. Zhao, C. Ma, W. Yang, Y. Xiong, J. Li and C. Sun, *Int. J. Hydrogen Energy*, 2013, **38**, 6821–6829.
290 Y. Liu, F. Wang, B. Chi, J. Pu, L. Jian and S. P. Jiang, *J. Alloys Compd.*, 2013, **578**, 37–43.
291 X. Xi, X. Chen, G. Hou, N. Xu, Q. Zhang and Z. Tao, *Ceram. Int.*, 2014, **40**, 13753–13756.
292 X. Ding, H. Liu, Z. Gao, G. Hua, L. Wang, L. Ding and G. Yuan, *Int. J. Hydrogen Energy*, 2017, **42**, 24968–24977.
293 Y. Bu, S. Joo, Y. Zhang, Y. Wang, D. Meng, X. Ge and G. Kim, *J. Power Sources*, 2020, **451**, 227812.
294 J. Hou, J. Qian, L. Bi, Z. Gong, R. Peng and W. Liu, *J. Mater. Chem. A*, 2015, **3**, 2207–2215.
295 D. Chen, Q. Zhang, L. Lu, V. Periasamy, M. O. Tade and Z. Shao, *J. Power Sources*, 2016, **303**, 305–316.
296 C. Duan, J. Tong, M. Shang, S. Nikodemski, M. Sanders, S. Ricote, A. Almansoori and R. OHayre, *Science*, 2015, **349**, 1321–1326.
297 H. Dai, E. H. Da'as, S. P. Shafi, H. Wang and L. Bi, *J. Eur. Ceram. Soc.*, 2018, **38**, 2903–2908.
298 J. Kim, *Solid State Ionics*, 2001, **143**, 379–389.
299 X. Yu, C. Sui, R. Ren, J. Qiao, W. Sun, Z. Wang and K. Sun, *ACS Appl. Energy Mater.*, 2020, **3**, 447–455.
300 J. Wang, F. Meng, T. Xia, Z. Shi, J. Lian, C. Xu, H. Zhao, J.-M. Bassat and J.-C. Grenier, *Int. J. Hydrogen Energy*, 2014, **39**, 18392–18404.
301 L.-P. Sun, Q. Li, H. Zhao, J.-H. Hao, L.-H. Huo, G. Pang, Z. Shi and S. Feng, *Int. J. Hydrogen Energy*, 2012, **37**, 11955–11962.
302 H. Wang, M. Zhou, P. Choudhury and H. Luo, *Appl. Mater. Today*, 2019, **16**, 56–71.
303 G. Yang, W. Jung, S.-J. Ahn and D. Lee, *Appl. Sci.*, 2019, **9**, 1030.
304 S. B. Adler, *Chem. Rev.*, 2004, **104**, 4791–4844.

305 S. K. Burnwal, S. Bharadwaj and P. Kistaiah, *J. Mol. Eng. Mater.*, 2016, **4**, 1630001.
306 Y.-L. Huang, A. M. Hussain, I. A. Robinson and E. D. Wachsman, *ACS Appl. Mater. Interfaces*, 2018, **10**, 28635–28643.
307 S. Mulmi and V. Thangadurai, *Chem. Commun.*, 2019, **55**, 3713–3716.
308 B. Boukamp, *Solid State Ionics*, 2004, **169**, 65–73.
309 J. R. Dygas, G. Fafilek, H. Durakpasa and M. W. Breiter, *J. Appl. Electrochem.*, 1993, **23**, 553–558.
310 J. Macdonald and L. Potterjr, *Solid State Ionics*, 1987, **24**, 61–79.
311 B. A. Boukamp and A. Rolle, *Solid State Ionics*, 2018, **314**, 103–111.
312 H. Schichlein, A. C. Müller, M. Voigts, A. Krügel and E. Ivers-Tiffée, *J. Appl. Electrochem.*, 2002, **32**, 875–882.
313 A. Leonide, V. Sonn, A. Weber and E. Ivers-Tiffée, *J. Electrochem. Soc.*, 2008, **155**, B36.
314 Z. Drach, S. Hershkovitz, D. Ferrero, P. Leone, A. Lanzini, M. Santarelli and Y. Tsur, *Solid State Ionics*, 2016, **288**, 307–310.
315 A. Oz, K. Singh, D. Gelman, V. Thangadurai and Y. Tsur, *J. Phys. Chem. C*, 2018, **122**, 15097–15107.
316 B. A. Boukamp, *Electrochim. Acta*, 2015, **154**, 35–46.
317 B. A. Boukamp and A. Rolle, *Solid State Ionics*, 2017, **302**, 12–18.
318 V. Sonn, A. Leonide and E. Ivers-Tiffée, *J. Electrochem. Soc.*, 2008, **155**, B675.
319 H. Sumi, T. Yamaguchi, K. Hamamoto, T. Suzuki, Y. Fujishiro, T. Matsui and K. Eguchi, *Electrochim. Acta*, 2012, **67**, 159–165.
320 T. Ramos, M. Søgaard and M. B. Mogensen, *J. Electrochem. Soc.*, 2014, **161**, F434–F444.
321 M. Saccoccio, T. H. Wan, C. Chen and F. Ciucci, *Electrochim. Acta*, 2014, **147**, 470–482.
322 T. Hörlin, *Solid State Ionics*, 1998, **107**, 241–253.
323 S. Hershkovitz, S. Tomer, S. Baltianski and Y. Tsur, *ECS Trans.*, 2019, **33**, 67–73.
324 Q. Yang, D. Tian, R. Liu, H. Wu, Y. Chen, Y. Ding, X. Lu and B. Lin, *Int. J. Hydrogen Energy*, 2021, **46**, 5630–5641.
325 K. Wei, N. Li, Y. Wu, W. Song, X. Wang, L. Guo, M. Khan, S. Wang, F. Zhou and Y. Ling, *Ceram. Int.*, 2019, **45**, 18583–18591.
326 N. Shi, F. Su, D. Huan, Y. Xie, J. Lin, W. Tan, R. Peng, C. Xia, C. Chen and Y. Lu, *J. Mater. Chem. A*, 2017, **5**, 19664–19671.
327 S. B. Adler, *Solid State Ionics*, 1998, **111**, 125–134.
328 L. Almar, J. Szász, A. Weber and E. Ivers-Tiffée, *J. Electrochem. Soc.*, 2017, **164**, F289–F297.
329 A. Mroziński, S. Molin, J. Karczewski, T. Miruszewski and P. Jasiński, *Int. J. Hydrogen Energy*, 2019, **44**, 1827–1838.